UNIVERSITÀ POLITECNICA DELLE MARCHE

Dipartimento di Scienze e Ingegneria della Materia, dell'Ambiente ed Urbanistica

Ph.D. Course in Information Engineering

Curriculum in Biomedical, Electronics and
Telecommunications Engineering

XXXII CYCLE

NANOSCALE STRUCTURE OF
ADVANCED SOFT MATERIALS FOR
INNOVATIVE APPLICATIONS

Supervisor

Prof. Oriano Francescangeli

Ph.D. student

Dr. Fabrizio C. Adamo

Co-Supervisor

Dr. Francesco Vita

Abstract

My Ph.D. research work was focused on the investigation of new soft materials, in particular new liquid crystals, polymers and biosystems, of potential interest for innovative applications in the fields of nano- and bio-technologies including novel electronic and photonic devices, high mechanical-performance materials, biomaterials for nanomedicine and biosensing. The main purpose of my research work was the study of the relationships between the peculiar macroscopic properties of these materials and their structure at the nanoscale. To this end, a key role was played by the X-ray diffraction and scattering techniques used as the primary tool of experimental investigation. The X-ray measurements were carried out at the synchrotron light sources of the European Synchrotron Radiation Facility, Grenoble (France), ELETTRA, Trieste (Italy), and ALBA, Barcelona (Spain), in the context of officially approved experiments. A series of complementary techniques were also employed to better characterize these materials, in collaboration with other international research groups.

The research work can be identified with four main topics: *i*) the influence of the molecular structure on the nematic phase of bent-core liquid crystals. The recently discovered cybotactic nanostructure of their nematic phase makes them the ideal candidates for the two most sought after and elusive properties of liquid crystals, namely the *nematic biaxiality* and the *nematic ferroelectricity*, widely recognized as the *Holy Grail* of the liquid crystal science. The findings suggest useful clues to guide the research effort towards the synthesis of novel bent-core mesogens exhibiting such features; *ii*) the study of the nanostructure and molecular ordering of ultra-thin films of bent-core mesogens deposited on solid substrate to gain insight into the mechanisms of anchoring and self-assembling of liquid crystal molecules at the interface and investigate the molecular space arrangement (in-plane and out-of-plane order). We obtained a highly ordered film with the anisotropic in-plane structure of the liquid crystal molecules, which has never been reported in the literature for these systems; *iii*) structural study of a reactive thermotropic liquid crystal used in the production of a new class of high-temperature/high-performance thermosets - crosslinked 3D networks designed to preserve the local nematic morphology in the solid state. High-temperature X-ray diffraction studies made it possible for the first time to monitor the transformation of the ethynyl end-group and to follow the evolution of the nematic phase during the chain extension/cross-linking

reactions; *iv*) the structural and physico-chemical characterization of novel lyotropic liquid crystalline nanosystems for their potential applications in the development of efficient and biocompatible vectors for drug delivery in nanomedicine. The study was focused on the incorporation of a cationic surfactant in the phytantriol cubic phase, unloaded and loaded with the anticancer drug 5-fluorouracil. The study evidences the efficiency of the phytantriol/ionic surfactant system as anticancer drug delivery vectors.

Contents

List of Figures

List of Tables

Abbreviations

Sm   Smectic

SmA   Smectic A

SmC   Smectic C

5-FU   neutral 5-fluororacil

5-FUs   anionic 5-fluororacil

AFM   Atomic force microscopy

ATR-FTIR   Attenuated total reflection Fourier transform infrared

BAM   Brewster angle microscope

BCM   Bent-core mesogen

CPP   critical packing parameter

CSA   Chemical shift anisotropy

DDABr   didodecyldimethylammonium bromide

DLS   Dynamic light scattering

DMOAP   Dimethyloctadecyl[3-(trimethoxysilyl)propyl]ammonium chloride

DOMA   dioctadecyldimethylammonium bromide

DOPG   1,2-dioleoyl-sn-glycero-3-phosphoglycerol

DOPS   1,2-dioleoyl-sn-glycero-3-phospho-L-serine

DRS   Dielectric relaxation spectroscopy

DSC   Differential Scanning Calorimetry

DSC   Differential scanning calorimetry

EE   Entrapment efficiency

ESRF   European Synchrotron Radiation Facitlity

FWHM   Full width half maximum

GISAXS Grazing-incidence small-angle scattering

GIWAXS Grazing-incidence wide-angle X-ray scattering

GMO   Glyceryl monooleate

H   Hexagonal

HN   Havriliak-Negami

HT/HP High-temperature/high-performance

I   Isotropic

K   Crystal

L_α Lamellar

LB   Langmuir-Blodgett

LC   Liquid crystal

LS   Langmuir-Schaefer

MLO   Glyceryl monolinoleate

N_b Biaxial nematic

N_u Uniaxial nematic

NMR   Nuclear magnetic resonance

NMR   Nuclear magnetic resonance

N   Nematic

ODBP   2,5-bis(*p*-hydroxyphenyl)-1,3,4-oxadiazole

ODF   Orientational distribution function

PDI   Polidispersity index

PE   Phenylethynyl

PHYT   Phytantriol

PSCM   Partnership of Soft Condensed Matter

Q   Cubic

SAXS   Small-angle X-ray scattering

UNC   University of North Carolina

UNICAL Università della Calabria

XRD   X-ray diffraction

XRR   X-ray reflectometry

Zp   Zeta potential value

Introduction

Soft materials are materials than can be easily deformed by thermal stresses or fluctuations at about room temperature and are strongly affected by application of external mechanical, electric or magnetic fields. Soft materials include liquids, polymers, gels, foams, colloids as well as most biological materials. Beside their fundamental interest spanning several areas from physics and chemistry to biology and medicine, they are of great interest for a variety of technological applications in many different fields.

Following a research line undertaken a few years ago by the Soft Matter Group of the SIMAU Department at the Polytechnic University of Marche under the supervision of Prof. O. Francescangeli, my Ph.D. research work was focused on the investigation of new soft materials, in particular new liquid crystals (LCs), polymers and biosystems, of potential interest for innovative applications in the fields of nano- and bio-technologies including novel electronic and photonic devices, high mechanical-performance materials, biomaterials for nanomedicine and biosensing. The main purpose of my research work was the study of the relationships between the peculiar macroscopic properties of these materials and their structure at the nanoscale. To this end, a key role was played by the X-ray diffraction (XRD) and scattering techniques used as the primary tool of experimental investigation. The X-ray measurements were carried out at the synchrotron light sources of the European Synchrotron Radiation Facility (ESRF), Grenoble (France), Elettra, Trieste (Italy), and ALBA, Barcelona (Spain), in the context of officially approved experiments. A series of complementary techniques were also employed to better characterize these materials, in collaboration with other international research groups, which include differential scanning calorimetry (DSC), optical polarizing microscopy, atomic force microscopy (AFM), nuclear magnetic resonance (NMR), dielectric relaxation spectroscopy (DRS), attenuated total reflection Fourier transform infrared (ATR-FTIR) spectroscopy, UV–Vis spectroscopy and dynamic light scattering (DLS). The structure of this doctoral thesis is here summarized.

After a short introduction in Chapter 1 on the general properties of LCs, Chapter 2 describes the research work carried out on a novel class of LCs based on bent-core mesogens (BCMs). The bent shape of these molecules and their transverse molecular dipole result in a marked

predisposition to stratification. This tendency strongly favours the formation of a variety of polar (and biaxial) smectic (*Sm*) phases and it is retained, in the form of nanosized clusters, even in the nematic (N) phase. The technological potential of these materials for new ultra-fast displays and photonic devices for optical data storage and processing, relies on the recently discovered *cybotactic* nanostructure of their N phase. This makes them ideal candidates for the two most sought after and elusive properties of LCs, namely the *nematic biaxiality* and the *nematic ferroelectricity*, widely recognized as the *Holy Grail* of the LC science. The materials investigated were synthesised by the groups of Prof. E. T. Samulski, University of North Carolina (UNC), Chapel Hill, USA, and Prof. E. Scharrer, University of Puget Sound, Tacoma, USA. The DRS measurements were carried out in collaboration with the group of Prof. N. Scaramuzza, Università della Calabria (UNICAL), Rende, Italy. Some of the results of this research have already been published in the two papers:

- F. Vita, F. C. Adamo, O. Francescangeli, "Polar order in bent-core nematics: An overview", *J.Mol.Liq.*, 267, 564-573 (2018);

- R. Harkins, T. Tauscher, J. Nguyen, S. Lewis, F. C. Adamo, M. Pisani, D. Hermida-Merino, E. T. Samulski, F. Vita, O. Francescangeli, E. Scharrer, "Biaxial ordering in the supercooled nematic phase of bent-core mesogens: effects of molecular symmetry and outer wing lateral groups", *Liq.Cryst.*, DOI: 10.1080/02678292.2019.1633431 (2019);

while others are the subject of papers in preparation for a forthcoming publications. Chapter 3 concerns the study of the nanostructure and molecular ordering of ultra-thin films of LCs deposited on solid substrates. The scope of the investigation was to gain insight into the mechanisms of anchoring and self-assembling of LC molecules at the LC-solid interface and investigate the molecular space arrangement (in-plane and out-of-plane) in thin films of LCs spanning from a few molecular layers down to a monolayer. Besides the fundamental physico-chemical aspects, this topic is of great interest also for potential applications in the design of organic electronic devices such as organic thin film transistors, organic photovoltaic cells and biosensors. Despite the great importance, the field is still essentially unexplored in particular from the experimental point of view, and only very recent experiments and simulations have started to study the LC anchoring at the nanoscale. In this frame, my activity was devoted to the investigation of these aspects using grazing-incidence wide-angle X-ray scattering (GIWAXS) and X-ray reflectometry (XRR) as the primary experimental tools to probe the nanoscale structure of a representative class of LC molecules, namely the BCMs, deposited as mono- or multi-layers over a solid substrate. My activity also included the preparation and deposition of the LC films with different techniques, carried out at

the LYCRIL laboratories of the UNICAL and at the Partnership of Soft Condensed Matter (PSCM) laboratories of the ESRF, as well as their morphological characterization by means of AFM. Because of the difficulty of addressing such a limit case of very low scattering volumes, these experiments were quite challenging and represent a new and original contribution. The preliminary results of these very recent investigations are reported in the following paper submitted for publication:

- F. C. Adamo, F. Vita, O. Francescangeli *et al*, "Nanoscale structure of Langmuir-Blodgett film of bent-core molecules", *Langmuir* SUBMITTED.

Chapter 4 concerns the structural study of a reactive thermotropic LC used in the production of a new class of high-temperature/high-performance (HT/HP) thermosets - crosslinked 3D networks designed to preserve the local N morphology in the solid state. In particular, the study was focused on the evolution of the LC order investigated using two phenylethynyl(PE)-terminated biphenol (PE-biphenol-PE) and naphthalenediol (PE-naphthalenediol-PE) model compounds. Understanding this evolution is key for a deeper comprehension of the role of the N order of the macromonomers in determining the structural properties of the corresponding LC thermoset. High-temperature X-ray diffraction studies, carried out at the ESRF, and NMR experiments, performed in collaboration with the group of Prof. Samulski at UNC, made it possible for the first time to monitor the transformation of PE end-groups (specifically, the ethynyl group) and to follow the evolution of the N phase during the chain extension/cross-linking reactions. The results of this study have published in the following paper:

- F. Vita, F. C. Adamo, M. Pisani, L. M. Heist, M. Li, M. Hegde, T. J. Dingemans, E. T. Samulski, O. Francescangeli, "Liquid crystal thermosets. A new class of high-performance materials", *Liq.Cryst.*, DOI: 10.1080/02678292.2019.1641233 (2019).

Chapter 5 reports the structural and physico-chemical characterization of novel lyotropic LC nanosystems for their potential applications in the development of efficient and biocompatible vectors for drug delivery in nanomedicine. Because of their highly ordered internal structures, inverse bicontinuous cubic and inverse hexagonal mesophases are attracting growing interest for their ability to incorporate different therapeutic agents (from small drug molecules to biomacromolecules) and their capacity to control or sustain their release. In this context, addition of a cationic surfactant is known to affect the mesophase structure of the lipid matrix and therefore it can be used as a tool to control its entrapment efficiency. The systems here investigated are based on the phytantriol (PHYT) amphiphilic lipid that exhibits higher resistance to hydrolysis compared to the most commonly used amphiphilic

lipids in lyotropic LC reserach. Specifically, my study was focused on the effects of the incorporation of the didodecyldimethylammonium bromide (DDABr) cationic surfactant in the phytantriol cubic phase, unloaded and loaded with the anticancer drug 5-fluorouracil. The formulations, prepared as bulk and dispersed phases, were characterized by synchrotron small-angle X-ray scattering (SAXS), ATR-FTIR and UV–Vis spectroscopy and DLS. The results of this research have been published in the paper:

- P. Astolfi, E. Giorgini, F. C. Adamo F. Vita, S. Logrippo, O. Francescangeli, M. Pisani, "Effects of a cationic surfactant incorporation in phytantriol bulk cubic phases and dispersions loaded with the anticancer drug 5-fluorouracil", *J.Mol.Liq.*, 286, 110954 (2019).

Chapter 1

Liquid crystals

Over the last decades, soft condensed matter has attracted tremendous interest for both fundamental and technological reasons. Soft matter is quite common around us (*e.g.* paint, ink, foam, emulsion, gel etc.) and we ourselves could be considered soft machines [1–3]. Within the wide class of soft materials, LCs play a unique role.

LCs are a state of matter whose properties are between those of conventional liquids and those of solid crystals [4–7]. In a crystal, the basic components (atoms, molecules or groups of molecules) are regularly stacked in a three-dimensional (3D) periodic lattice and accordingly they exhibit 3D long-range positional as well as orientational order. As a result, the corresponding X-ray diffraction pattern shows sharp Bragg reflections characteristic of the lattice. In a liquid, the centres of gravity of the molecules are not ordered in this sense and there exists an isotropic length scale (the *correlation* length, ξ) over which particle-particle correlations are lost (particle: atom, molecule or molecular group). The corresponding X-ray diffraction pattern exhibits diffuse peaks of width $\propto \xi^{-1}$. LCs are systems in which a liquid-like order exists at least in direction of space (1D) and in which some degree of anisotropy is present. Differently from most common materials, LCs do not show a single transition from solid to liquid, but rather a cascade of transitions involving new phases whose mechanical and symmetry properties are intermediate between those of a liquid and those of a crystal. These phase are commonly referred to as "mesomorphic phases" (*mesomorphic*: of intermediate form). The mesophases can be obtained in two distinct ways:

1. Imposing no positional order or imposing positional order in one (1D) or two (2D) rather than in three dimensions. The first case corresponds to the N mesophase, *i.e.* an *anisotropic* liquid having particle-particle correlation function featured by different correlation lengths, $\xi_\perp$ and $\xi_\parallel$, parallel and perpendicular to a macroscopically defined direction, respectively. The second case describes 1D order in three dimensions: the

system can be viewed as a set of 2D liquid layers stacked on each other with a well defined spacing: the corresponding phases are called *Sm* mesophases. Finally, the third case corresponds to 2D ordered systems in three dimensions. They can be described as a 2D array of liquid tubes and are called *columnar* mesophases.

2. Introducing degrees of freedom that are distinct from the localization of the particle centres of mass. For non-spherical molecules, these are given by the molecular orientations. Orientational transitions may take place in crystals, LCs and isotropic liquids. In the first two cases the freezing of orientational degrees of freedom does not generate very novel phases. On the other hand, freezing out orientational degrees of freedom in an isotropic liquid does yield anisotropy. The phase obeys the definition of a nematic.

N, *Sm* and columnar phases are the known forms of LCs. The type of LCs that may be observed depends heavily on the structure of the constituent molecules (the *building blocks*). Nematics and smectics are often made of *elongated* objects, whereas some other nematics and most columnar phases are made of disk-like molecules. Depending on the nature of the building blocks and on the external parameters (temperature, concentration, etc..), we can observe a variety of transitions amongst LCs.
In general it is possible to define two families of LC:

- **Thermotropics**: the parameter that induces the mesophase transition is the temperature.

- **Lyotropics**: the parameter that induces the mesophase transitions is the concentration of molecules in a solvent.

1.1   Thermotropic liquid crystals

Thermotropic LC molecules have the peculiarity to be anisotropic and this influences the physical properties, which are subsequently anisotropic. The most conventional LCs are the so-called calamitic mesogens. They are typically constituted by a central aromatic rigid core connected with flexible aliphatic tails that are relatively free to move. From the physical point of view, they can be schematically represented like a rod (or in some cases as a rod capped with a hemisphere at each extremity) or elongated ellipsoid, as the model structures in Fig. 1.1. However, LC thermotropic phases are observed also in other exotic molecular shapes like discotic molecules, banana-shaped, hockey-stick etc.
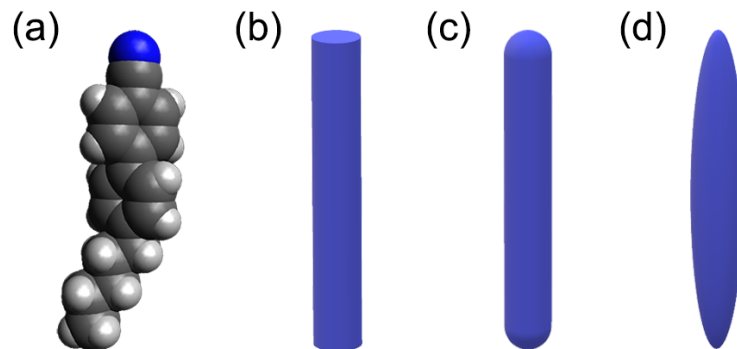
Figure 1.1 Model structures of a calamitic mesogen: (a) 5CB molecular structure, (b) rod, (c) capped rod and (d) ellipsoid. In (a) the carbon atoms are in black, the hydrogen atoms in white and the nitrogen atom in blue.

In thermotropic LCs, the transition from isotropic (I) phase to LC phase is driven by changes in temperature. A typical phase diagram is shown in Fig. 1.2. It makes apparent the changes in the molecular order passing from the crystal (K) phase, characterized by both orientational and positional order, to conversely disordered I phase; between them, the N phase exhibit only orientational order. In a more common situation, other mesophase sequences can be observed in the phase diagram between the K and the I phases, which involve the appearance of *Sm* mesophases below the N. Here we focus on their main physical properties of nematics and smectics and their interaction with external fields and surfaces.
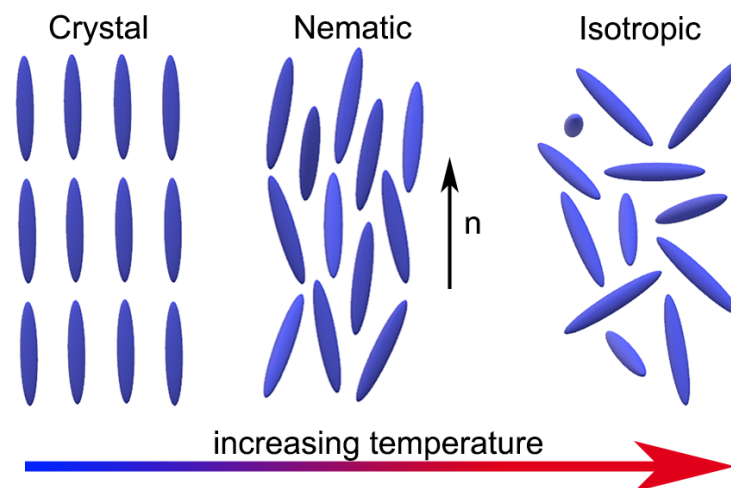
Figure 1.2 Typical phase diagram of a N LC. In the N phase the black arrow points out the director **n**.

1.1.1   Nematics

The N mesophase is featured by long range *orientational order* of the molecules and the absence of long range *positional order* of the molecular centres of mass. A model structure of the N phase is illustrated in Fig. 1.2. The molecules tend to align parallel to each other in order to minimize the excluded volume and maximize the attractive Van der Waals interaction between them [8, 9]. The preferential orientation of the molecular long axis is pointed out by a unit vector **n** called the *director*. All physical properties, even from macroscopical point of view, can be described using this vector and its space dependence, *i.e.* the director field **n(r)**. The direction of **n** is arbitrary in space, it depends on the molecular and external field interaction. The two states **n** and -**n** are indistinguishable and accordingly a conventional N phase is macroscopically apolar even when constituted by polar molecules. Moreover, the translational motion of the molecules is possible in any direction, so the density is isotropically constant and the N phase is the most fluid of the LC phases.
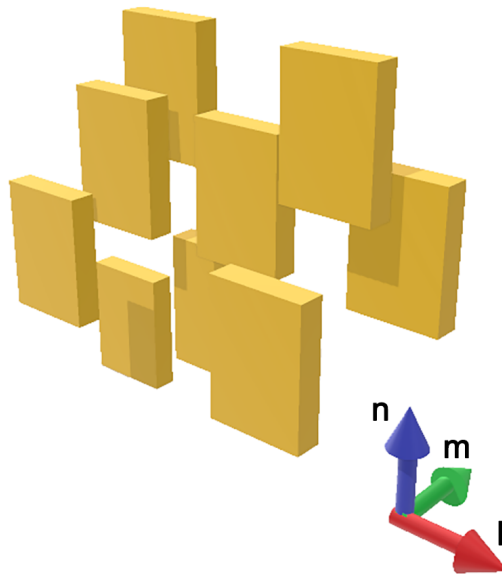
Figure 1.3 Model structures of biaxial nematic phase with the three directors **n**, **m** and **l**.

Hitherto, the discussion was focused on the uniaxial N phase (N_u) that possesses cylindrical symmetry around **n**. In the N_u phase all the directions perpendicular to **n** are identical and therefore the phase is optically uniaxial. When the molecular cylindrical symmetry is broken, there is a need to introduce new directors perpendicular to **n** to describe the preferential molecular orientations of the anisotropic molecules. Fig. 1.3 shows an example

of a structure with reduced symmetry where the anisometric molecules can be schematized as parallelepiped platelets and the molecular arrangement is featured by a triad of orthogonal directors. From the optical point of view this structure is biaxial and the corresponding mesophase is called biaxial nematic (N_b) [10, 11].

1.1.2 Smectics

Sm LCs have stratified structures but a variety of molecular arrangements are possible within each stratification. Respect to the N phase, there is periodicity along a direction because the molecules tend to organize in layers. The *Sm* phase can form on cooling the N phase or directly from the I phase. There exists a variety of *Sm* phases with different degree of positional and orientational order and each type is identified with a capital letter following the chronological discovery order (*e.g. SmA*, *SmB*, *SmC* and so on ...). Here we focus our interest on the *SmA* and *SmC* phases which consist of stacks of liquid-like layers. In fact, the two phases can be considered like a one-dimensional solid and a two-dimensional liquid with the spatial positions of the molecules on neighbor layers.

In the *SmA* phase the molecules are upright in each layer with their centres of mass irregularly spaced in a liquid-like fashion. The interlayer attractions are weak as compared with the lateral forces between molecules and as a consequence the layers are able to slide over one another relatively easily. Hence this mesophase has fluid properties, although it is very much more viscous than the N phase. In Fig. 1.4 is shown the lamellar structure of the *SmA* phase featured by the interlayer distance d. In the *SmA*, there is higher orientational order compared to the N phase; nevertheless, as in the N phase, there are no differences between of **n** and -**n** and there is translational invariance but only in the two directions of a layer plane, where the density is constant. The mass density along the direction perpendicular to the *Sm* layers is a periodic function. To maintain valid the relationship between **n** and -**n**, it has to be an even function like:

$$\rho(z) = \rho_0 + \sum_{n=1}^{\infty} \rho_n \cos nqz , \qquad (1.1)$$

where z is the direction of layering, ρ_0 is the mass density in the centre of a single layer and $q = \frac{2\pi}{d}$ is the wavevector of the periodic structure. Since longitudinal thermal disorder add Fourier terms which damps the higher terms, we have that $\rho_n < \rho_0$ for each n and the eqn 1.1 can be approximated to the first harmonic:

$$\rho(z) = \rho_0 + \rho_1 \cos qz , \qquad (1.2)$$

where ρ_1 is generally used as the translational order parameter.
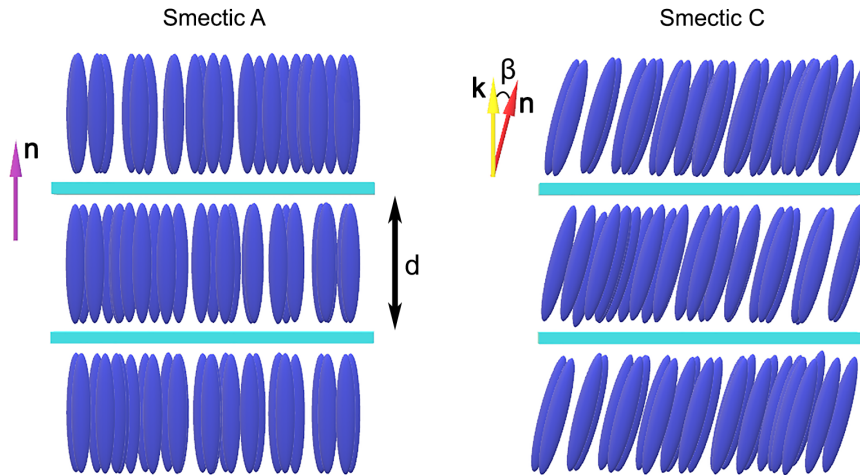
Figure 1.4 Lamellar structure of the *SmA* phase with the director **n** in violet. For the *SmC* phase, the director **n** in red is tilted respect to the layers normal **k** by an angle β. *d* points out the interlayer distance.

The *SmC* phase is a tilted form of the *SmA* phase, *i.e.* in the *SmC* phase the longitudinal molecular axes are tilted from the *Sm* layer normal by an angle β. Fig. 1.4 shows the molecular structure of the *SmC* phase. The tilt of the molecules in different layers is the same, but not the spatial position (as in *SmA* phase). The density has the same features of the *SmA* phase, constant in each layer while normal to the layer it is described by eqn 1.2. The director **n** has the same definition and properties of the previous phases.

1.1.3   Liquid crystal polymers

LC polymers represent an important subclass of LCs. A polymer will have a propensity to form a LC phase if its backbone is relatively rigid and the molecules behave as a rigid rods. As it is shown in Fig.1.5, it is possible to distinguish between two classes:

- **Main-chain polymers**: a rigid backbone linked with a flexible part to another one (Fig 1.5(a)).

- **Side-chain polymers**: mesogenic groups are linked with flexible spacers (Fig 1.5(b)) to a backbone.
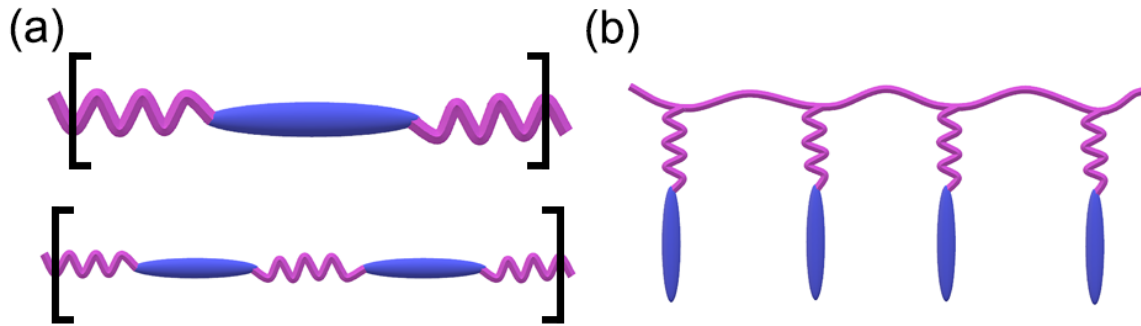
Figure 1.5 Model structures of (a) main-chain LCs polymer and (b) side-chain LCs polymer.

Flexible chains (spacers) are necessary to provide a certain freedom to mesogenic moieties to form an ordered state. LC polymers can form the same thermotropic phases as low-molecular mass compounds (N, *Sm* phases as well). Despite the same symmetry, physical properties of LC polymers are very specific. They are very viscous due to the entangling of long polymer chains hindering the translational motion (flow). On cooling the LC polymers acquire a glassy state very useful for many applications. For example, it is possible to create some macroscopic structures in the N phase very sensitive to external fields and then froze it into the glassy state which is not K but mechanically solid. Some LC polymers can be elastic as rubber (elastomers). They have very good prospectsas piezoelectric materials as well as materials having mechanically tunable optical properties.

1.1.4   Order parameter

We started our discussion about thermotropic LCs introducing qualitatively the concept of orientational order, which is lost on heating a substance from the K to the I phase. Here we introduce a quantitative definition of the order parameter. Obviously, this quantity must be zero for the I phase and non-zero for LC phase. We will concentrate on the N phase where we have only orientational order. Rigid rods are the simplest type of molecules that exhibit N behaviour. The axis of one rod labelled by a unit vector **a**. The rod is assumed to have complete cylindrical symmetry about **a**. The **n**-director, *i.e.* the average direction of alignment of the molecules, is taken along z-axis. Fig. 1.6 reports a sketch of a molecule in the laboratory frame (x, y, z). The three components of a can be expressed as:

$$a_x = \sin\theta\cos\phi \,,$$
$$a_y = \sin\theta\sin\phi \,, \tag{1.3}$$
$$a_z = \cos\theta \,.$$

The state of the alignment of all molecules can be expressed using the distribution function $f(\theta,\phi)d\Omega$, which give the probability to find a molecule in a small solid angle $d\Omega = \sin\theta d\theta d\phi$ around the direction (θ,ϕ). Because of the cylindrical symmetry around $\mathbf{n}$ of the N phase, $f(\theta,\phi)$ is independent of ϕ. Moreover, $\mathbf{n}$ and $-\mathbf{n}$ are equivalent, therefore $f(\theta) = f(\pi-\theta)$. The general appearance of $f(\theta)$ is reported in Fig. 1.6.
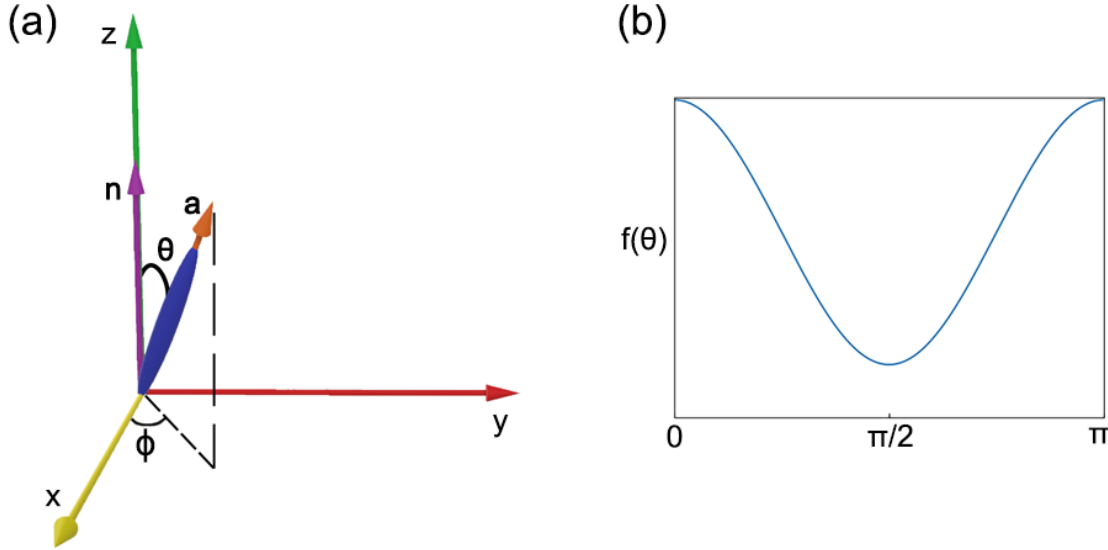
Figure 1.6 (a) Vectors and angles in the laboratory frame for a LC molecule; (b) the distribution function $f(\theta)$ in the N phase: $f(\theta)$ is large around $\theta = 0$ or π and is small for $\theta \simeq \pi/2$.

To express the orientational order through a numerical paramenter, we have to average a proper quantity using the distribution function. The quantity can be consider from the terms of a multipoles expansion [4]. For the previous assumption, averaging the first order term proportional to $\cos\theta$ the results is zero, because there is no average dipole. The first term giving a non-trivial result is the quadrupole, so we can express the orientational order parameter S in terms of second-order Legendre polynomial:

$$S = \langle P_2(\cos\theta)\rangle = \frac{1}{2}\langle(3\cos^2\theta - 1)\rangle = \int f(\theta)\frac{1}{2}(3\cos^2\theta - 1)d\Omega \,. \tag{1.4}$$

For instance, if $f(\theta)$ is strongly peaked around $\theta = 0$ and π, (parallel alignment of the molecules and very high order), $\cos\theta = \pm 1$ and $S = 1$. Conversely, if there is no alignment and $f(\theta)$ is independent of θ, we would have $\langle\cos^2\theta\rangle = 1/3$ and $S = 0$. For the *Sm* phase it is possible to introduce an order parameter for the translational order which will be zero in the *N* phase and non-zero in the *Sm* phase [12].

1.1.5 Magnetic field effects

Most organic molecules, like LCs, are diamagnetic. The diamagnetism is particularly strong when the molecule is aromatic. In a benzene ring placed in a magnetic field normal to its plane, a current is generated that tends to reduce the flux going across it; in this way the field lines are expelled and the energy interaction increases. On the other hand, if the magnetic field is in the plane of the aromatic ring, there is no induced current and the energy is minimized. Thus the organic molecules tend to choose a configuration with the benzene ring parallel to the magnetic field. In conventional LCs there are at least two aromatic rings, so the LC molecules tend to align along the magnetic field. To describe the behaviour of the complex systems, like LCs, in general is convenient to obtain an expression for the free energy that, for the thermodynamic principles, must be minimized. The magnetization **M** in an anisotropic media is expressed through a second-rank tensor for the magnetic susceptibility χ [4, 7]:

$$M_\alpha = \mu_0^{-1}\chi_{\alpha\beta}B_\beta \,, \qquad \alpha,\beta = x,y,z \,, \tag{1.5}$$

where $\chi_{\alpha\beta}$ is an element of χ, μ_0 is the vacuum permeability and **B** is the magnetic induction. Restricting to uniaxial phases and taking **n** along the z axis, χ takes diagonal form [1]:

$$\begin{bmatrix} \chi_\perp & 0 & 0 \\ 0 & \chi_\perp & 0 \\ 0 & 0 & \chi_\parallel \end{bmatrix} \tag{1.6}$$

The subscripts $\perp$ and $\parallel$ are used to indicate the components normal and parallel to **n**. The magnetic anisotropy is defined as:

$$\Delta\chi = \chi_\parallel - \chi_\perp \,. \tag{1.7}$$

Hence the susceptibility tensor has only two different non zero elements, and we find:

---

[1]In a biaxial phase we have three different values for the χ diagonal matrix, because the two directions normal to **n** are not indistinguishable.

$$\mathbf{M} = \mu_0^{-1} \chi_{\parallel} \mathbf{B}, \qquad \text{if} \quad \mathbf{B} \parallel \mathbf{n},$$
$$\mathbf{M} = \mu_0^{-1} \chi_{\perp} \mathbf{B}, \qquad \text{if} \quad \mathbf{B} \perp \mathbf{n}. \tag{1.8}$$

In the general case in which there is an arbitrary angle between $\mathbf{B}$ and $\mathbf{n}$, the magnetization will be:

$$\mathbf{M} = \mu_0^{-1} \chi_{\perp} \mathbf{B} + \mu_0^{-1} \Delta \chi (\mathbf{B} \cdot \mathbf{n}) \mathbf{n}. \tag{1.9}$$

The free energy density in a magnetic field then is given by:

$$F_{magn} = -\int \mathbf{B} \cdot d\mathbf{M} =$$
$$= -\frac{1}{2} \mu_0^{-1} \chi_{\perp} \mathbf{B}^2 - \frac{1}{2} \mu_0^{-1} \Delta \chi (\mathbf{B} \cdot \mathbf{n})^2. \tag{1.10}$$

The first equality follows from the fact that $\int \mathbf{B} \cdot d\mathbf{M} = \int \mathbf{M} \cdot d\mathbf{B}$. For diamagnetic substances, $\chi_{\parallel}$ and $\chi_{\perp}$ are small and negative, of the order of 10^{-5} SI units. The term $1/2\mu_0^{-1}\chi_{\perp}\mathbf{B}^2$ in eqn (1.10) is independent of the molecular orientation (*i.e.* independent from $\mathbf{n}$). For the minimization of the free energy density in eqn (1.10), we have to take in account only the last term and since in usual nematics $\Delta\chi > 0$, the director $\mathbf{n}$ will be collinear with $\mathbf{B}$, as stated before.

1.1.6 Electric field effects

An electric field applied to a LC has many physical effects [13]. Two of the most interesting features for technological applications are flexoelectricity [14] and ferroelectricity [15, 16]. The first is similar to the piezoelectric effect in the solids, *i.e.* applying a strain to the LC it is possible to induce a polarization, or vice versa an applied field may induce a distortion in the bulk; the second is the LC property exhibit a permanent polarization with no applied electric field. Here we restrict to the simple case of a perfect N insulator under an applied electric field $\mathbf{E}$ (dc, low frequency or optical) and we consider the interaction free energy density. The displacement $\mathbf{D}$ may be written as:

$$\mathbf{D} = \varepsilon_{\perp} \mathbf{E} + \Delta\varepsilon (\mathbf{n} \cdot \mathbf{E}) \mathbf{n}, \tag{1.11}$$

where $\varepsilon_{\parallel}$ and $\varepsilon_{\perp}$ are the static dielectric constants measured along or normal to the N axis, respectively. The dielectric anisotropy

$$\Delta\varepsilon = \varepsilon_\parallel - \varepsilon_\perp \ , \tag{1.12}$$

may be positive or negative, depending on the detailed chemical structure of the molecules. The free energy density of a LC in an electric field can be expressed as [4]:

$$
\begin{aligned}
F_{el} &= -\int \mathbf{D} \cdot d\mathbf{E} = \\
&= -\frac{1}{2}\varepsilon_\perp \mathbf{E}^2 - \frac{1}{2}\Delta\varepsilon(\mathbf{E}\cdot\mathbf{n})^2 \ .
\end{aligned}
\tag{1.13}
$$

The first term in the last equation does not depend on **n** orientation with respect to the electric field, so it does not contribute in the minimization; on the other hand, the second term is relevant in the minimization and two cases are possible: if $\Delta\varepsilon > 0$ the molecules align with the electric field (**n** ∥ **E**); if $\Delta\varepsilon < 0$ the molecules tend to orient perpendicular to the electric field (**n** ⊥ **E**).

1.1.7 Surface Anchoring

Being a fluid phase, LCs require proper confining systems. In addition, experimental investigation often need the use of cell and/or capillary. The structure of the LC molecules in the proximity of confining surfaces strongly affect the LC orientation even in the bulk [17, 18]. We will concentrate our discussion about the N phase (by reason of its low viscosity respect to the *Sm* phase) and to the interaction with solid substrates. The surface properly treated or modified can induce different director orientation. This effect is an interplay of some phenomena which can occur, *i.e.* the surface wetting [19], polar surface order and surface polarization [20], and simply elastic properties of the mesophase [18]. In the following, two general types of molecular orientations with the most common alignment methods are outlined (Fig. 1.7).

Planar alignment

Planar alignment occurs when the director **n** is parallel to the surface plane. If the long molecular axis is oriented in the plane of the substrate with the azimuthal angle being arbitrary the alignment is degenerate planar (referred to tangential alingment). On the other hand, the LC has a uniform planar alignment when the long molecular axis is not only oriented in the plane of the substrate, but also pointing along a preferred azimuthal direction. To produce planar alignment, there are two main surface treatments: by mechanical rubbing of a

polymer deposited on the surface (or, in some cases, directly rubbing the surface) [21], or by the evaporation of metals or oxides onto the surface at oblique incidence [22, 23].

Homeotropic alignment

In this case the director is perpendicular to the surface. The most popular technique for homeotropic orientation is the use of surfactants. There are several way to depositate a monolayer surfactant on a surface: spin coating of a solution, withdrawing of the substrate from the solution, plasma discharge or polymerization of the organosilicon directly onto the substrate. Also other methods induce homeotropic alignment, like etching the surface glass or treating a substrate with organometallic complexes. Even some crystalline cleavages (Al_2O_3 and $LiNbO_3$) can orient nematogens homeotropically.
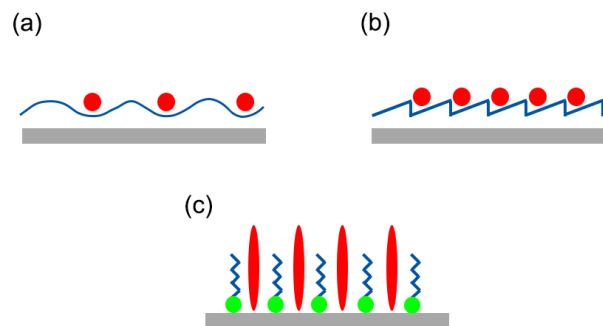
Figure 1.7 Different types of LCs alignments: (a) and (b) planar alignment with rubbed polymer and SiO_x evaporation, respectively; (c) homeotropic alignment using surfactants.

1.2 Lyotropic liquid crystals

The lyotropic LC systems are represented by molecules, such as lipids or surfactants, that show an amphiphilic nature deriving from the presence in the same molecule of two different parts, one hydrophilic and the other one hydrophobic. Usually the hydrophilic portion is depicted as the "head", with the hydrophobic portion as the "tail". In aqueous solutions amphiphilic molecules are able to self-assemble into compartments (*structure elements*) and to organize in stable structures. A variety of different phases can exist as a function of water concentration and temperature for a specific lipid (this property is called *polymorphism*) and small variations in the environment, such as changes in temperature or pH, can lead to phase transitions. One of the major driving forces for amphiphilic self-assembly is the hydrophobic effect, which acts to minimize the interface between the hydrocarbon tails of the amphiphile

and the solvent-water. The different mesophases result from an optimization of hydrophobic effect in combination with other geometric packing constrains.

In particular, the geometry of different amphiphilic molecules and the derived structures formed in the presence of a solvent can be explained by considering the critical packing parameter (CPP). The CPP provides a useful measure of aggregation topology. This parameter can be defined as CPP$= v/a_0 l_c$, where v is the volume of the hydrophobic chain(s) of the molecule, l_c is the length of the hydrophobic tail, and a_0 is the effective polar headgroup area. CPP characterizes local packing constraint and permits amphiphiles to be categorized by their "shape". From such geometric constraints and in the absence of inter-aggregate interactions, the mesophases can be classified as follows: for CPP < 1, the amphiphilic molecules have hydrophilic groups larger than the hydrophobic ones and they tend to form "normal" or Type I phases; while for CPP >1, the hydrophobic regions are greater than the hydrophilic ones, in this case the molecules form "inverse" or Type II structures; for CPP = 1, the amphiphiles occupy an apparently cylindrical space and they form lamellar phases (Fig. 1.8).
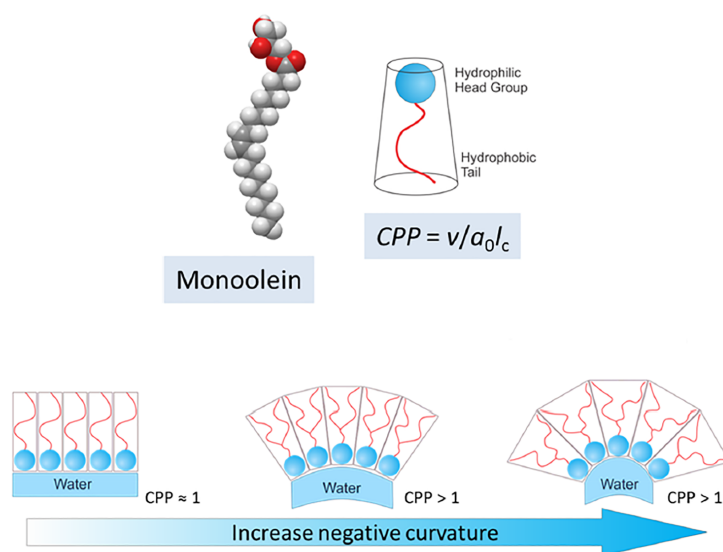
Figure 1.8 Example of an amphiphilic molecule, the monoolein, with the CPP model with some structures commonly observed self-assembled. Adapted with permission from [24]. Copyright 2019 American Chemical Society.

The major and most studied mesophases are one-dimensional lamellar (L$_\alpha$), two-dimensional hexagonal (H), and three-dimensional cubic (Q) based on their symmetries. The L$_\alpha$ mesophases are the simplest and largest studied, they have a one-dimensional structure consisting of bilayer sheets separated by a layer of aqueous solvent. Each bilayer consists of two monolayers stacked on each other in order to shield the hydrocarbon chains from any contact with water. In excess of water the lipid bilayers fold upon themselves forming a

vesicular system, called liposome.

In the H phase, the structures elements are rods, infinitely long and packed onto a two-dimensional H lattice. H phases can be either "normal" (H_I), with the cylinders filled by hydrocarbon chains and the polar groups of the amphiphiles exposed to the water, or "inverse" (H_{II}), the cylinders are filled by water and dispersed in a continuous medium consisting of hydrocarbon chains. The lyotropic phases with three-dimensional long range ordered structures characterized by Q symmetries are called *cubic phases*. According to the presence of continuous polar and hydrocarbon media, cubic phases have been separated in two different categories: *bicontinuous*, in which both the polar and hydrocarbon regions are continuous, and micellar, in which only one of the two media is continuous. The bicontinuous cubic phases have received growing interest for the last decades and several articles about cubic phases as carriers for drug delivery have been published [25, 26]. These phases consist of a single continuous curved lipid bilayer forming a complex network with three-dimensional Q symmetry, which separates two continuous but non intersecting water channels. The bicontinuous cubic phases are characterized by the crystallographic space groups *Im3m* (primitive), *Pn3m* (double diamond), *Ia3d* (gyroid). The *Im3m* phase, water channels meet at 90° in 6-ways junctions; in the *Pn3m* phase water channels meet in 4-way junctions at the tetrahedral angle (109,5°). The two networks of water channels are identical to one another in these two phases. In the *Ia3d* phase they meet in 3-way junctions at 120°. Two water regions in this phase are not similar but they are enantiomeric (Fig. 1.9).

The materials reported to form lyotropic LC phases include zwitterionic, nonionic, cationic and anionic surfactants, and amphiphilic lipids of biological origin, such as monoglycerides, phospholipids, glycolipids and sphingolipids. These lyotropic LC systems are thermodynamically stable and they can be dispersed into smaller particles that retain the complex internal nanostructure in the presence of a stabilizer (polymer). Dispersions of these bulk "parent" phases have been given the suffix "-osome". The dispersions from the L_α, H and Q phases are called as *liposomes*, *hexosomes* and *cubosomes* respectively. The key advantages of the hexosomes and cubosomes particles compared to liposomes include their ordered 3D internal structure with potential for controllable release and their increased lipid volume fraction per particle, which provides a large lipophilic area for containing poorly water-soluble lipophilic drugs. Furthermore, these nanoparticles represent promising carriers for improvement the hydrophilic or hydrophobic drug payload, protection from hydrolysis, oxidation and enzymatic degradation. The formulations of these nanoparticles offer a large surface area, low viscosity, high stability and can exist at almost any dilution level. Combined with the low cost of the raw materials and the potential for controlled release through functionalization, they represent an attractive choice.
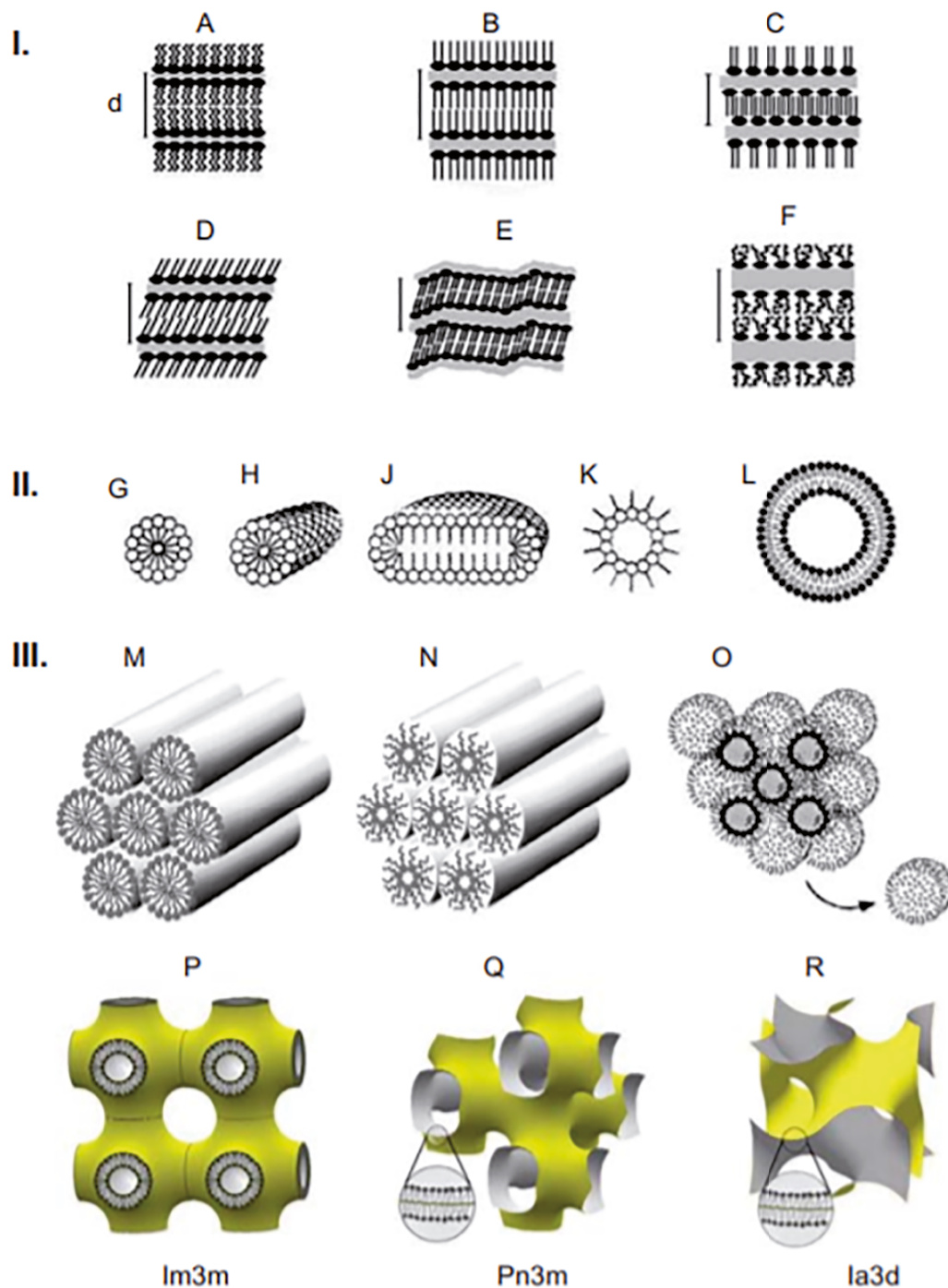
Figure 1.9 Structures of lipid phases. In **I** schematic of various lamellar phases: subgel (A), gel (B), interdigitated gel (C), gel with tilted chains (D), rippled gel (E) and LC (F). In **II** are shown micellar aggregates: spherical micelles (G), cylindrical micelles (tubules) (H), disks (J), inverted micelles (K) and liposome (L). In **III** we find the non-lamellar lyotropic LC phases of various topology: H_I (M), H_{II} (N), inverted micellar Q phase (O), bicontinuous Q phase *Im3m* (P), *Pn3m* (Q) and *Ia3d* (R). Reprinted from [27].

Chapter 2

The cybotactic nematic phase of laterally-substituted bent-core mesogens

2.1 Introduction

BCMs [28] were developed more than 20 years ago [29] and since then have taken centre stage in current LC science. This interest is due to the fact that even a small kink in the molecular shape leads to new and highly unconventional properties not observed in calamitic mesogens: extraordinary sensitivity to magnetic [30, 31] and electric fields [32], giant flex-oelectricity [33], unusual rheological properties [34, 35], ferroelectric-like switching upon application of an electric field [36–40]. Above all, BCMs have been claimed to represent the first example of biaxial nematic among low molecular weight thermotropic LCs [41, 42], although the true nature of their supposed biaxiality-macroscopic or local, spontaneous or field-induced-has been strongly questioned in the literature [10, 43–46].

It is now clear that all these unique features derive from the BCMs' marked predisposition to stratification, a tendency strongly favoured by their bent shape and transverse molecular dipole. This behaviour results in the formation, throughout the N phase, of nanosized molecular clusters encompassing a few hundred molecules and featuring *SmC*-like positional order (cybotactic order), as revealed by the typical four-spot small-angle pattern in XRD experiments [10, 36, 43–45, 47–49]. It is generally assumed that these clusters (cybotactic groups) also exhibit biaxial orientational order. As the clusters transverse axes are randomly oriented around the N director **n**, the cybotactic N phase is macroscopically uniaxial; however, external stimuli can coherently align the clusters, inducing the transition to a macroscopically N_b phase. This peculiar behaviour provides an explanation for the much-debated claims of

biaxiality reported for the N phase of these materials over the past 15 years [10, 41–46].
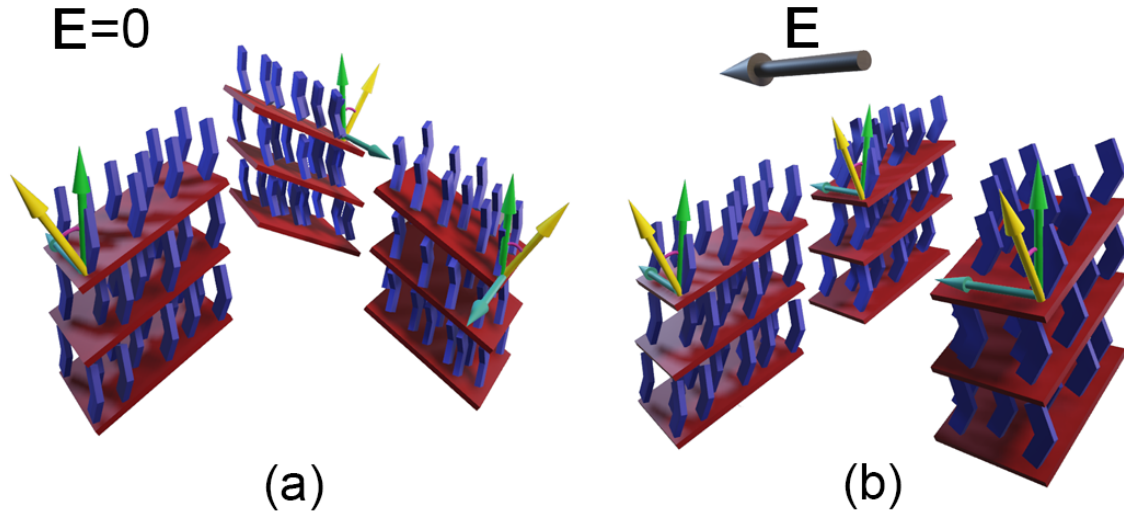
Figure 2.1 Cluster orientation in the tilted cybotactic N phase of BCMs: (a) in the unperturbed state the cluster polarization vectors (light blue arrows) are randomly oriented around the long axis molecular director **n** (green arrows) and the phase polarization vanishes; (b) the cluster polarization vectors are aligned by an external electric field **E** and the phase is macroscopically polar. The yellow arrows indicate the normals to the cluster layers. Reprinted from [40].

If the clusters are also polar, an electric field exceeding a threshold is able to align the cluster dipoles, leading to a switchable, macroscopic polar state (Fig. 2.1) [36, 40]. This type of response is only possible because the field couples with the polarization of a whole cluster rather than with individual molecular dipoles, in this way overcoming thermal disorder. In fact, the coupling energy μE of an ordinary electric field E with a single molecular dipole μ is much lower than the thermal energy $k_B T$, with k_B being the Boltzmann constant and T the absolute temperature. For instance, considering the coupling of a substantial electric field $E = 10^7 \ Vm^{-1}$ with a molecular dipole $\mu = 1$ D at a temperature $T = 500 \ K$, one gets an energy ratio $\frac{\mu E}{k_B T}$ of 0.5×10^{-2}. By contrast, in a cluster N phase, the field would couple with a whole cluster of ordered molecules, so that its aligning effect, magnified by a factor proportional to the average number of molecules per cluster, can prevail over thermal disorder. Indeed, the emerging picture is that all the enhanced properties of the cybotactic N phase of BCMs can be ascribed to the cluster nature of the phase, whose fundamental entities are nanosized clusters rather than individual molecules as in conventional nematics [10, 30–33, 36, 38, 40, 43–53].

In this context, understanding how the details of the molecular structure affect cybotactic

order, and hence the phase macroscopic properties, is a prerequisite to develop new BCMs with tailored unconventional properties. In particular, the design of new BCMs featuring enhanced cybotactic order and stronger, possibly spontaneous, biaxial and polar properties represents an exciting perspective. In addition, both the fundamental study and the technological application of BCMs are strongly hampered by two fundamental limitations: *i*) the high onset temperature of the N phase, typically close to 200 °C; *ii*) the lack of established methods to control the alignment of molecular director(s) by imposing proper surface anchoring conditions, as routinely done in conventional liquid crystals. While the latter problem has stimulated the research activity discussed in Chapter 3, the former has been recently tackled by the addition of lateral groups to the mesogen chemical structure [50, 54–56]. This strategy has led to BCMs entering the N phase at temperatures lower than 100 °C and preserving the N order down to room temperature in a supercooled metastable glassy state. Even more interestingly, these structural modifications also have a profound impact on the molecular packing, promoting a higher level of local biaxial order. This effect has been evidenced by XRD measurements which show an unprecedented splitting of the wide-angle diffraction reflections. As discussed below, this unconventional feature points at two different transverse intermolecular distances and represents the first XRD evidence of local biaxial ordering in the N phase of BCMs. This chapter describes the studies carried out on this family of laterally substituted BCMs, aiming to: *i*) explore the relationship between substitution pattern, thermodynamic properties of the N phase and biaxial ordering, as evidenced by the splitting of the XRD wide-angle reflections; *ii*) investigate their polar properties and dynamic response by means of dielectric spectroscopy.

2.2 The unconventional properties of laterally substituted oxadiazole-based bent-core nematics

The incorporation of lateral substituents onto the mesogen structure is a well know approach to tailor the properties of LC compounds. In particular, this strategy has been applied to BCMs both to lower their N temperature range and to enhance their tendency towards biaxial order [57–59]. Pursuing the same goals, over the last decade the group led by E. Scharrer at the University of Puget Sound synthesized a series of laterally-substituted BCMs, all based on a 2,5-bis(4-hydroxyphenyl)-1,3,4-oxadiazole (ODBP) core [54, 55, 60, 61]. ODBP BCMs are particularly interesting as they are the LC family that was first claimed to show N biaxiality and, consequently, they have been widely investigated [41, 42]. Among the newly synthesized mesogens, the most promising behaviour was exhibited by trisubstituted

derivatives with methyl groups at the 2 position of both outer rings and a third methyl group at either the 2 or the 3 position of one of the inner benzene rings (derivatives **1** and **2**, respectively, in Fig. 2.2) [50, 51, 54].
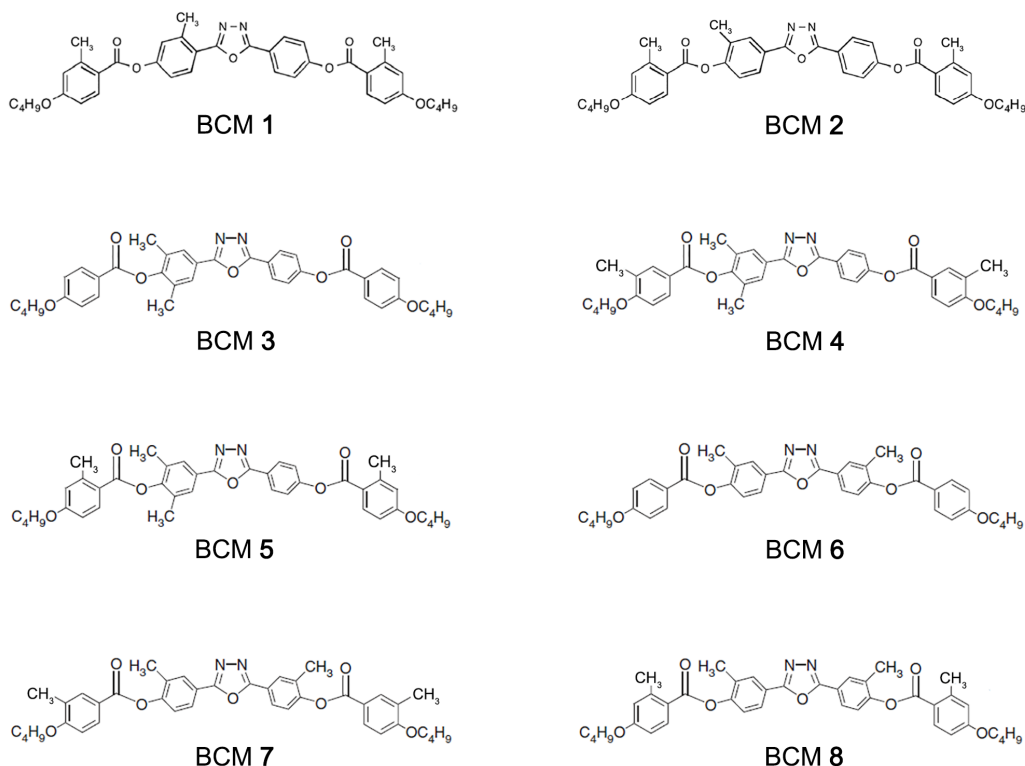
Figure 2.2 Molecular structure of BCMs studied in the thesis.

They showed a number of interesting features that are here summarized:

- They exhibited an enantiotropic N phase with a reduced onset temperature, 88 °C and 120 °C for derivative **1** and **2**, respectively (to be compared with 200 °C in the parent, unsubstituted compound [47]), as shown by the phase diagrams in Fig, 2.3 obtained by DSC.

- The N phase could be supercooled down to room temperature into a metastable, highly viscous state. This behaviour was peculiar of derivatives **1** and **2**; analogue compounds, *e.g.* monomethylated samples without the methyl groups on the outer rings, crystallized on cooling.

- Their N phase exhibited tilted (*i.e.*, *SmC*-like) cybotactic order over the whole N range, as revealed by the characteristic four diffuse spots in the small-angle XRD patterns of both compounds.

- While the previous feature was common to most bent-core nematics, including the parent compound [47], a peculiarity of BCMs **1** and **2** was their wide-angle XRD patterns, consisting of two equatorial (*i.e.*, centred on the normal to the molecular director **n**) reflections. Although broad and partly overlapping, these reflections were clearly distinct, pointing at two different transverse intermolecular distances, $d_1 \approx 4.9$ Å and $d_2 \approx 3.8$ Å (Fig. 2.4 and 2.5), which could be related to the width and thickness of the aromatic rings present in the derivatives' structure.

The last observation, never reported before for other BCMs, represented the first XRD evidence of biaxial ordering in bent-core nematics. In particular, as the molecular shape biaxiality of derivatives **1** and **2** does not differ significantly from that of most bent-core nematics, it must be inferred that the wide-angle splitting uniquely observed in these samples reflects a higher degree of local biaxial order compared to other related compounds. Unfortunately, diffraction measurements were unable to distinguish between local and macroscopic biaxial ordering, mainly because of the difficulty of studying a monodomain biaxial sample by simultaneously aligning both long and short axis molecular directors (a problem that stimulated the study of BCM alignment discussed in Chapter 3). Even though optical measurements seem to exclude macroscopic biaxiality in these derivatives [62], these observations certainly indicate a promising approach towards a stronger biaxial order, which could be potentially extended over a macroscopic length scale through proper molecular engineering.
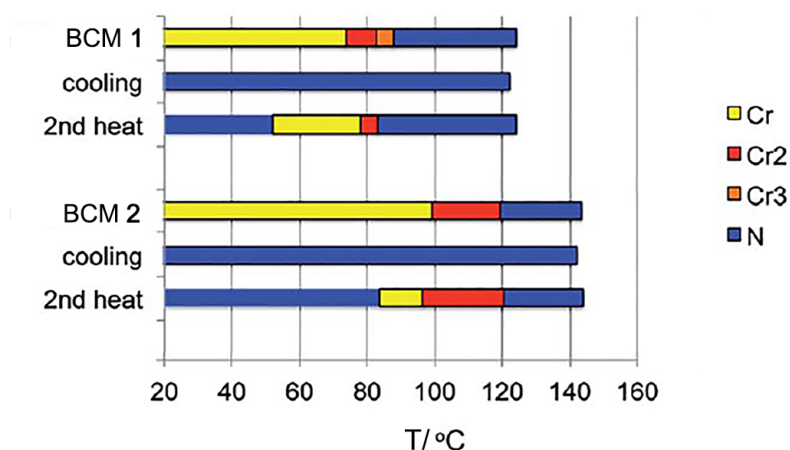
Figure 2.3 Phase behaviour of trimethylated oxadiazole derivatives BCMs **1** and **2**.
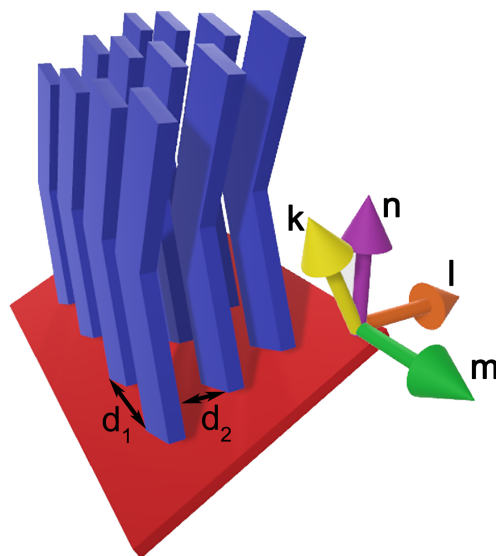
Figure 2.4 Group of molecules in a cybotactic cluster with local biaxial order. **k** indicates
the normal to the *Sm* plane, **n**, **m**, and **l** are the three orthogonal molecular directors; d_1 and
d_2 are the intermolecular distances in the plane normal to **n**

It is interesting to observe that the splitting of the wide-angle XRD pattern, although
more evident at low temperatures, was present throughout the N phase and it was even
discernible in the I phase, indicating a certain persistence of biaxial packing above the
N-I transition temperature [51]. In addition, the effect was clearly related to the particular
substitution pattern of derivatives **1** and **2**, as it was not observed in the parent compound or
in monomethylated analogues, both exhibiting a conventional "single" wide-angle reflection,
corresponding to a transverse intermolecular distance $d \approx 4.5$ Å. This has led to conjecture a
connection with the supercooling behaviour of the same compounds (indeed, supercooling
of the N phase was another unique feature of **1** and **2**): the substitution pattern could affect
the molecular conformation and hamper its mobility by promoting stronger anisotropic
interactions between nearest-neighbor mesogens, in this way preventing the crystallization
and enhancing orientational correlations in the transverse molecular packing.
In an attempt to test this idea and clarify the subtle relationship between substitution pattern,
phase behaviour and biaxial ordering in this class of bent-core nematics, the following
section reports the XRD investigation of the N phase for two new series of dimethylated and
tetramethylated ODBP-based BCMs.
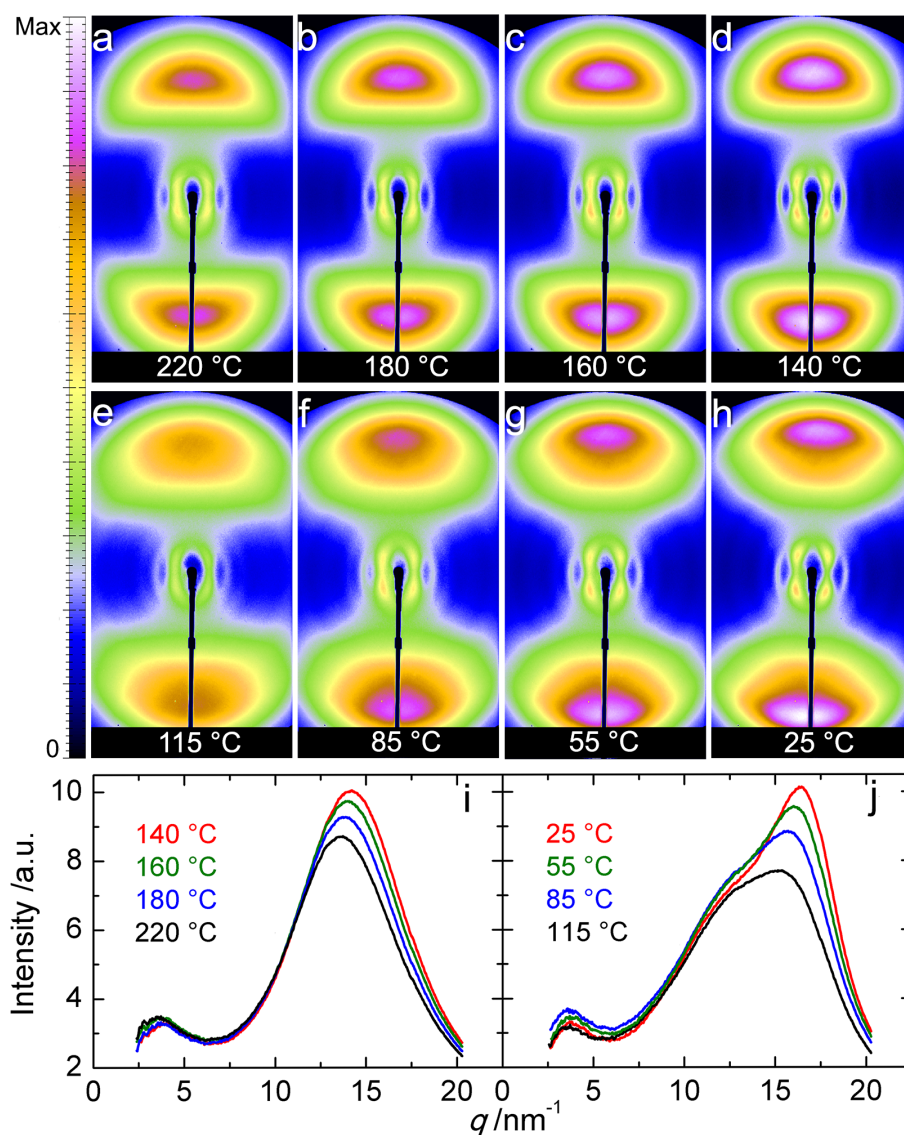
Figure 2.5 XRD patterns of monomethylated compounds without the methyl groups on the outer rings (a-d) and analogous trimethylated BCM **1** (e-h) recorded at selected temperatures while cooling the samples under a horizontal magnetic field and the corresponding equatorial intensity profiles (i) and (j), respectively. Adapted with permission from [50]. Copyright 2019 American Chemical Society.

2.3 Influence of the molecular structure on phase behaviour and biaxial ordering in the nematic phase

The work has been focused on the phase behaviour and structural properties of two new series of laterally substituted BCMs, both based on the well-known ODBP mesogenic core. Compared to the mono- and trisubstituted BCMs previously studied [50, 51, 54], these new compounds have either two or four lateral methyl groups. In one series (derivatives **3**, **4** and **5** in Fig. 2.2), the arrangement of the lateral groups is non-symmetric and in other case (derivatives **6**, **7** and **8** in Fig. 2.2), the groups are symmetrically distributed.

Phase behaviour

The phase behaviour of all compounds, characterized by DSC (heating/cooling rate 10 °C/min), is summarized by the bar graphs shown in Fig. 2.6 and 2.7 for non-symmetric and symmetric derivatives, respectively.
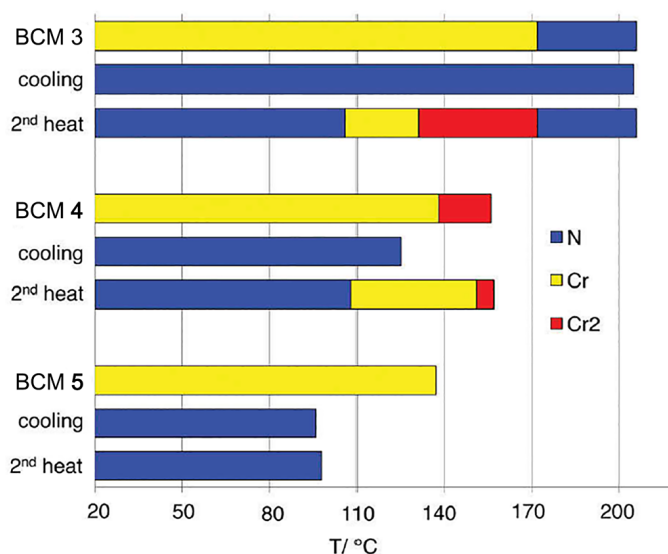
Figure 2.6 Phase behaviour of non-symmetric derivatives BCMs **3**, **4** and **5**.

BCM **3** (non-symmetric) melts to the N phase at 172 °C and enters the I phase at 207 °C. This compound supercools in the N phase all the way to room temperature, with a remarkable temperature drop of more than 200 °C. Notably, this BCM is, to date, the only ODBP-based derivative without any lateral groups on the exterior benzene rings to show this extent of supercooling. This peculiar behaviour is probably related to the exaggerated steric effects

created by the presence of two methyl groups on one of the inner benzene rings and to the
resulting lack of molecular symmetry.

BCM **4** (non-symmetric), *i.e.*, the derivative with methyl groups at the 3 position of the outer
benzene rings, shows monotropic behaviour and melts to the I phase at 156 °C. Upon cooling,
it then enters the N phase at 125 °C and can be supercooled in this phase down to room
temperature. Upon the subsequent heating run, it crystallizes from the N phase at 108 °C,
before clearing at 157 °C.

Also BCM **5** (non-symmetric) exhibits a monotropic phase behaviour, melting to the I phase
at 136 °C. Upon cooling, the sample enters the N phase at 96 °C and supercools to room
temperature. However, differently from **4**, no crystallization occurs upon a second heat: the
derivative remains in the N phase all the way to 98 °C, when it becomes isotropic. To date,
such behaviour has been observed only for two other derivatives (trisubstituted analogues
that contain a halogen substituent) [55]. Notably, the supercooled N phase remains present
for at least one month at room temperature with no obvious textural changes observed under
polarized microscope. However, if the sample in the supercooled N phase is heated at a
slower heating rate (2.5 °C/min instead of 10 °C/min), part of the sample undergoes slow
recrystallization, while the rest of the sample remains in the N phase.

By comparing BCMs **4** and **5** it can be noticed that shifting the methyl groups on the outer
rings from position 3 to 2 leads to a lower isotropization temperature and to a more stable
supercooled N phase. Similar behaviour was also observed for trisubstituted derivatives
[54, 55] and is possibly related to the effects on the molecular conformation of the interaction
between the methyl groups at the 2 position of the outer rings and the nearby carbonyl
oxygens.

The N phase of all of these derivatives is fluid at elevated temperatures, but becomes vis-
cous upon cooling and loses fluidity completely prior to reaching room temperature. This
behaviour is similar to that shown by trisubstituted derivatives **1** and **2**.

To summarise, while all the three non-symmetric derivatives supercool in the N phase to
room temperature, only the dimethylated derivative exhibits enantiotropic behaviour, with
monotropic behaviour shown by the two tetramethylated analogues.

The behaviour of symmetric derivatives is significantly different. BCM **6** (symmetric), the
derivative with only two methyl groups on the inner rings, melts to the N phase at 148 °C
and clears at 209 °C. Upon cooling, the N phase crystallizes at 77 °C.

BCM **7** (symmetric) shows a monotropic phase behaviour and melts to the I phase at 162 °C.
On cooling, the N phase forms at 139 °C and remains present until 80 °C.

BCM **8** (symmetric) also shows monotropic behaviour with N-I transition temperature of
149 °C. But, in this case, the N phase forms at 94 °C on cooling and supercools to room

temperature. Upon the subsequent heat, the compound crystallizes from the N phase at 68
°C. However, the described phase sequence is only observed with cooling rates of 10 °C/min
or faster. If the sample is cooled more slowly, crystallization is observed well above room
temperature. For example, if cooled at 1 °C/min, crystallization occurs within 10 °C of N
phase formation. For even slower cooling rates, such as those used for the XRD measure-
ments discussed below, the I melt crystallizes at about 75 °C, preventing the formation of the
N phase.
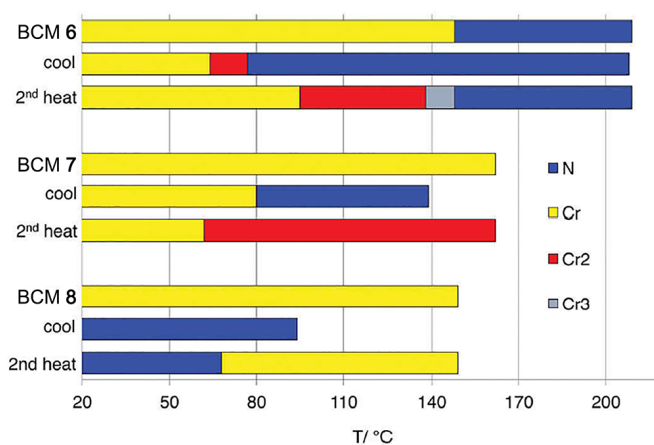
Figure 2.7 Phase behaviour of symmetric BCMs **6**, **7** and **8**.

Comparing the two series of derivatives, it is evident that the non-symmetric substitution
pattern favours the N phase dramatically compared to the symmetric one. It seems that
the lack of symmetry creates a higher kinetic barrier to crystallization, which allows the N
phase to remain present for longer periods of time. Vice versa, a symmetrically substituted
derivative can more rapidly access favourable conformations to allow for crystalline packing.
However, regardless of the symmetric or non-symmetric substitution pattern, all tetramethy-
lated derivatives only exhibit a monotropic N phase. Hence, three methyl groups seem the
maximum number of lateral substituents compatible with an enantiotropic N phase.

Structural properties

In order to probe the effects of the different substitution patterns on the local biaxial order in
this class of compounds, XRD experiments were performed on the N phase. The measure-
ments were carried out at the BM26B DUBBLE beamline at the ESRF (Grenoble, France).
The samples were placed in capillaries (1 mm diameter) and mounted in a hot-stage allowing
application of an aligning magnetic field **B** perpendicular to the incident beam direction and

horizontal in all figures.

All of the investigated compounds showed the four-spot small-angle pattern typical of tilted, *i.e.* *SmC*-like, cybotactic order [10, 36, 43–45, 47–49]. The four-spot pattern was present throughout the N phase, becoming more evident as the temperature decrease. In contrast, the samples manifested significant differences at wide diffraction angles. BCM **4** and **5** (Fig. 2.8 and 2.9) showed a splitting of the wide-angle diffuse crescents reminiscent of that previously reported for the analogous trisubstituted compounds with only one methyl (or halogen) at position 3 of the inner phenyl ring [50, 51, 55]. The splitting is more evident in the intensity profiles taken along the equatorial direction (Fig. 2.8 (d,e) and 2.9 (d,e)): the curves are clearly the superposition of two broad peaks, each one related to a different transverse intermolecular spacing. Fitting the q-scans, obtained by azimuthal integration of narrow (5°) intensity slices orthogonal to **n**, by two Voigt line shapes (indicated in figure as $p1$ and $p2$) provides the spacing values $d_1 = 5.0$ Å and $d_2 = 3.9$ Å at T=120 °C and T=95 °C for BCMs **4** and **5**, respectively. Decreasing the temperature the splitting become more evident reaching the values $d_1 = 5.0$ Å and $d_2 = 3.8$ Å for BCMs **4** and $d_1 = 5.1$ Å and $d_2 = 3.8$ Å for BCMs **5** in the supercooled N phase. The confirmation of biaxial order are the values found. In fact, d_2 is typical of the face-to-face distance between stacked π-systems, while d_1 is closer to the width of a planar aromatic ring (*e.g.* compare with values reported for other systems, such as N_b glasses [63], biaxial *SmA* phases [64], and low temperature N_b phase of shape-persistent V-shaped mesogens [65, 66]). Following Leadbetter *et al*. [67][1], the corresponding correlation lengths ξ_1 and ξ_2 were calculated for each peak as $\xi_{1,2} = 9.92/\Delta q_{1,2}$, with $\Delta q_{1,2}$ being the peak full width at half maximum (FWHM). The correlation lengths are significantly different along the two lateral directions, being around $2d_1$ in the plane of the core, and around $5d_2$ in the orthogonal direction. These values are of the same order of magnitude as the transverse size of cybotactic clusters estimated from the width of the small-angle diffraction spots [54], and, overall, they were similar to those obtained for analogous trisubstituted derivatives, with only one methyl group on the inner phenyl ring [46, 51].

On the other hand, dimethylated BCMs **6** exhibits the conventional wide-angle XRD pattern of calamitic and bent-core nematics: it consists of just one diffuse crescent corresponding to a transverse d and a correlation length ξ ranging from $d = 4.6$ Å and $\xi = 2.5d$

---

[1]Although the spatial extent of positional order, *i.e.*, the correlation length ξ, is always inversely proportional to the peak width, the actual factor at the numerator depends on the model used to describe the system (the 9.92 factor used by Leadbetter is derived from Hosemann's paracrystalline model); therefore, the values of ξ are better considered as order of magnitudes useful to compare different samples, rather than as absolute values (see also [47]).
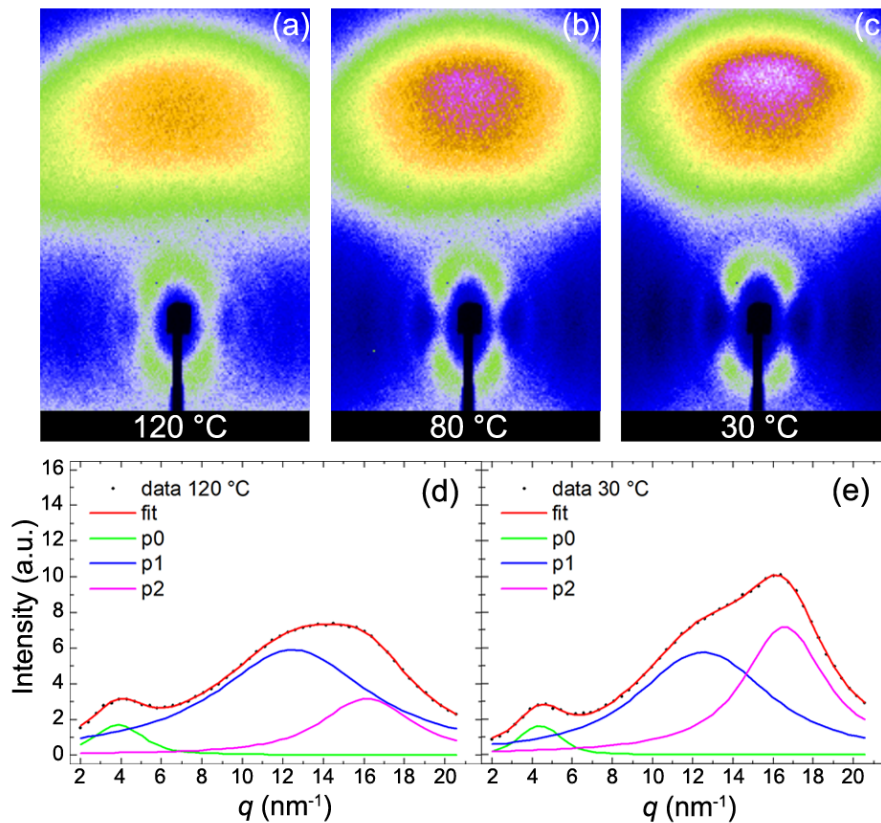
Figure 2.8 (a–c) XRD patterns of BCM **4** taken at different temperatures in the N phase upon application of a horizontal magnetic field aligning the long-axis molecular director **n**. Because of the symmetry of the patterns, only the upper wide-angle crescent is shown. (d,e) Fit of the equatorial intensity profiles ($\perp$**n**) taken from patterns (a) and (c), respectively. The wide-angle peak is fitted with a superposition of two Voigt line shapes, $p1$ and $p2$ (an additional peak, $p0$, models the peripheral scattering from the small-angle reflections). Wide-angle splitting is indicative of local biaxial ordering. Experimental parameters: wavelength $\lambda = 1.03$ Å, sample-to-detector distance $D = 0.200$ m and magnetic field $B = 1.0$ T. Reprinted from [61].

Figure 2.9 (a–c) XRD patterns of non-symmetric BCM **5** taken at different temperatures in the N phase upon application of a horizontal magnetic field aligning the long-axis molecular director **n**. Because of the symmetry of the patterns, only the upper wide-angle crescent is shown. The rotation of the diffraction pattern observed in the highly viscous supercooled N phase on decreasing temperature is due to the competition between the action of the field (horizontal) and the alignment induced by the capillary wall (vertical) [54]. (d,e) Fit of the equatorial intensity profiles ($\perp$**n**) taken from patterns (a) and (c), respectively. The wide-angle peak is fitted with a superposition of two Voigt line shapes, $p1$ and $p2$ (an additional peak, $p0$, models the peripheral scattering from the small-angle reflections). Wide-angle splitting is indicative of local biaxial ordering. Experimental parameters: wavelength λ = 1.03 Å, sample-to-detector distance D = 0.200 m and magnetic field B = 1.0 T. Reprinted from [61].

at T=185°C to $d = 4.3$ Å and $\xi = 2.9d$ at T=65 °C, as confirmed by fitting the intensity profiles shown in Fig. 2.10 (d.e).

Figure 2.10 (a–c) XRD patterns of symmetric BCM **6** taken at different temperatures in the N phase upon application of a horizontal magnetic field aligning the long-axis molecular director **n**. Because of the symmetry of the patterns, only the upper wide-angle crescent is shown. (d,e) Fit of the equatorial intensity profiles ($\perp$**n**) taken from patterns (a) and (c), respectively. The wide-angle peak is fitted with a Voigt line shape, $p1$ (an additional peak, $p0$, models the peripheral scattering from the small-angle reflections). The absence of WA splitting is indicative of uniaxial ordering. Experimental parameters: wavelength $\lambda = 1.03$ Å, sample-to-detector distance $D = 0.136$ m and magnetic field $B = 0.8$ T. Reprinted from [61].

At this stage, it seems that a direct relationship between the supercooled N phase and the wide-angle splitting of the XRD pattern exists because both effects reflect the hindrance of molecular motion caused by the lateral substituents. However, this simple picture contrasts with the results obtained for BCMs **3**. In fact, this disubstituted non-symmetric derivative shows a conventional wide-angle XRD pattern, with non evidence of splitting over the whole N range (Fig. 2.11), even though it exhibit a a supercooled N phase. Within this class of derivatives, this is the first mesogen to show this behaviour. The lack of splitting is evident in the intensity profiles shown in Fig. 2.11 (d,e), whose fitting provides a transverse spacing

$d = 4.6$ Å and a correlation length $\xi = 2.5d$ at T=205 °C, just below the clearing point, and $d = 4.1$ Å and $\xi = 3.5d$ in the supercooled N phase at T=35 °C. Clearly the details of the molecular structure, with their effects on the molecular conformation and intermolecular interactions, affect the property of the phase and the local molecular ordering in distinct, more subtle ways.
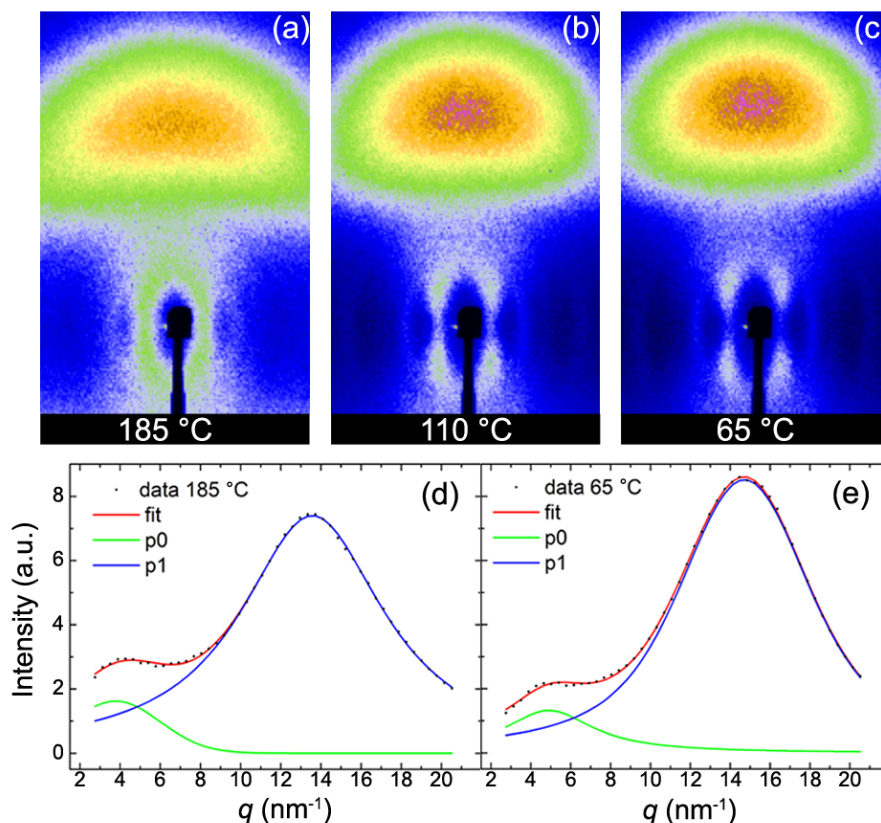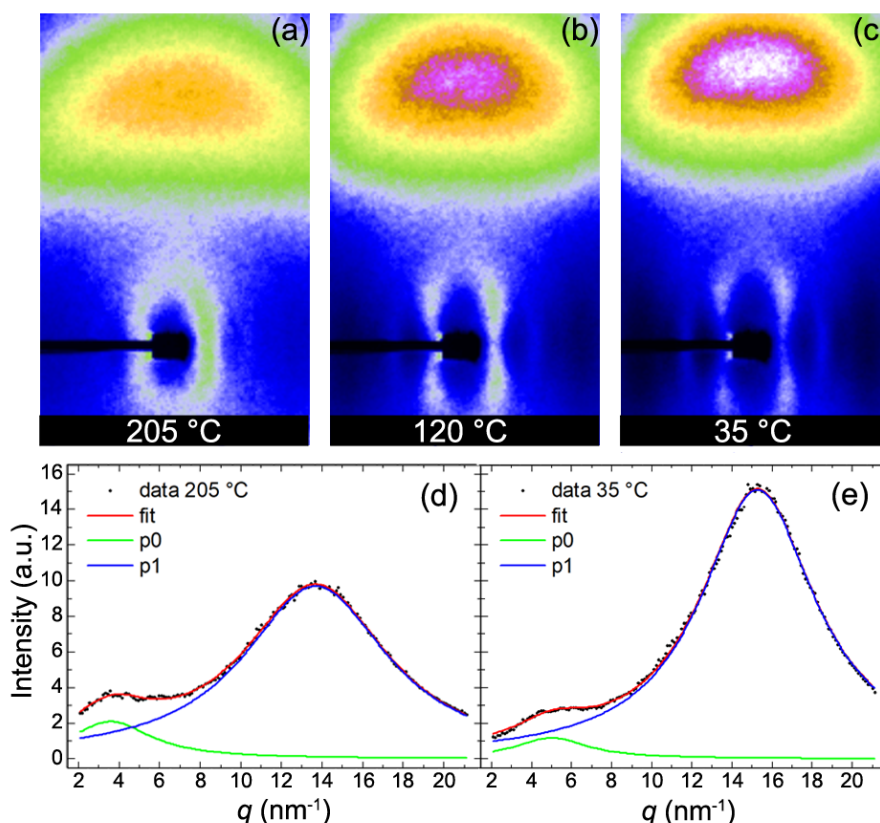

Figure 2.11 (a–c) XRD patterns of non-symmetric BCM **3** taken at different temperatures in the N phase upon application of a horizontal magnetic field aligning the long-axis molecular director **n**. Because of the symmetry of the patterns, only the upper wide-angle crescent is shown. (d,e) Fit of the equatorial intensity profiles ($\perp$**n**) taken from patterns (a) and (c), respectively. The wide-angle peak is fitted with a Voigt line shape, $p1$ (an additional peak, $p0$, models the peripheral scattering from the small-angle reflections). The absence of wide-angle splitting is indicative of uniaxial ordering. Experimental parameters: wavelength $\lambda = 0.827$ Å, sample-to-detector distance $D = 0.172$ m and magnetic field $B = 2.8$ T. Reprinted from [61].

In particular, while the extent of the N phase and its supercooling to room temperature depend in a quite general way on the number of substituents and their symmetric or non-symmetric disposition, the behaviour of BCM **3** suggests that the wide-angle splitting is more strictly related to the presence of substituents on the outer phenyl rings. This conclusion is

consistent with the behaviour of previously studied derivatives [46, 51, 55], and it is further
corroborated by a comparison of the two symmetric derivatives BCM **6** and BCM **8**. In fact,
though crystallization prevented XRD measurements on the N phase of BCM **8**, the XRD
patterns taken in the I phase of the two compounds are clearly different (Fig. 2.12): while
the intensity profile of the wide-angle diffuse ring of BCM **6** exhibits the usual Voigt line
shape centred at $d = 4.8$ Å (Fig. 2.12 (a,b)), the profile of BCM **8** broader and requires an
additional Voigt peak at $d = 3.8$ Å to be adequately fitted (Fig. 2.12 (c,d)). This behaviour,
already reported for trimethylated compounds [51], suggests that molecular packing in the N
and, to a lesser extent, in the I phase varies with the mesogen conformation, the latter being
strongly influenced by the presence of substituents on the outer phenyl groups.
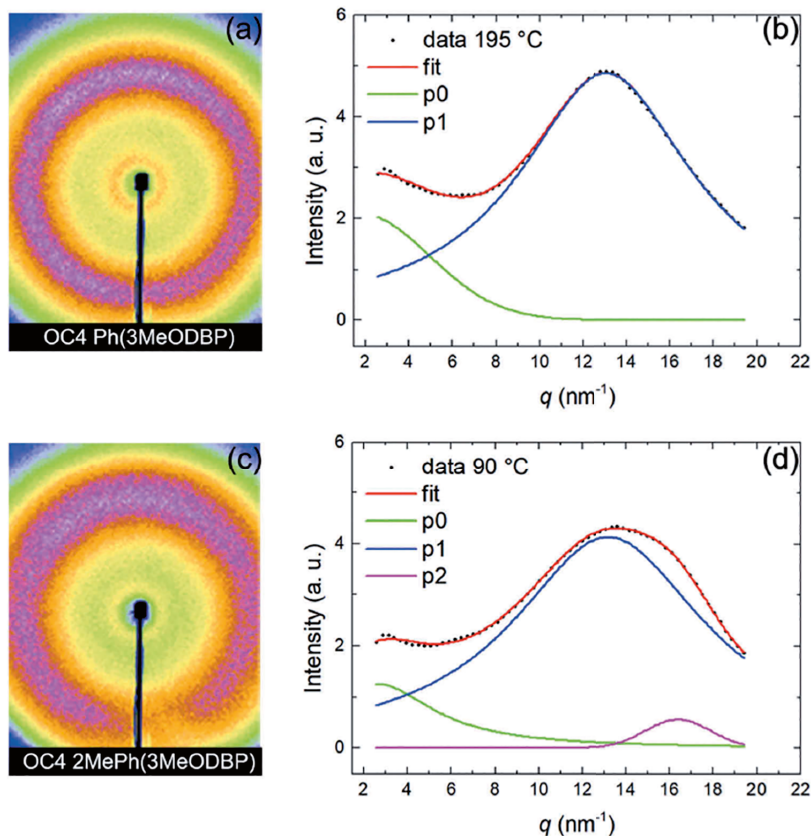
Figure 2.12 (a) XRD pattern of symmetric BCM **6** taken on cooling at $T = 195°C$ in the I phase and (b) corresponding wide-angle radial intensity profile fitted by a Voigt line shape, $p1$. (c) XRD pattern of symmetric BCM **8** taken on cooling at $T = 90°C$ in the I phase and (d) corresponding wide-angle radial intensity profile fitted by two Voigt line shapes, $p1$ and $p2$. In both (b) and (d) an additional Voigt Peak, $p0$, models the small-angle scattering. Wide-angle splitting, indicative of local biaxial ordering, is only observed for the derivative with lateral groups on the outer benzene rings. Experimental parameters: wavelength $\lambda = 1.03$ Å, sample-to-detector distance $D = 0.136$ m and magnetic field $B = 0.8$ T. Reprinted from [61].

2.4   Polar order: a dielectric spectroscopy investigation

In the introduction to this chapter it has been already mentioned how the presence of polar cybotactic clusters in the N phase of some BCMs can results in a ferroelectric-like response to switching electric fields. The discovery of this highly unconventional behaviour in bent-core nematics and its connection to cybotaxis have been reviewed in the authored paper [40]. The first observation of this effect - never recorded before in conventional nematics - was reported by Francescangeli *et al.* in 2002 [68] for the BCM reported in Fig. 2.13. This mesogen exhibits a high temperature N phase between 140 and 263 °C, above an underlying *SmC* phase. It is based on an asymmetric heterocyclic central unit, a 3,5-disubstituted 1,2,4-oxadiazole, which imparts the molecule a core bend angle of $\sim 140°$ and a molecular dipole $\mu = 5.97$ D, tilted by $\alpha \approx 33.5°$ with respect to the transverse x axis (Fig. 2.13).
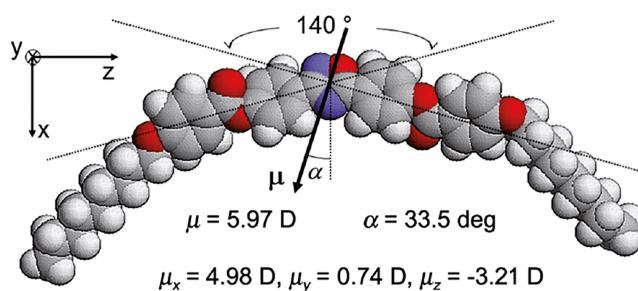
Figure 2.13 Single molecule geometry and molecular dipole μ for the BCM which exhibits a ferroelectric-like response to switching electric fields. The first observation of this effect was reported for this mesogen. The model was obtained by combining density functional theory calculations and atomistic molecular dynamics simulations, as describe in [36]. Reprinted from [40].

The ferroelectric-like switching response of the mesogen was studied through repolarization measurements, *i.e.* by applying a driving voltage waveform across the LC cell and measuring the current induced in the circuit by the switching sample polarization. The interpretation of the switching as due to the collective reorientation of polar clusters was suggested by the analysis of the XRD data, providing evidence of tilted cybotactic order, and confirmed by the results of molecular dynamics simulations [36]. Subsequently, a similar polar response was reported by other groups for a number of other BCMs [37, 69–71]. In most cases, additional support to the polar cybotactic model came from dielectric spectroscopy measurements, which showed a characteristic low frequency peak associated to the collective reorientation of polar clusters.

Within this framework, aim of this study is to investigate the polar properties of laterally substituted BCMs by means of dielectric spectroscopy. The investigated compounds are the

trisubstituted BCMs **1** and **2**. They were chosen for their enantiotropic low temperature N phase, which can also be supercooled to room temperature in a metastable state. By XRD diffraction they exhibit a typical four-spot pattern in the small-angle region, indicative of tilted cybotactic order, and the splitting of the wide-angle diffuse crescents associated to local biaxial order (Fig. 2.5) [50, 54].

The dielectric spectroscopy experiments were performed at the Department of Physics of the UNICAL in collaboration with the group of Prof. N. Scaramuzza. For the measurements, the LC was confined in 10 μm-thick cells consisting of two conducting ITO-coated glass plates (electrode area of 10 mm $\times$ 10 mm) covered with an aligning layer of obliquely evaporated SiO$_x$ so as to induce a planar alignment of the N director **n**. As BCMs exhibit a negative dielectric anisotropy, with a transverse molecular dipole, this configuration allows probing the LC dielectric properties in the direction orthogonal to the long axis N director **n**. The use of SiO$_x$, instead of more common organic aligning agents such as rubbed polyimide, ensures the absence of spurious effects, such as those due to charge adsorption/desorption processes. The LC was injected into the cells in the I phase by capillary forces. An EG&G 273A galvanostat-potentiostat/impedance-meter was used to measure the real (*ReZ*) and imaginary (*ImZ*) parts of impedance. The instrumentations, controlled by the impedance software M398, worked in the frequency range 1 Hz-100 kHz with an applied voltage of 500 mV (root means square); no bias voltage was applied. The samples were placed in a CaLCTec FB150 programmable temperature hot stage (temperature stability of $\pm$0.1 °C) to perform dielectric measurements as a function of temperature. The dielectric spectra were acquired over the N temperature range, on both heating and cooling.

The impedance-meter outputs are the real and the imaginary part of the impedance; they allow to calculate the real and the imaginary part of the complex dielectric permittivity $\varepsilon^*(f) = \varepsilon'(f) - i\varepsilon''(f)$ through the following equations:

$$\varepsilon'(f) = \frac{ImZ}{ImZ^2 + ReZ^2} \frac{d}{\varepsilon_0 A} \frac{1}{2\pi f} \, ,$$
$$\varepsilon''(f) = \frac{ReZ}{ImZ^2 + ReZ^2} \frac{d}{\varepsilon_0 A} \frac{1}{2\pi f} \, ,$$
(2.1)

where Z is the impedance, d the cell thickness, A the electrode area and f the applied voltage frequency.

The analysis of the imaginary part of the dielectric permittivity in the N phase has been carried out using the Havriliak-Negami (HN) equation with the addition of a low frequency conductivity contribution due to the presence of ionic charges [72]:

$$\varepsilon''(f) = \varepsilon_\infty + \sum_j \frac{\Delta \varepsilon_j}{[1 + (if\tau_j)^{\alpha_j}]^{\beta_j}} - \frac{i\sigma}{\varepsilon_0(f)^n} \ , \tag{2.2}$$

where f is the frequency, ε_∞ is the high frequency limit of permittivity, $\Delta \varepsilon_j$ is the dielectric strength of the j-th relaxation process, τ_j is the j-th process relaxation time, corresponding to a relaxation frequency $f_j = 1/\tau_j$, α_j and β_j are shape parameters ranging between 0 and 1 and describing the broadening and asymmetry of the j-th process dielectric dispersion curve, σ is the dc sample conductivity and n is a fitting parameter responsible for the slope of the conductivity contribution. The imaginary part ε'' of the dielectric spectra measured in the fluid N phase of BCM **1** both on heating and cooling is shown in Fig. 2.14(a) and 2.14(b), respectively. Analogous data for BCM **2** are shown in Fig. 2.15 (a) and 2.15(b).
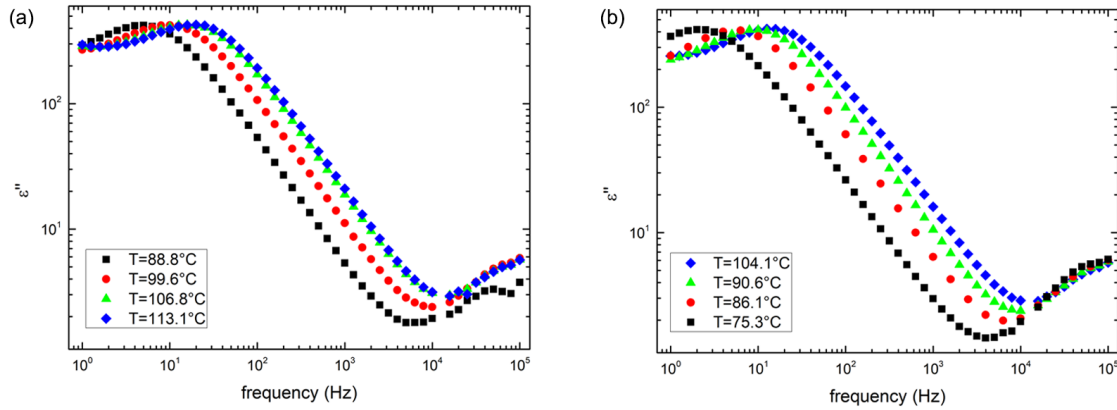
Figure 2.14 Imaginary part of the dielectric spectrum of BCM **1** in the N phase on heating (a) and cooling (b).

The spectra of the two samples can be well fitted by a two-process model consisting in a low frequency mode HN1 and a high frequency mode HN2, as shown in Fig. 2.16 (a) and (b) for two representative curves of BCM **1** and **2**, respectively. The fitting parameters for the two modes and the conductivity contribution are summarized in Tab. 2.1 and 2.2, for BCM **1** and **2**, respectively.

HN2 is a high frequency mode, with a characteristic frequency $f_2 \approx 100$ kHz and a dielectric strength $\Delta \varepsilon_2 \approx 11$. These values, which are typical for molecular processes, indicate that HN2 is due to the mesogen reorientation around the long molecular axis.

The lower frequency mode HN1 is more interesting. Its characteristic values of frequency and dielectric strength are shown as function of temperature in Fig. 2.17 (a) and (b) for BCMs **1** and **2**, respectively.
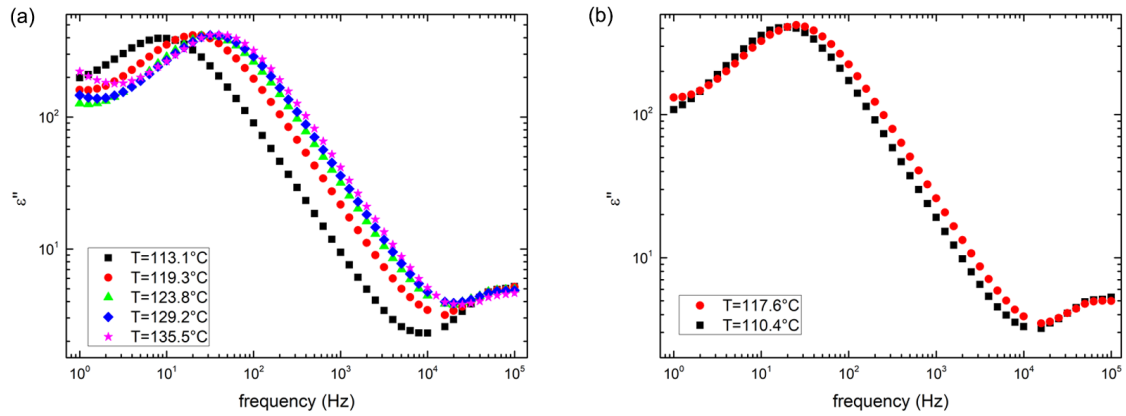
Figure 2.15 Imaginary part of the dielectric spectrum of BCM **2** in the N phase on heating (a) and cooling (b).
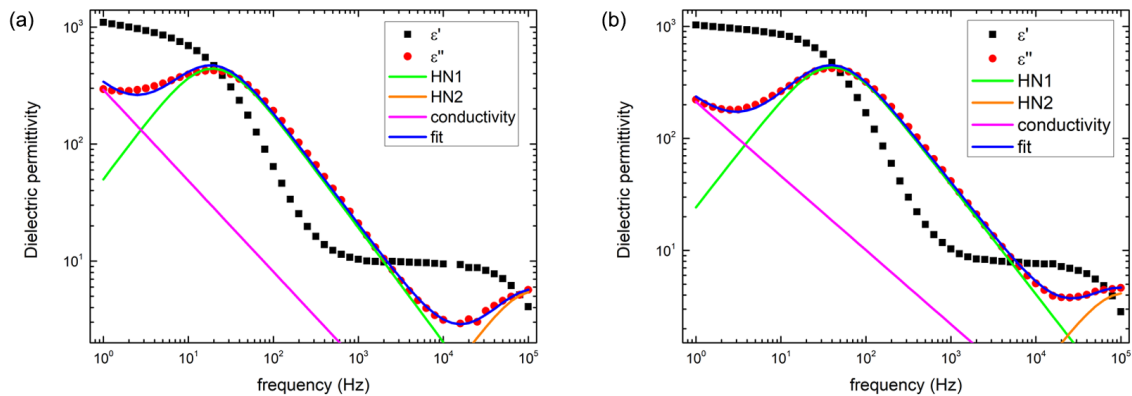
Figure 2.16 Fit of the imaginary part of the dielectric spectrum for two representative curves of BCMs **1** (a) and **2** (b).

Table 2.1 Fitting parameters of the conductivity term and relaxation processes of BCM **1** on heating and cooling.

	cond.		HN1				HN2			
T (°C)	σ (nS/m)	n	f_1 (Hz)	$\Delta\varepsilon_1$	α_1	β_1	f_2 (kHz)	$\Delta\varepsilon_2$	α_2	β_2
88.8	8.71	0.95	5.89	825.8	0.99	1.00	34.7	14.0	0.95	0.30
99.6	9.12	0.86	10.72	886.7	0.98	1.00	100.0	11.3	1.00	1.00
106.8	0.10	0.78	16.60	920.5	0.97	1.00	109.7	10.8	1.00	1.00
113.1	0.11	0.78	19.50	915.7	0.98	1.00	120.2	11.0	1.00	1.00
104.1	8.32	0.80	14.45	907.7	0.97	1.00	104.7	10.9	1.00	1.00
90.6	7.08	0.85	10.00	879.2	0.97	1.00	100.0	11.3	1.00	1.00
86.1	6.17	0.92	6.31	847.3	0.97	1.00	38.0	56.3	1.00	0.10
75.3	8.13	1.06	2.82	779.7	0.95	1.00	91.2	12.9	0.96	1.00

Table 2.2 Fitting parameters of the conductivity term and relaxation processes of BCM **2** on heating and cooling.

	cond.		HN1				HN2			
T (°C)	σ (nS/m)	n	f_1 (Hz)	$\Delta\varepsilon_1$	α_1	β_1	f_2 (kHz)	$\Delta\varepsilon_2$	α_2	β_2
113.1	5.25	0.86	9.77	838.2	0.97	1.00	83.2	10.1	1.00	1.00
119.3	2.95	0.61	20.42	896.2	0.98	1.00	95.5	9.7	1.00	1.00
123.8	3.09	0.67	30.20	902.1	0.97	1.00	91.2	9.2	1.00	1.00
129.2	3.80	0.66	34.67	900.3	0.97	1.00	93.3	8.9	1.00	1.00
135.5	6.31	0.66	39.81	896.3	0.98	1.00	107.2	8.3	1.00	1.00
117.6	2.14	0.73	18.62	892.5	0.97	1.00	85.1	10.1	1.00	1.00
110.4	2.24	0.60	23.99	908.1	0.97	1.00	93.3	9.4	1.00	0.10
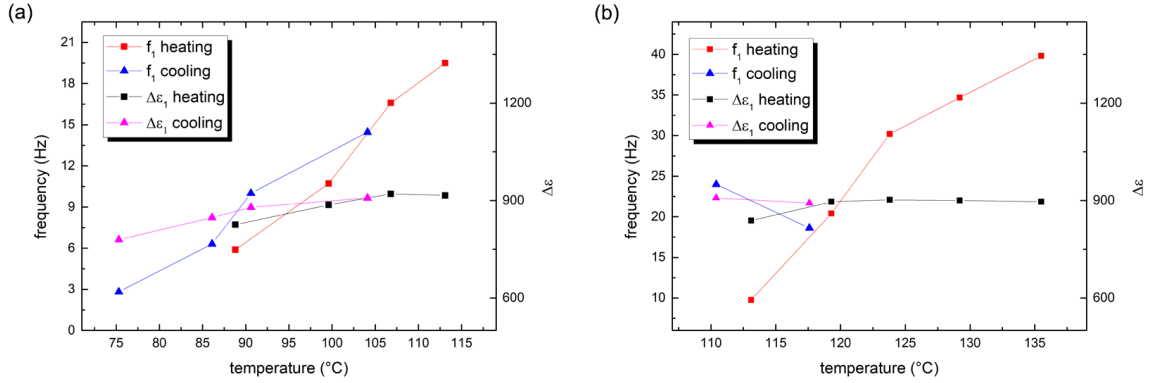
Figure 2.17 Frequency and dielectric strenght of the HN1 mode of BCMs **1** (a) and **2** (b).

For BCM **1**, the frequency f_1 ranges between 3 and 20 Hz, clearly increasing with the increasing temperature, while the dielectric strength is $\Delta\varepsilon_1 \approx 900$, relatively independent of temperature. Data for BCM **2** are similar, with f_1 increasing with the temperature (on heating) from 10 Hz to 40 Hz and the dielectric strength assuming values like those of the previous sample $\Delta\varepsilon_1 \approx 900$. Contrary to the trend described above, a slight, anomalous increase of f_1 is observed on cooling for BCM **2**. Apart from this minor deviation, the two samples do not show significant differences and the slightly larger value of f_1 for BCM **2** is probably due to the higher temperature range of its N phase. Both the frequency range and the large dielectric strength of mode HN1 suggest the collective nature of the underlying dielectric process, namely the reorientation of polar cybotactic clusters [37, 69–71]. In particular, the values of $\Delta\varepsilon$ are exceptionally large in the N phase and can only be ascribed to the reorientation of polar clusters. As the dielectric strength of a reorientation mode can be assumed to be proportional to the number of molecules involved in the process, the number of molecules per cluster can be estimated considering the ratio between the dielectric strength of the collective mode HN1 and that of the single-molecule process HN2, providing a value $\frac{\Delta\varepsilon_1}{\Delta\varepsilon_2} \approx 10^2$ molecules per cluster. Such a value is in a good agreement with the typical values obtained by the analysis XRD patterns, through the measure of the characteristic correlation lengths associated to cybotactic order [47–49]. Finally, the increase of the relaxation frequency f_1 with the temperature is easily explained with the temperature dependence of the sample viscosity.

2.5   Conclusions

Investigation of laterally methylated bent-core nematics provides new insights into the effect of lateral substituents on the mesophase properties as well as on the local molecular

packing. In particular it was found that: *i*) non-symmetrically substituted derivatives show a stronger propensity for supercooling the N phase into a room temperature glassy state than symmetrically substituted compound; *ii*) the splitting of the wide-angle XRD pattern, indicative of two different transverse intermolecular distances, hence of local biaxial order, is only observed in derivatives with methyl substituents on the outer phenyl rings, regardless of the supercooling properties of the phase. These findings suggest useful clues to guide the research effort towards the synthesis of novel BCMs exhibiting a low temperature N phase with spontaneous macroscopic biaxial order.

The relaxation behaviour of dielectric permittivity has been determined in the frequency range from 1 Hz to 100 kHz in the N phase of two trimethylated BCMs. From dielectric spectra emerge the presence of two distinct modes: the HN2 high frequency mode related to a molecular reorientation around the long molecular axis and the HN1 low frequency mode which suggests the collective reorientation of the molecules due to the switching of cybotactic polar clusters. The next step is to improve these results and modify the molecular structure to increase the polar order. The group led by Prof. E. Scharrer synthesised a new mesogen substituting the methyl group in the inner phenyl ring of BCMs **2** with a much polar NO_2 group, in order to obtain the ferroelectric N phase even when the electric field is switched off. The research is continuing in this direction and preliminary promising measurements on this mesogen are performed. In fact, such BCM exhibits interesting features described in this chapter, *i.e.* the splitting of the wide-angle XRD diffuse crescents and the supercooled N phase.

Chapter 3

X-ray probing of surface anchoring in thin films of bent-core mesogens

3.1 Introduction

The search for the N_b phase represents one of the most fascinating fields of study within the LC community, with arguments presented both in favour [41, 42, 50, 73–94] and against [48, 95–102] its existence. Since Freiser's theoretical prediction [11], the N_b phase has been experimentally observed only in lyotropic LCs [74, 103], whereas it still remains elusive in thermotropic LCs. Among the latter, BCMs have been widely considered the most promising candidates for N biaxiality because of the symmetry of their molecular structure, characterized by three different molecular axes. Although N_u and N_b phase exhibit drastically different sets of symmetry-allowed topological defects that can be used for phase identification [77, 99, 104–106], textural features of regular samples, such as flat cells, might be similar in the two phases, as shown by Chiccoli *et al*. [104]. After decades of failing attempts, in the early 2000s, a few BCMs have been claimed to exhibit the N_b phase, a conclusion supported by XRD [42, 79], NMR [41] and electro-optical studies [80–83]. However, after the initial enthusiasm [107], these conclusions have been widely questioned [48, 95, 99, 100] with the intimate nature of the supposed biaxiality being eventually reconsidered [10]. For instance, it has been recently demonstrated that previous claims of BCM N biaxiality based on optical measurements were probably caused by misinterpreted surface anchoring transitions in uniaxial samples that mimicked the behaviour of biaxial samples [62, 96]. Although the assessment of the N_b phase in BCMs is still a debated topic, a general consensus is finally emerging: *i*) no undisputable proof of proper - *i.e.* spontaneous and macroscopic - biaxiality has been provided so far for the N phase of BCMs; *ii*) most claims of N biaxiality in BCMs

should be attributed either to erroneous interpretations of experimental data (often due to ill-founded assumptions on the LC alignment) or to the action of external fields (electric, magnetic, mechanical) which can extend the local biaxiality of nanosized cybotactic clusters to a macroscopic length scale. While understanding the intimate nature of cybotaxis and short-range intermolecular order in BCMs can provide a pathway towards the engineering of new mesogens exhibiting proper biaxial order, a prerequisite to any experimental investigation and technological exploitation of these materials is the ability to control the director(s) alignment by imposing proper surface anchoring conditions.

For conventional (rod-like) LCs, the average molecular orientation can be efficiently controlled (uniformly over very large areas) by treating the confining surfaces with specific alignment layers (*e.g.*, surfactants, rubbed polyimide films, oblique SiO_x depositions) (see Section 1.1.7). Although the microscopic mechanism behind each aligning approach is not always fully understood, a very fine control over the anchoring conditions can be usually obtained. The superficial alignment is then extended to the bulk (over a length scale of microns) by the LC elastic properties. Unfortunately, aligning BCMs by these conventional approaches has proved quite challenging. For instance, while the surfactant Dimethyloctadecyl[3-(trimethoxysilyl)propyl]ammonium chloride (DMOAP) is widely used to get homeotropic alignment in rod-like LCs [108], it is found to induce a planar alignment in bent-core nematics. This is clearly shown by the GIWAXS pattern in Fig. 3.1: it shows the grazing-incidence diffraction pattern from a film (less than 1 μm thick) of BCM **1** spin-coated over a silicon substrate treated with DMOAP. The measurement, taken in the N phase at $T =$ 115 °C, shows a wide-angle diffuse reflection centred along the normal to the substrate at $q_z \approx$ 15 nm^{-1}, corresponding to an intermolecular spacing $d \approx 4$ Å. Contrary to the expectation, this type of pattern points unequivocally at a planar LC alignment, *i.e.* with the molecular long axis lying in the plane of the film.

Given these difficulties, the development of surface treatments able to finely control the alignment of molecular director(s) in BCM films, possibly establishing biaxial anchoring conditions, is a fundamental step in the study of BCMs. In particular, it is a prerequisite for the unequivocal identification, and subsequent technological application, of a true N_b phase. In this framework, the deposition of Langmuir films of BCMs on proper substrates could provide both ideal systems for the study of LC anchoring on the molecular scale and a suitable approach to get aligning surfaces with controlled anchoring conditions [109–119]. Langmuir films are molecular films formed at the air-water interface that can be then transferred onto solid substrates (see next section for further details) [120].

Compared to spin-coating, deposition from Langmuir films results in a much finer control of the film thickness and structure and it is thus more suitable to study the anchoring properties
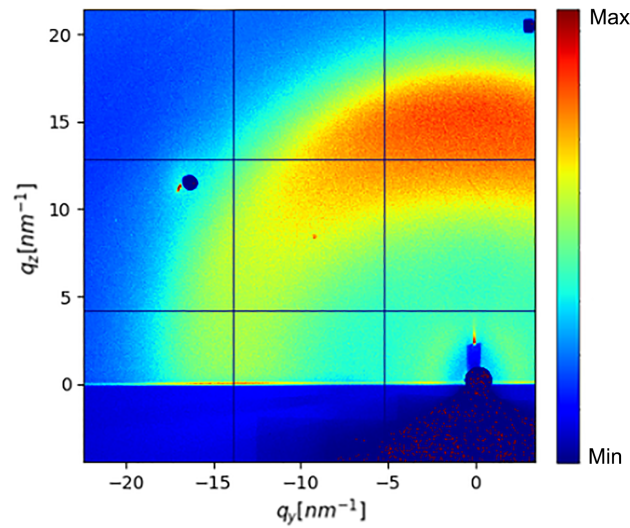
Figure 3.1 GIWAXS pattern of the BCM **1**, spin-coated film on silicon substrate ((100)-cut *n*-doped) previously treated with surfactant DMOAP, a well-know agent to induce homeotropic alignment. Unexpectedly, the pattern indicates a planar alignment. Experiment performed at the ID03 beamline of the ESRF with the following parameters: wavelength $\lambda = 0.55$ Å, sample-to-detector distance $D = 1395$ mm, beam size $= 180 \times 28$ μm^2 (width $\times$ height), incident angle $\alpha_{in} = 0.09^o$ and exposure time t = 10 s.

of interfacial LC layers and their critical effect on the bulk LC alignment. In addition, this deposition technique is inherently anisotropic (compression of the film over water and dipping directions of the substrate set an in-plane preferential direction) [36, 40], it can possibly force the LC molecules to adopt a biaxial ordering, with both long and short molecular axes uniformly aligned with respect to the substrate. Such biaxial anchoring conditions, not achievable at present with conventional alignment techniques, would be of extreme interest from both a fundamental and technological point of view.

This chapter reports the deposition of Langmuir films of BCMs (single and multiple depositions on silicon substrates) and their characterization by means of X-ray and complementary techniques. The nanoscale structure of the films is resolved in both cases: films obtained by a single deposition show a bilayer structure with the bottom molecules flat and the top molecules upright; on the other hand, multiple deposition films exhibit an in-plane anisotropy of the molecular ordering which has never been reported in the literature for these systems.

3.2 Experimental

3.2.1 The bent-core mesogen

The experiments discussed in this chapter are all performed using the laterally substituted BCM **1** already mentioned in Chapter 2. Its chemical structure, phase transition temperatures, and molecular geometry are shown in Fig. 3.2. The compound is a trimethylated ODBP mesogen characterized by a bending angle of $\sim 124°$ and a molecular length $L \approx 34$ Å. On heating, it enters the N phase at 88 °C, the lowest value among this class of laterally substituted BCMs, while on cooling the N phase can be supercooled down to room temperature into a metastable glassy state. As discussed in Chapter 2 (see Fig. 2.5), its wide-angle XRD patterns show a splitting of the transverse reflection indicative of two distinct transverse intermolecular distances, hence of local biaxial ordering.
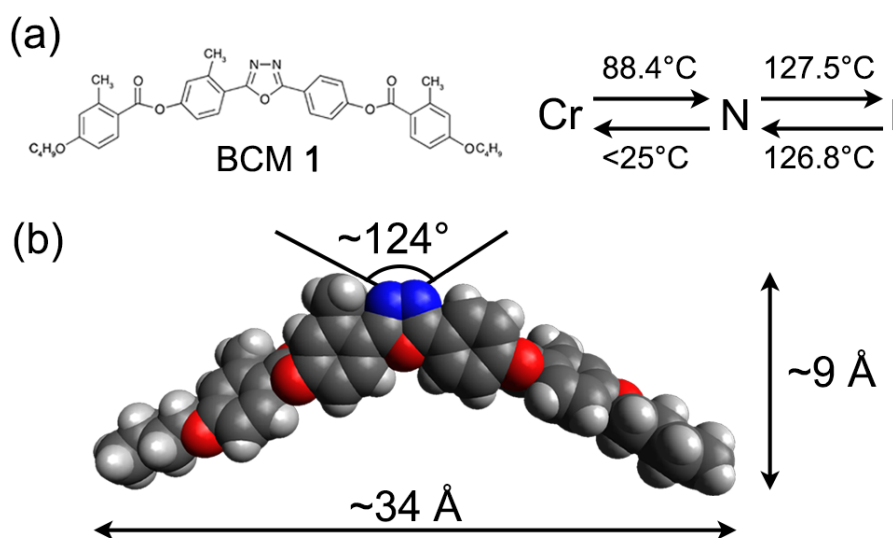
Figure 3.2 (a) Chemical structure and phase diagram of the BCM **1**, both on heating (rightward arrow) and cooling (leftward arrow). (b) 3D model of the molecule with typical dimensions and bending angle.

3.2.2 Langmuir-Blodgett/Langmuir-Schaefer depositions and BAM measurements

A Langmuir film is formed at the air-water interface by dispersing insoluble molecules over water; compression of the film by moving barriers determines the molecular arrangement on the water surface, which can then be transferred over a solid substrate. The stability

of a Langmuir film and the orientation of the molecules critically depend on the interplay between the molecular hydrophobic and hydrophilic moieties. In fact, Langmuir films are conventionally prepared with amphiphilic molecules. By contrast, typical BCMs have two hydrophobic alkyl tails of variable length and a hydrophilic aromatic core. The films were prepared using the Langmuir trough NIMA available in the PSCM laboratory of the ESRF, Grenoble (France), equipped with control barriers, a Wilhelmy plate pressure sensor and a Brewster angle microscope (BAM). BAM microscopy uses a p-polarized laser beam ($\lambda =$ 532 nm) to illuminate the liquid surface at an incidence angle equal to the Brewster angle of the water-air interface. In this condition the reflectance from a pure water-air interface is null, so all the non-zero signal in the CCD camera of the apparatus is due to the reflectance of the Langmuir layer.
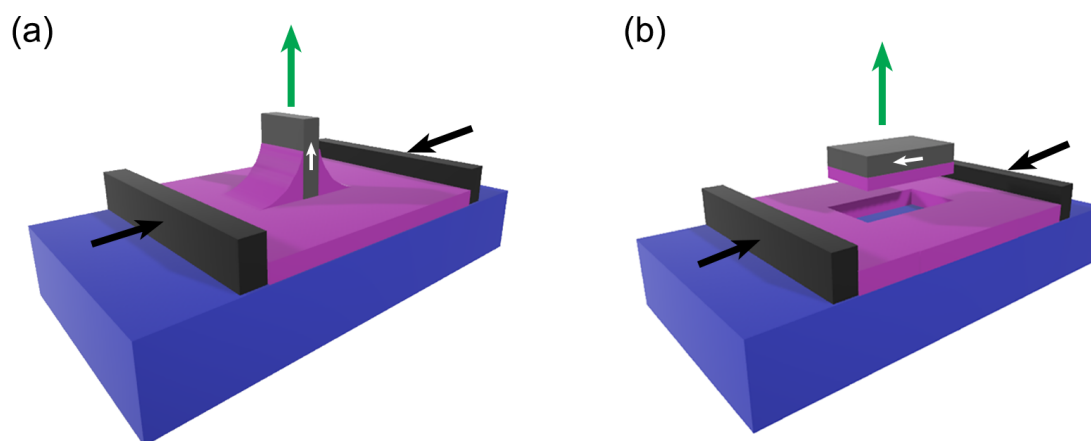
Figure 3.3 Schematic drawing of the experimental set-up for Langmuir-Blodgett (a) and Langmuir-Schaefer (b) techniques. The Langmuir film (in violet) is on the top of the water (in blue). For the Langmuir-Schaefer depositions, the silicon orientation was chosen in such a way that the barrier compression direction (black arrows) was parallel to the LB dipping direction (green arrow in (a) marked by a white arrow on the sample) chosen for the first layer. The green arrows are the dipping directions for the two techniques.

The BCM was dissolved in chloroform at 0.1 mg/ml. The solution was spread on the top of the Langmuir trough filled with pure water (PURELAB Flex ELGA, resistivity of 18.2 MΩ/cm) at an initial area per molecule $S \approx 130 \div 140$ Å^2. The films were deposited on silicon substrates: (100)-cut n-doped for single depositions and (111)-cut p-doped for

multiple depositions[1], both previously treated with piranha solution. Single deposition films were deposited using the Langmuir-Blodgett (LB) technique: the substrate was vertically immersed in the water before spreading the BCM solution; hence, the solution was spread and the barriers were closed until the desired deposition pressure was reached; finally, a motor extracted the substrate from the water with the BCM molecules remaining attached on the silicon surface. Multiple deposition films were prepared combining the LB technique described above for the first layer, and then depositing additional 28 layers (for a total number of layers of 29) using the Langmuir-Schaefer (LS) geometry: in this case, the silicon substrate, kept parallel to the water surface, was manually lowered until getting in contact with the Langmuir film, which was hence transferred onto the substrate. During the LS depositions the sample orientation was chosen in such a way that the barrier compression direction was parallel to the LB dipping direction chosen for the first layer. In Fig. 3.3 is shown a schematic drawing of two techniques. The deposition pressure for single deposition films was $\Pi = 12$ mN/m, corresponding to an area per molecule $S \approx 40$ Å^2, while multiple deposition films were prepared setting, for all layers, a target pressure $\Pi = 30$ mN/m, corresponding to $S \approx 32$ Å^2/molecule. After the deposition, excess water was left to evaporate before performing any characterization of the films.

3.2.3 Atomic Force Microscopy

AFM (Bruker Multimode 8 with Nanoscope V controller) was used to check the morphology and the uniformity of single deposition films. Data were acquired in tapping mode, using silicon cantilevers (model TAP150, Bruker).

3.2.4 X-ray reflectivity

XRR was used with single deposition films to determine the electron density profile normal to the film surface, the layer thickness and correlated roughness. XRR experiments were performed at the ID03 beamline of the ESRF, Grenoble (France). The samples were placed on a high precision hexapod support while a photon-counting detector MAXIPIX, developed by the ESRF, was mounted on a z-axis vertical diffractometer. The beam width and height were 200 μm and 40 μm, respectively, while the beam wavelength was $\lambda = 0.55$ Å. The measurements were performed at room temperature.

---

[1]The silicon (111)-cut prevents the appearance of Bragg reflections in the q-range of interest for GIWAXS experiments.

3.2.5 GIWAXS experiments

The in-plane and out-of-plane order of multiple deposition films was investigated by means of GIWAXS. The measurements were carried out at the NCD-SWEET beamline of the ALBA synchrotron, Barcelona (Spain). The sample was mounted on a rotating stage in order to investigate the film under different azimuthal orientations. The wavelength was λ = 1.55 Å and the beam size was 111 $\times$ 12 μm^2 (width $\times$ height). The sample-to-detector distance was D = 198.4 mm and the fixed incident angle was set at α_{in} = 0.16° with an exposure time of 30 s. The patterns were recorded at room temperature.

3.3 Single deposition films

A typical isotherm (*i.e.*, a Π vs S curve) taken during a full compression/expansion cycle of the BCM Langmuir film is shown in Fig. 3.4 together with a sequence of BAM images. After spreading, the decrease in energy associated to molecular aggregation overcomes the entropy loss and the molecules start forming floating islands, freely movable over the water surface (Fig. 3.4(a)). Within these islands, it can reasonably be assumed that the molecules tend to lie flat on the water surface, with the hydrophilic carbonyl oxygens of the mesogen core close to the water [121] and the hydrophobic end-chains lifted up. This picture is also supported by the relatively large value of area per molecule.

When the barriers start to compress (Fig. 3.4(b)), at a constant compression rate of 70 cm^2/min, the islands get closer and coalesce; as consequence, the pressure increases until the water surface is almost completely covered; at this stage, further compression induces a collapse of the film, as indicated by the bump in the isotherm at $S \approx$ 102 Å^2/molecule (Fig. 3.4(c)). Subsequently, the isotherm shows a plateau, where the area per molecule decreases but the pressure remains approximately constant; this behaviour is typically due to the reorganization of the molecules into a new configuration (Fig. 3.4(d-e)). In our case, this reasonably corresponds to the formation of a double layer. This is particularly evident at the end of the plateau region (Fig. 3.4(e)), where the BAM image show the coexistence of regions of different brightness; as the brightness in BAM images is proportional to the square of the thickness of the Langmuir film [122], this clearly indicates the concurrence of regions of different thickness. At $S \approx$ 40 Å^2/molecule (Fig. 3.4(f)), the area per molecule chosen to make the deposition on the silicon substrate, there is an abrupt increase of the isotherm slope, which indicates a phase transition into a solid-like arrangement of the molecules with almost the same thickness. At higher pressure (Fig. 3.4(g)), the molecules form a tightly packed film that remains compact also after the expansion of the barriers (Fig. 3.4(h)), suggesting a strong interaction among the molecules. On further expansion, the molecules remain relatively well
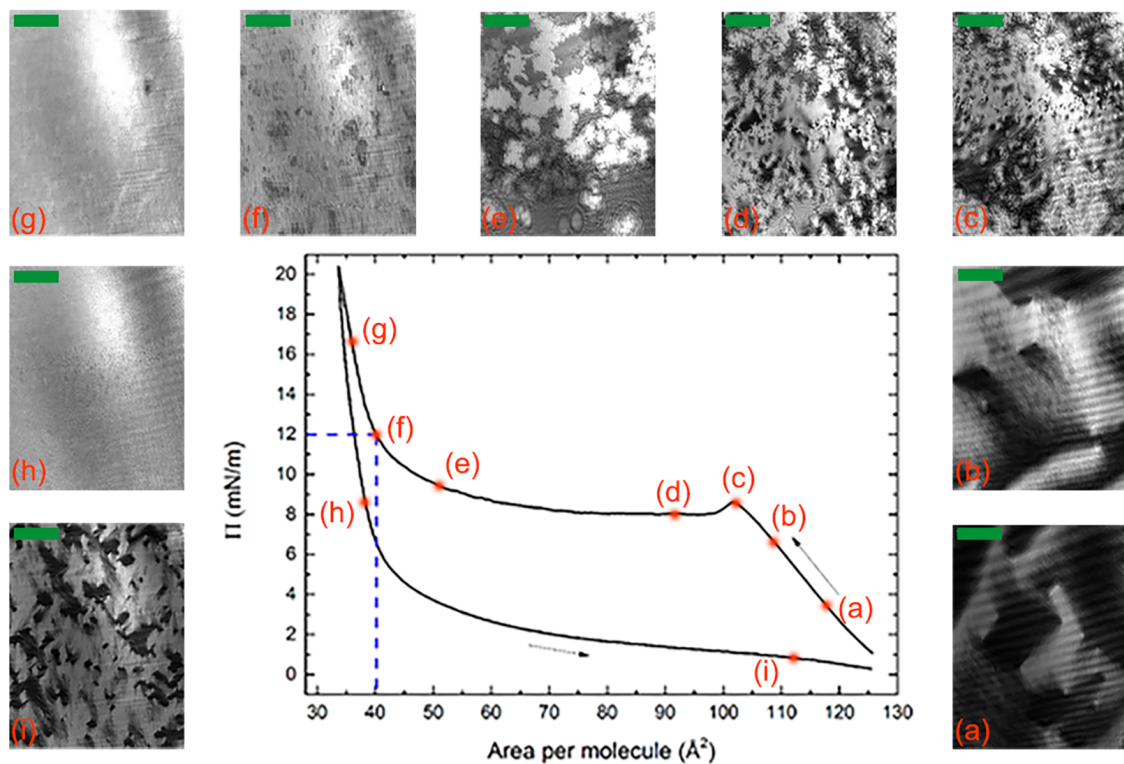
Figure 3.4 Isotherm of a complete compression (leftward arrow) and expansion (rightward arrow) cycle and corresponding sequence of BAM images. The compression/expansion rate was 70 cm^2/min. The dashed lines point out the deposition parameters. The green bar in each BAM image corresponds to 100 μm.

packed even for high value of area per molecule (Fig. 3.4(i)).

The hysteresis observed during the compression/expansion cycle - a quite common occurrence - reflects differences in the aggregation (organization of the molecules at the compression) and relaxation (disorganization of the molecules at the expansion) processes, *e.g.*, their different kinetics. The area between the curves provides the interaction energy among the molecules: it corresponds to a value of 738 cal/mol, which is relatively large if compared to values reported in the literature for other systems (*e.g.* 300 cal/mol for mixed monolayers of fatty acids [123] or 626 cal/mol for a myelin monolayer [124]). This confirms the strong cohesive intermolecular energy.
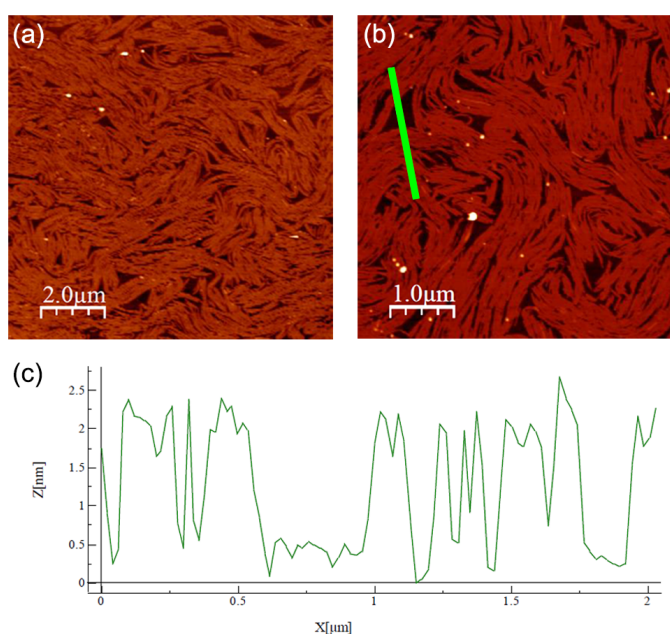
Figure 3.5 (a,b) AFM images of LB films deposited on silicon at Π = 12 mN/m, taken at different positions and magnifications. (c) Thickness profile measured along the green bar in (b).

Single deposition films were deposited at the values of pressure and area per molecule indicated in Fig. 3.4 (12 mN/m and 40 Å^2/molecule, respectively). After evaporation of excess water, the films were analyzed by AFM. Representative images taken at different magnifications are shown in Fig. 3.5(a,b). The film covers almost all the substrate with an average thickness of $\sim$ 22 Å. However, the film is not uniform, showing a supramolecolar fibrous structure. In fact, each fiber has a width of the order of 10^2 nm and and a length of the order of 1 μm. The fibers tend to lie parallel to each other, forming well aligned domains whose size is of the order of few μm^2; however, the fiber alignment is lost over larger distances and no preferential orientation is identifiable on the sample surface. Such

behaviour is very similar to that of the N director **n** in a conventional LC sample with tangential alignment (*i.e.*, with the director lying in the plane of the substrate without any in-plane preferential orientation). XRR measurements discussed below indicate that the deposited films consist of two molecular layers, with the molecules of the underlying layer lying parallel to the substrate. Hence, it is reasonable that the fibrous structure evidenced by AFM reflects the local alignment induced in the film by those molecules.
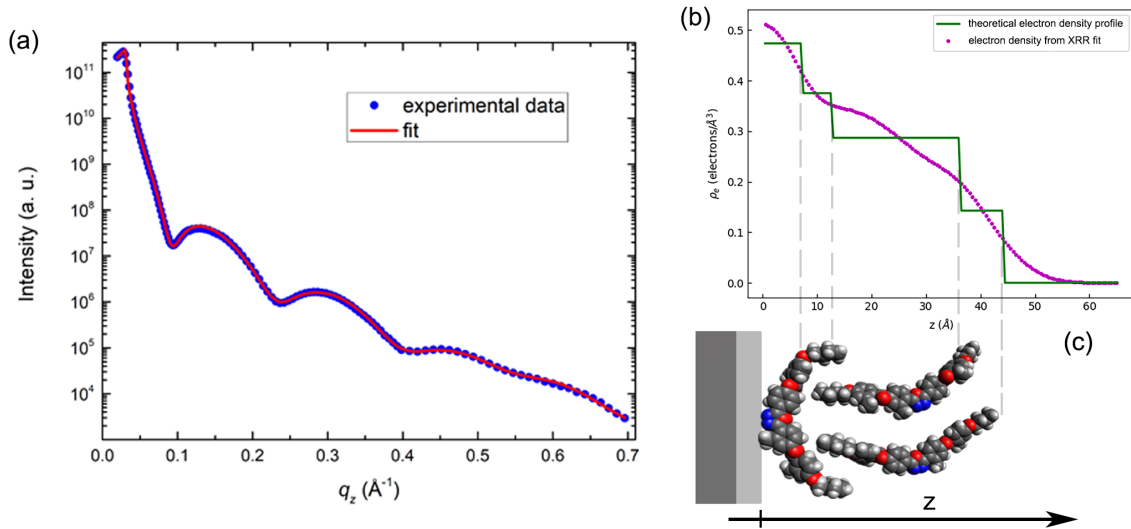
Figure 3.6 (a) XRR curve: experimental data (blue points) and fit curve (red line). (b) Experimental electron density (ρ_e) as a function of the film thickness (z) as obtained from fitting the XRR curve (magenta points) compared with the theoretical electron density profile obtained by the molecular model that best reproduces the experimental data (green line). (c) Molecular organization of the BCM film over the silicon and silicon oxide layers (grey and light grey, respectively). Grey dashed lines indicate the four sections used to model the film.

Films were then characterized by XRR. Fig. 3.6(a) shows the typical reflectivity curve for a single deposition film and the corresponding fit, which reproduces very well the experimental data. That fitting procedure was carried out using the software GenX [125], which uses the Parratt algorithm to simulate the experimental data [126] and models the roughness of each layer through a Gaussian distribution as in the Nevot-Croce theory [127, 128]. For very low incidence angles, *i.e.* in the region of total external reflection when $q_z < q_c$ (q_c is the critical q-value), the footprint of the incoming beam may exceed the sample size and GenX is able to correct the reflected intensity considering the values of beam width, sample length and incidence angle. The fitting is based on a multilayer model of the investigate sample, including both the substrate and the BCM film. The parameters (electron density, thickness and roughness) for all the layers used in the model are summarized in Table 3.1. For the substrate, it is important to take into account the few nanometers thick layer of

native silicon oxide (SiO_2), in most cases amorphous [129], which is typically present on single-crystal silicon substrates. The silicon substrate parameters were kept fixed at values known from the literature, whereas only the electron density was kept fixed for the overlaid SiO_2 layer. Finally, the BCM film was modelled by four LC layers (numbered 1, 2, 3, and 4 from the bottom to the top), so as to reproduce the electron density profile of the film. Electron density, thickness and roughness were fitted for all these layers. At this stage, no particular physical meaning can be attributed to these layers and they were introduced only to model the actual electron density profile of the BCM film. In particular, their number was chosen empirically as the minimum number of layers providing a good fitting of the experimental data. Further increasing the number of LC layers did not provide a significant improvement of the fit. The values are reported in Tab. 3.1.

Table 3.1 Thickness, roughness and electron density for each layer of the XRR fitting model. The bold values were kept fixed during the fitting procedure. The value of roughness indicates the standard deviation of roughness at the upper interface of each layer.

	Thickness (Å)	Roughness (Å)	Electron density (electrons/Å^3)
Si	∞	**1.5**	**0.70**
SiO_2	13.3	1.5	**0.66**
LC layer 1	6.2	3.4	0.52
LC layer 2	19.1	6.0	0.35
LC layer 3	13.8	3.6	0.22
LC layer 4	5.1	5.7	0.16

Fig. 3.6(b) shows the electron density profile obtained from the fit. The electron density decreases with increasing the distance from the substrate, while the total thickness of the four LC layers is 44.2 Å. As this value is larger than the estimated molecular length, it must be inferred that the film must consist of at least two molecular layers. Considering the hydrophobicity of the BCM tails (incompatible with hydrophilic SiO_2) and the larger electron density of the film in proximity of the substrate, it can by hypothesized a film structure as that shown in Fig. 3.6(c), with a compact (solid-like) bottom layer of molecules lying flat over the substrate and a looser upper layer of upright (or slightly tilted) molecules. To confirm this picture, we modeled the described molecular configuration as a sequence of four sections (not necessarily coincident with the four layers used to fit the experimental XRR curve), containing, respectively: the flat cores of the underlying molecules, both tails of the underlying molecules and the lower tails of the overlying molecules, the upright cores of the overlying molecules, and the upper tails of the overlying molecule, as shown in Fig.

3.6(b,c). This model was used to calculate a piecewise theoretical electron density profile, to be compared with the experimental one obtained by fitting the XRR data. The theoretical electron density ρ_i for the $i-th$ section (starting from $i=1$ for the section in contact with the substrate) is described by the function:

$$\rho_i = \frac{K_i}{Ad_i} \, , \tag{3.1}$$

where K_i is the number of electrons in a volume $V_i = Ad_i$ of the $i-th$ section, expressed as the product of the section thickness d_i and the base area A, with A taken equal to the surface area occupied by an underlying molecule. Knowing the molecular structure, K_i can be expressed in terms of the number n of overlying molecules for each underlying molecule, as follows: for section 1, $K_1 = Z_C$ ($Z_C = 262$ is the number of electrons in the mesogen core); section 2 contains 2 tails from the underlying molecule and n tails from the overlying molecules, so $K_2 = Z_T(n+2)$ ($Z_T = 41$ is the number of electrons in one mesogen tail); for section 3, $K_3 = nZ_C$; for section 4, $K_4 = nZ_T$. The theoretical electron density profile is thus defined piecewise as:

$$\rho = \begin{cases} \rho_1 & 0 \leq z < d_1 \\ \rho_2 & d_1 \leq z < d_2 \\ \rho_3 & d_2 \leq z < d_3 \\ \rho_4 & d_3 \leq z \leq d_4 \\ 0 & otherwise \end{cases}$$

In order to validate the model, instead of assuming reasonable values for the parameters in the previous function, $d_{1,2,3}$, A, n were considered variable parameters to be determined by fitting the experimental electron density profile with the piecewise function defined above. The thickness d_4 of the fourth section was dependent on $d_{1,2,3}$, as we imposed a total film thickness of 44 Å (as indicated by the experimental data). The thicknesses and densities calculated by this procedure are reported in Tab. 3.2 for each section; the corresponding theoretical electron density profile is shown in Fig. 3.6(b), superimposed to the experimental profile obtained by XRR. In addition, the fit provided $A = 78.8$ Å^2 and $n = 2.06$.

Despite representing a drastic simplification of the real molecular organization, this four-section model results in a theoretical electron density profile in a good qualitative agreement with the experimental curve (an even better agreement could be obtained by adding some kind of smearing to the theoretical profile, to reflect the continuous change of electron density across the film caused by molecular disorder, flexibility, etc.) More importantly, the thickness values reported in Tab. 3.2 are consistent with the molecular dimensions. For example, the combined thickness of sections 2, 3 and 4 ($\sim$37 Å) is close to the expected length of an

Table 3.2 Best values of thickness and electron density for each section of the film model.

	Thickness (Å)	Electron density (electrons/Å)
LC section 1	7.0	0.47
LC section 2	5.6	0.38
LC section 3	23.8	0.29
LC section 4	7.6	0.14

upright molecule ($\sim$34 Å). Likewise, the value obtained for the base area A of a flat molecule is quite reasonable considering a compact packing with the end tails lifted up. By contrast, the value of $n \approx 2$ upright molecules for each underlying flat molecule suggests an overlying layer which is much less dense. It is expected that further increasing the deposition pressure would result in a more compact upper layer. Overall, these considerations strongly support the adopted model, providing robust evidence of a double layer organization within the film. The discrepancy between the film thickness obtained by XRR and the value provided by AFM can be rationalized by assuming the complete coverage of the substrate by the underlying layer of flat molecules, so that the morphology shown by the AFM scans only reflects the more inhomogeneous and less compact overlying layer (the upper two sections in Fig. 3.6(c)).

3.4 Multiple depositions films

XRR provides information on the film structure in the direction orthogonal to the substrate, but it is blind to in-plane order. The latter can be conveniently investigated by means of GIWAXS. Unfortunately, because of their molecular structure (typically lacking heavy atoms) and short-range positional order, N LCs typically exhibit weak and diffuse diffraction features. As a result, single deposition films were too thin to generate a detectable diffraction signal, and GIWAXS could only be used to study multiple deposition films.

Based on the results obtained with single deposition films, a larger deposition pressure was chosen for multiple depositions, in an attempt to get a more uniform coverage of the substrate and, above all, a more ordered packing of the molecules. To verify the maximum pressure that the film could sustain, a BCM Langmuir film was compressed up to reaching the collapse of the structure. A sudden drop in the corresponding isotherm, shown in Fig. 3.7, indicates a collapse pressure of $\sim$39 mN/m. Hence, a deposition pressure of 30 mN/m was chosen

for the preparation of multiple deposition samples, corresponding to an area per molecule of ~ 32 Å^2.
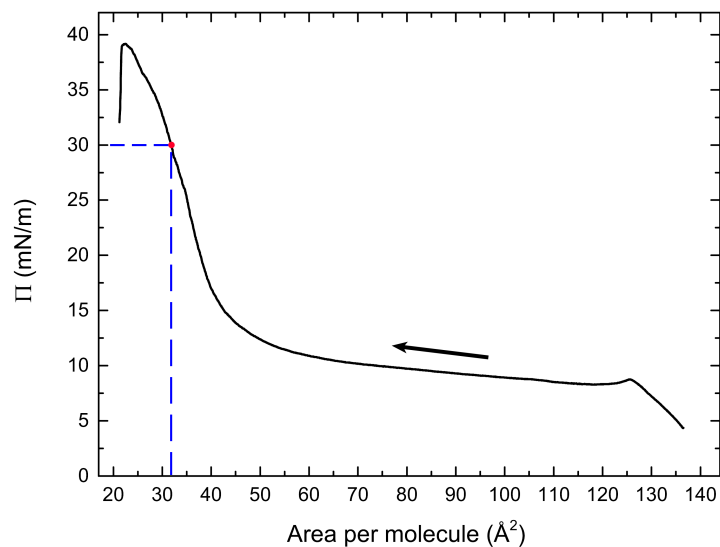
Figure 3.7 Compression isotherm (compression rate 30 cm^2/min) of a BCM Langmuir film from low pressure to the collapse at $\Pi \approx 39$ mN/m. The arrow indicates the compression direction. The dashed lines point out the deposition parameters.

To investigate the effect of the large deposition pressure on the film morphology, a single LB deposition on silicon was observed by AFM (Fig. 3.8). The difference with AFM images of films deposited at $\Pi = 12$ mN/m (Fig. 3.5) is evident. The film is now much more uniform; the fibrous meandering structure present in low pressure samples is replaced here by dense sequence of parallel grooves, homogenously aligned along the direction perpendicular to the dipping direction. The grooves have a width of ≈ 100 nm and a thickness of ~ 33 Å, values quite similar to those observed for low pressure samples. Clearly, the higher deposition pressure results in a more ordered mesoscale structure, characterized by an in-plane anisotropy extending uniformly over the whole sample surface.

LB films deposited on silicon at $\Pi = 30$ mN/m were used as substrates for the subsequent LS depositions (always at pressure of $\Pi = 30$ mN/m) of 28 additional layers. The subsequent LS depositions were carried out with the substrate oriented in such a way that the film compression direction was parallel to the LB dipping direction of the first layer (Fig. 3.3. The multiple deposition films prepared in this way were hence characterised by GIWAXS. Typical diffraction patterns measured with the incident beam parallel to the dipping/compression direction ($\varphi = 0$, with φ indicating the azimuthal angle between the dipping/compression direction of the sample and the incidence plane of the beam) and perpendicular to the dipping/compression direction ($\varphi=\pi/2$) are shown in Fig. 3.9(a) and (b), respectively. The
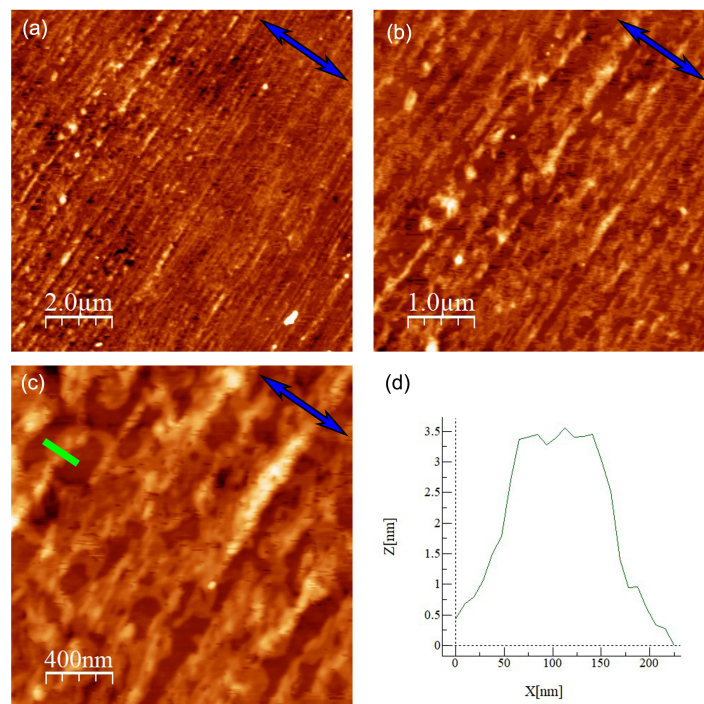
Figure 3.8 (a-c) AFM images of a LB film deposited on silicon at $\Pi = 30$ mN/m , taken at different positions and magnifications. The blue arrows indicate the dipping direction of the substrate. (d) Thickness profile measured along the green bar in (c).

evident difference between the two diffraction patterns is a clear indication of the sample in-plane anisotropy, already evidenced by the AFM scans. However, while the anisotropy observed by AFM is relative to the mesoscale sample morphology, the GIWAXS data pertain to a much lower length scale, revealing the anisotropy of the molecular ordering.
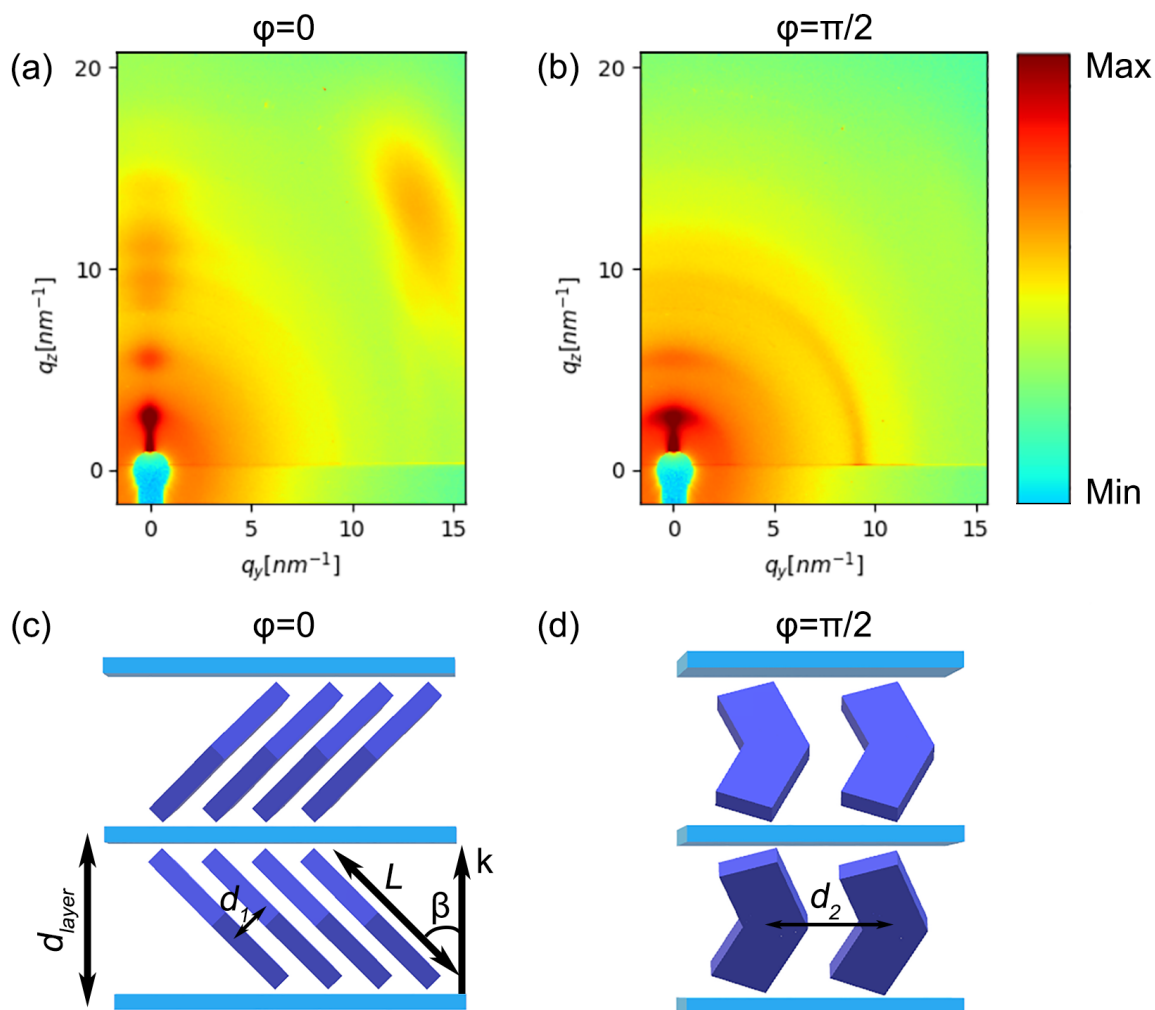
Figure 3.9 On the upper panel, GIWAXS patterns of a multiple deposition film with the incident beam (a) parallel ($\varphi = 0$) and (b) perpendicular ($\varphi = \pi/2$) to the dipping/compression direction. Only the right half of the patterns is shown because of the pattern symmetry. The diffraction intensity is colour-coded on a logarithmic scale. On the lower panel, scheme of the layered molecular arrangement as seen for (c) $\varphi = 0$ and (d) $\varphi = \pi/2$.

Looking into the details of the GIWAXS patterns, it is possible to note the following features. A sequence of reflections centred at $q_y = 0$ is evident along q_z in both patterns. They consist of a fundamental reflection at $q_z = 2.5$ nm^{-1} and the corresponding higher orders.

These reflections are clearly related to the multilayer nature of the sample and correspond to an interlayer distance $d_{layer} = 25.0$ Å. This value is significantly lower than the molecular length ($L = 34$ Å). Assuming no intercalation, it suggests a tilt of the molecules, with the molecular long axis forming an angle $\beta = \arccos(d_{layer}/L) = 43°$ with the layer normal (Fig. 3.9(c)). Comparing this sequence of reflections in the two patterns, it can also be noticed that they are much more intense and transversally narrow in the pattern taken at $\varphi = 0$ (Fig. 3.9(a)). By contrast, a significant "circular" broadening affects the reflections in the patterns taken at $\varphi = \pi/2$ (Fig. 3.9(b)), which also smears out the diffraction intensity. This effect is attributed to undulations of the layers in the plane normal to the dipping direction, *i.e.* to the grooves evidenced by AFM.

Fig. 3.9(a) also shows a broad oblique reflection in the wide-angle region, centred at ($q_y = 12.5$ nm^{-1}, $q_z = 12.1$ nm^{-1}). The same feature is absent in the pattern taken at $\varphi = \pi/2$. The **q** vector of this reflection forms an angle of $\sim 44°$ with the layer normal and corresponds to an intermolecular distance $d_1 \approx 3.6$ Å. The latter value corresponds to the transverse intermolecular distance between well packed molecules (measured in a direction perpendicular to the plane defined by the flat molecular core), while the angular tilt of the scattering vector confirms the molecular tilt initially suggested by the value of d_{layer} and the lack of intercalation in the multilayer (Fig. 3.9(c)). Finally, the disappearance of this oblique reflection for $\varphi = \pi/2$ indicates that the molecules tilt in the plane orthogonal to the dipping/compression direction.

Rotating the sample to $\varphi = \pi/2$, the wide-angle diffraction feature disappears, substituted by a much narrower in-plane peak centred at ($q_y = 9.1$ nm^{-1}, $q_z = 0$ nm^{-1}). It corresponds to the distance $d_2 \approx 6.9$ Å, interpreted as the transverse intermolecular distance measured in the plane of the cores (Fig. 3.9(d)). Once again, the "circular" broadening of this reflection is attributed to the layer undulation in the plane orthogonal to the dipping/compression direction.

3.5   Conclusions

The work described above demonstrated the possibility to prepare high quality BCM films by single and multiple LB/LS depositions. This result is not obvious as the BCM molecular structure is definitely different from the typical amphiphilic structure of molecules commonly used to make Langmuir films. The combination of isotherm analysis, BAM, AFM and XRR studies revealed that this result is made possible by the formation of a double layer structure, with the upper layer of upright molecules separated from the substrate by an underlying layer of flat molecules.

The study also evidenced the critical role of the deposition pressure in determining the film structure, both at the molecular (microscale) and morphological (mesoscale) level. In particular, a sufficiently large deposition pressure results in homogenous films with a strong in-plane anisotropy, an original result never reported before in the literature that will serve as the starting point for further investigations on the biaxiality in such films. In fact, GIWAXS measurements unequivocally show that the molecular packing in multiple deposition films is biaxial, with the biaxial order extending homogeneously over the whole sample surface. These films could thus be proposed as unconventional substrates to control the director(s) alignment of bent-core nematics and, more in general, of other possibly biaxial LC systems.

Chapter 4

Liquid crystal thermosets: a new class of high-performance polymers

4.1 Introduction

The terms "high-temperature" (HT) or "high-performance" (HP) polymers have generally been reserved for polymers which display exceptional thermal stability over prolonged periods of time in combination with mechanical performance and solvent resistance. The development of HT/HP polymers began in the late 1950s, mainly in support of the growing interest in electronics and aerospace industry [130–135]. The most prolific decade for HT/HP polymers was 1960 to 1970 where the most thermally stable heterocyclic rings were incorporated within polymers. Examples of specimens fabricated in this decade include polymides $Kapton^{TM}$, $Vespel^{TM}$, $Pyre - ML^{TM}$ by DuPont and $Skybond^{TM}$ by Monsanto. The markets for $Pyre - ML^{TM}$ and $Skybond^{TM}$ are considerbly smaller than those for $Kapton^{TM}$ and $Vespel^{TM}$, with the first one which has become the largest selling HT/HP polymer product in the world.

The 1970s saw the commercialization of several HT/HP polymers. Two of the more important contributions during this period were $Kevlar^{TM}$ by DuPont, a high modulus aromatic polyamide fiber, and $Ultem^{TM}$ by General Electric, a thermoplastic polyetherimide. As a moldable polymer, $Ultem^{TM}$ offered a favourable combination of relatively low cost, excellent processability, and moderate mechanical properties; a combination that eluded chemists for many years. In the 1980s, the work focused on exploring ways to make polymers more processable and on developing more cost-effective routes to convert them into various form such as adhesives, composite matrices, dielectric films, foams and moldings. Industrial research efforts focused on processing rod-like polymers from LC polymer melts. The

motivation was to develop HP polymers retaining the high degree of polymer chain alignment inherent to thermotropic LC polymers. In fact, the sufficiently rectilinear (high persistence length) LC polymer chains adopts the N morphology which is carried over to the solid state and results in an extremely low coefficient of thermal expansion, negligible moisture uptake and ultra-high strength [136]. However, thermotropic LC polymers continue to have processing challenges that have attenuated the widespread adoption of LC polymers [137]. In order to prevent this inconvenient, low molecular weight macromonomers having compositions similar to commercial LC polymers are used to make LC thermosets (LCTs). In this class of polymers, a part, or most of the positional and long-range order of the molecules in the melt can be preserved after cross-linking [138, 139]. Especially the N phase is attractive from a processing point of view. Several groups have investigated a variety of low molecular mass thermotropic monomers, end-capped with different reactive. Unfortunately, some drawbacks still remain, *e.g.* high glass-transition temperatures [140] and low viscous N melts upon heating [141, 142]. In a series of reports pionereed by researchers at NASA, LC end-functionalized "macro-monomer" precursors (Fig. 4.1) were shown to lead to a new class of HT/HP LCTs [143].
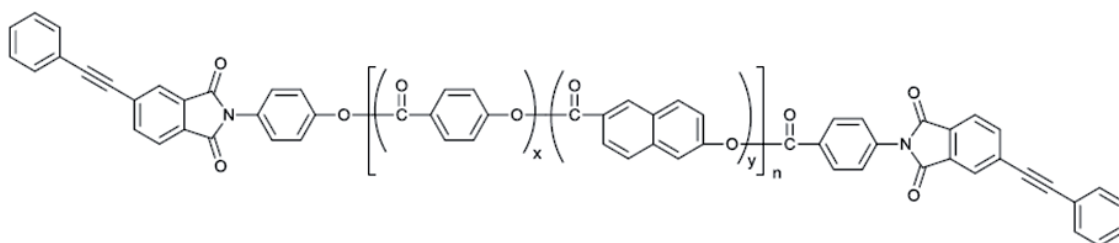
Figure 4.1 LC reactive oligomer with PE end-groups.

They can get a very high glass transition temperature (up to 450°C) and decomposition temperatures (>500°C), and exhibit extremely strong bonding to glass, metal, and carbon fibers, a prerequisite for a strong fiber-matrix interface in composites. In the melt phase of the reactive oligomer precursor (around 300°C) before curing, the fluid is a low viscosity N LC that can be readily processed. In the melt, the uniaxial N phase generates spectacular properties along the N director **n**, properties that can be transferred to the polymer by a thermally driven cross-linking reaction. This new family of reactive all-aromatic LC oligomers can be processed just like a traditional thermoplastic.

Critical to the continued development of this new class of LC thermosets is a comprehensive understanding of the end-group reaction kinetics. In an effort to gain insights into the PE end-group reactivity of the LC thermoset macromonomer precursors, two model mesogens with well-defined molecular structures (Fig. 4.2) have been prepared: PE terminated biphenol (PE-

biphenol-PE) and naphthalenediol (PE-naphthalenediol-PE) [144]. The rod-like mesogens exhibit a fluid N_u phase which can be readily oriented by an external magnetic field **B**, enabling to conduct nuclear magnetic resonance (NMR) and XRD measurements on aligned samples. In this chapter, the high temperature XRD and ^{13}C NMR experiments in the N phases of PE-biphenol-PE and PE-naphthalenediol-PE are reported, in an effort to monitor the transformation of PE end-goups (specifically, the ethynyl group) and to follow the evolution of the N phase during the chain extension/cross-linking reactions.

4.2 Phenylethynyl terminated LC thermosets

The synthesis of PE-biphenol-PE and PE-naphtalenediol-PE (Fig. 4.2) have been described in [144]. PE is the only reactive functionality, so far, which survives the extreme melt condensation conditions ($T_{max} \approx 310$ °C) and does not cross-link or chain extend prematurely. In addition, PE has been used extensively as a reactive end-group functionality in cross-linkable poly(etherimide)s [145, 146] and the mechanical properties of the final cured products were found to be outstanding. Another reason for using PE is the fact that this material not only form cross-link functionalities but can also chain extend, depending on the concentration and temperature profile used. As investigated by Roberts *et al*. [147], PE chain extends and forms cross-linking functionalities. In either case, the functionalities formed do not deviate too much from linearity and hence do not disrupt LC formation. The biphenol and naphtalenediol core make the LC thermosets here studied a low molecular weight mesogen with a well-defined rod-like structure.

PE–biphenol–PE

PE–naphthalenediol–PE
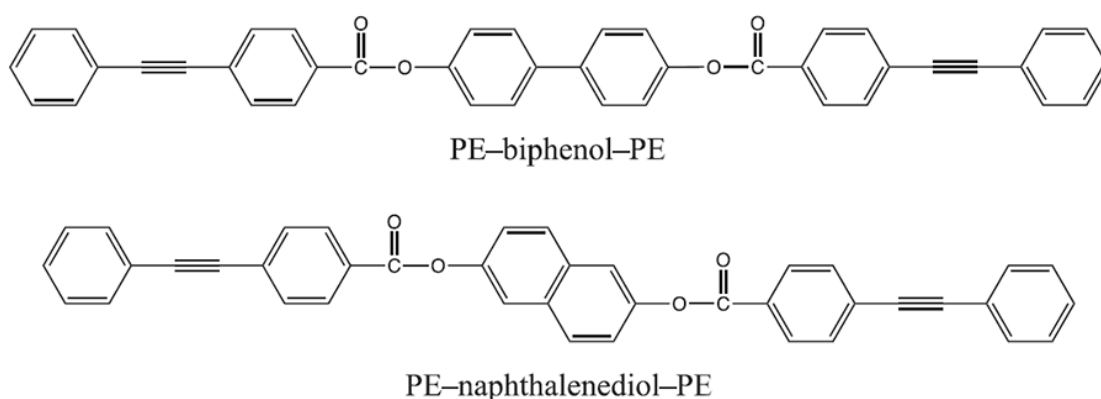
Figure 4.2 Molecular structures of model mesogenic compounds. Reprinted from [144].

The differential scanning calorimetry (DSC) measurements for PE-biphenol-PE and PE-naphtalenediol-PE points out a well defined K-N transition temperatures (Fig. 4.3). For

both model compounds the N range persists into the chain extension/cross-linking reactions temperature range 325-400 °C (see exotherm); PE-naphtalenediol-PE exhibits a solid state recrystallization transition at 233 °C prior to the K-N transition at 243 °C. If the temperature is restricted to < 300 °C both mesogens exhibit reversible K-N transitions, *e.g.* see DSC of PE-biphenol-PE in Fig. 4.3.
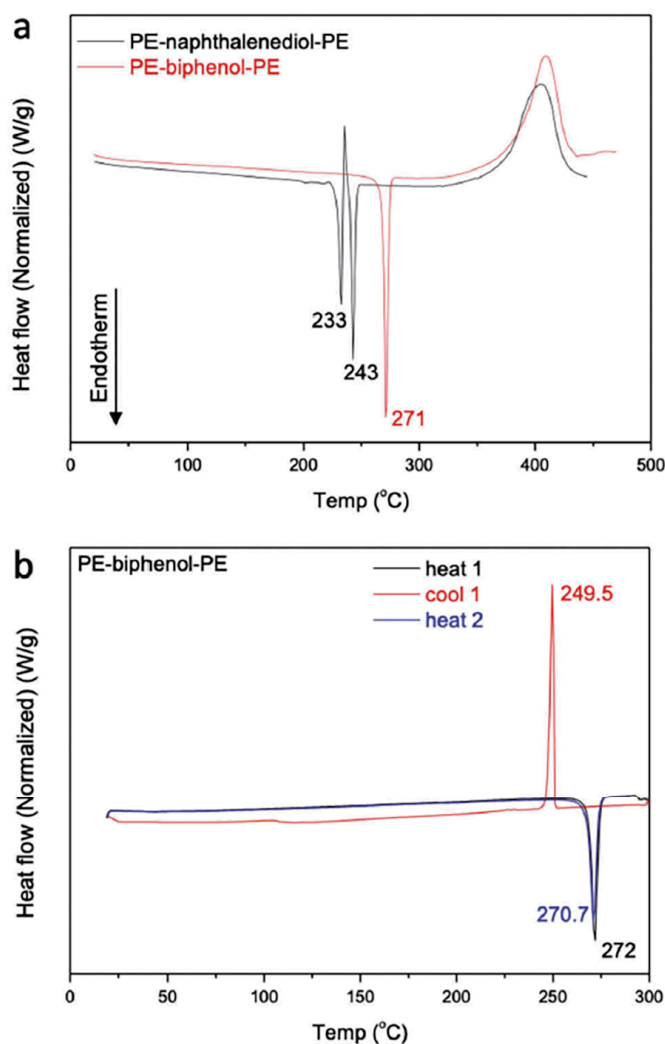
Figure 4.3 DSC scans of PE-biphenol-PE and PE-naphthalene-PE (heating/cooling rate 20 °C/min): (a) both mesogens show K-N transitions followed by reaction exotherms on continued heating; (b) the K-N transition of the PE-biphenol-PE is reversible if the sample does not undergo any end-group reactions. Reprinted from [144].

4.3 X-ray diffraction

XRD measurements were performed at the BM26B DUBBLE beamline of the ESRF, Grenoble (France). Samples were placed in capillaries and mounted in a temperature-controlled hot-stage; a superconducting magnet [148] allowed application of a vertical magnetic field **B** (B = 3.1 T) parallel to the capillary. Beam wavelength λ and sample-to-detector distance D were set to λ = 0.772 Å and D = 0.201 m for PE-biphenol-PE and to λ = 0.816 Å and D = 0.178 m for PE-naphtalenediol-PE. Fig. 4.4(a) and 4.5(a) show typical XRD patterns measured in the N phase of PE-biphenol-PE and PE-naphtalenediol-PE, respectively.
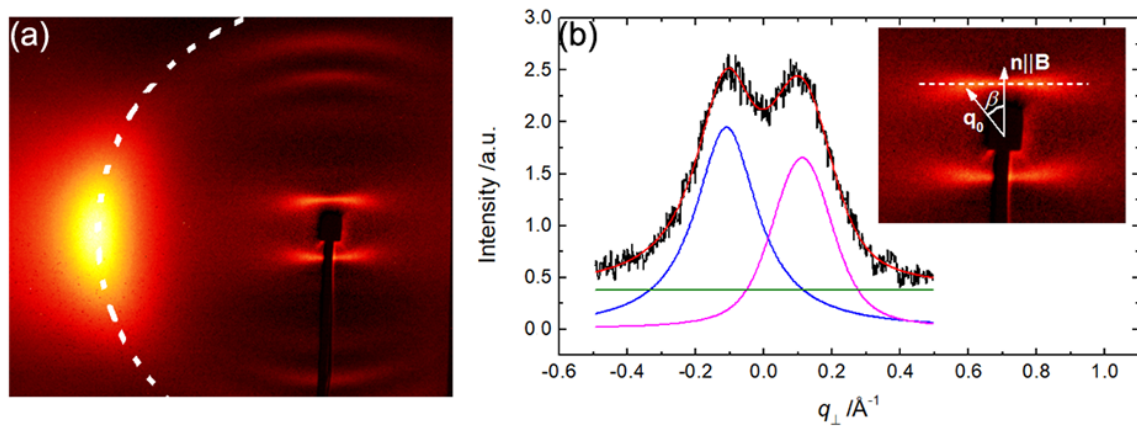
Figure 4.4 (a) XRD pattern of the N phase of PE-biphenol-PE, aligned by a vertical magnetic field **B**, at T = 285 °C and azimuthal cut of the wide-angle reflection (dashed line). (b) Closeup of the small-angle XRD pattern (inset) and fitting (red curve) of its intensity profile (black curve) along a transverse cut ($\perp$ **B**, dotted line in the inset) by the sum of two Voigt lineshapes and a constant background (blue, purple and green curves, respectively). Reprinted from [144].

The patterns were recorded at T = 285 °C for PE-biphenol-PE and T = 263 °C for PE-naphtalenediol-PE *i.e.* below the onset of chain extension/cross-linking reactions (cooling back the samples after several minutes spent at these temperatures restores the K phase). The patterns consist of three main features: *i*) a pair of small-angle diffuse reflections aligned along the meridional direction ($\parallel$ **n**), related to the intermolecular longitudinal order; *ii*) additional meridional reflections in the intermediate/wide-angle region, mainly resulting from intramolecular longitudinal scattering; *iii*) a pair of very broad equatorial ($\perp$ **n**) reflections associated with transverse intermolecular order. In particular, the small-angle meridional reflections exhibit a characteristic dumbbell shape, due to splitting of the diffracted intensity in the direction orthogonal to **n**. This feature, evident in the intensity profiles shown in Fig. 4.4(b) and 4.5(b), is indicative of tilted cybotactic order. As explained elsewhere [47, 48],
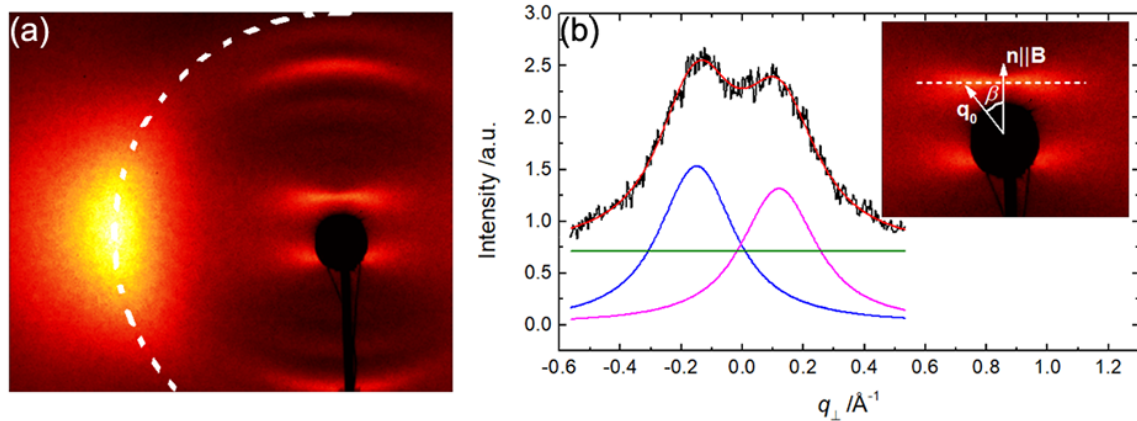
Figure 4.5 (a) XRD pattern of the N phase of PE-naphtalenediol-PE, aligned by a vertical magnetic field **B**, at T = 263 °C and azimuthal cut of the wide-angle reflection (dashed line). (b) Closeup of the small-angle XRD pattern (inset) and fitting (red curve) of its intensity profile (black curve) along a transverse cut ($\perp$**B**, dotted line in the inset) by the sum of two Voigt lineshapes and a constant background (blue, purple and green curves, respectively). Reprinted from [144].

the wavevector $\mathbf{q_0}$ associated with each diffraction maximum (insets of Fig. 4.4(b) and 4.5(b)) provides the layer spacing $d = \frac{2\pi}{q_0}$, while the angle β between $\mathbf{q_0}$ and **n** corresponds to the tilt of the normal to the *Sm* layers with respect to the molecular director **n**; finally, the molecular length L can be estimated as $L = \frac{d}{\cos\beta}$. This model provides the values $d = 31.3$ Å, $\beta = 33.8°$ and $L = 37.7$ Å for PE-biphenol-PE at = 285 °C and $d = 27.7$ Å, $\beta = 35.8°$ and $L = 34.2$ Å for PE-naphtalenediol-PE at T = 263 °C, in good agreement with the molecular lengths estimated by molecular modelling $L = 36.5$ Å and $L = 34.3$ Å for PE-biphenol-PE and PE-naphtalenediol-PE, respectively. The diffraction spots' FWHM $\Delta q_{\perp,\parallel}$, measured along the directions orthogonal and parallel to **n**, provides the correlation lengths of cybotactic order $\xi_{\perp,\parallel} = \frac{2}{\Delta q_{\perp,\parallel}}$ in the corresponding directions [47]. In this way, for both compounds we obtain $\xi_{\parallel}$ of the order of one molecular length and $\xi_{\perp}$ of the order of about two transverse intermolecular distances. These small values, slightly larger for PE-biphenol-PE compared to PE-naphtalenediol-PE, evidence the very short-range nature of cybotactic order. The additional meridional reflections spanning the intermediate to wide-angle region are diffraction features often encountered in the N phase of relatively rigid calamitic mesogens [149, 150]. They arise from the tendency of molecules to form weakly ordered strings, while the relative intensity of the diffraction orders reflects the electron density profile of the specific mesogen.

Finally, the *d*-spacing associated to the broad wide-angle equatorial reflections, ~ 4.7 Å for both compounds, provides an estimate of the transverse intermolecular distance. Additionally,

the azimuthal broadening of this diffraction feature, measured along the cuts shown in Fig. 4.4(a) and 4.5(a), provides a convenient way to estimate the molecular orientational distribution function $f(\theta)$ - θ being the angle between the long molecular axis and the molecular director **n** – and hence the orientational order parameter $\langle P_2 \rangle$ (see Section 1.1.4). The approach explained in the Appendix A, provided the values $\langle P_2 \rangle = 0.77$ for PE-biphenol-PE at $T = 285\ °C$ and $\langle P_2 \rangle = 0.71$ for PE-naphtalenediol-PE at $T = 263\ °C$. Even considering their uncertainty ($\sim 5 - 10\%$), these values are relatively large and indicate a quite high N-I transition temperature. In fact, by assuming an ideal Maier-Saupe temperature dependence of $\langle P_2 \rangle$ it is possible to obtain a rough estimation of the expected N-I transition temperature, $\sim 500\ °C$ for PE-biphenol-PE and $\sim 400\ °C$ for PE-naphtalenediol-PE. These temperatures are well above the onset of chain extension/cross-linking reactions and thus experimentally inaccessible.
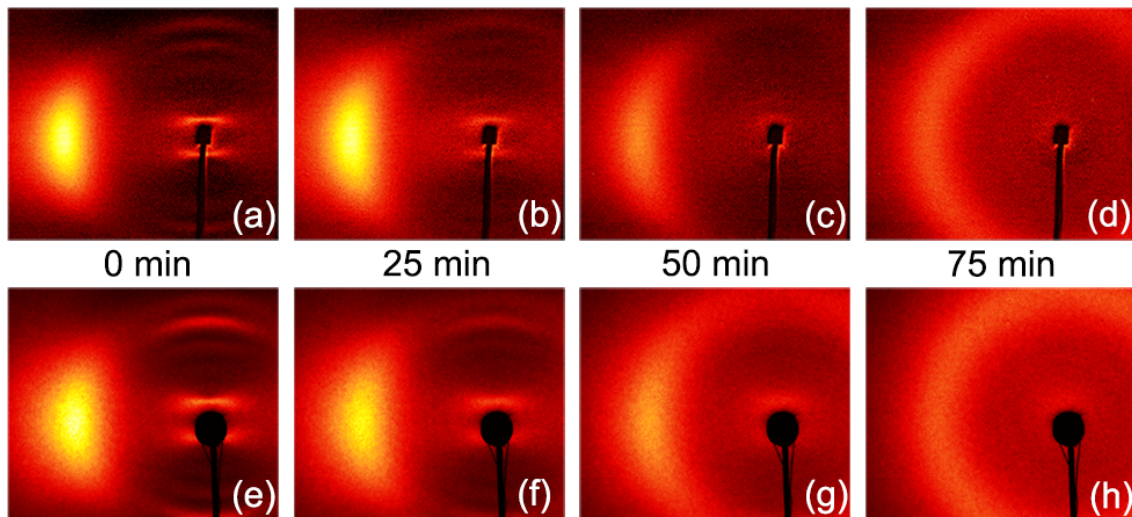
Figure 4.6 Time evolution of XRD patterns in the N phase, probed at 25 min intervals upon cross-linking at constant temperature: (a-d) PE-biphenol-PE at $T = 335\ °C$; (e-h) PE-naphtalenediol-PE at $T = 308\ °C$. Adapted from [144].

In order to study the effect of curing on the structural properties of the LC thermoset N phase, we rapidly heated PE-biphenol-PE to $T = 335\ °C$ and monitored the temporal evolution of the XRD pattern (Fig. 4.6(a-d)). The same procedure was applied to PE-naphtalenediol-PE at $T = 308\ °C$ (Fig. 4.6(e-h)). In both cases we observed a gradual transformation of the diffraction pattern into an I ring, reflecting a cross-linking induced decrease of the N order. After 75 min, the N order appeared almost completely lost. No change of the XRD patterns – in particular, no sign of crystallization – was observed upon cooling the samples to room temperature at the end of the thermal process or by removing the magnetic field. A quantitative comparison
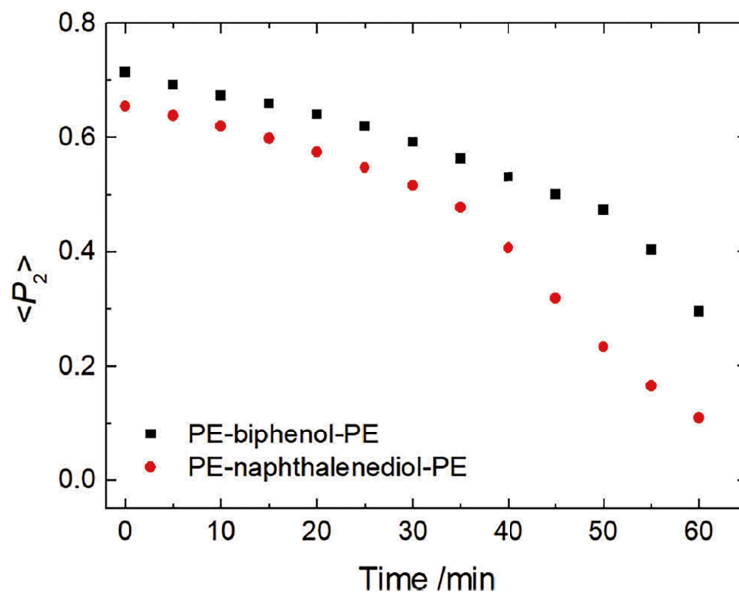
Figure 4.7 Time evolution of the orientational order parameter $\langle P_2 \rangle$ upon cross-linking at constant temperature as obtained by XRD measurements: PE-biphenol-PE at $T = 335$ °C (black squares), PE-naphtalenediol-PE at $T = 308$ °C (red circles). Reprinted from [144].

of the time evolution of $\langle P_2 \rangle$ for the two compounds, as obtained from the analysis of the corresponding XRD patterns, is provided in Fig. 4.7. Their behaviour is similar, with large initial values, $\langle P_2 \rangle = 0.71$ for PE-biphenol-PE and $\langle P_2 \rangle = 0.65$ for PE-naphtalenediol-PE, decreasing to $\langle P_2 \rangle = 0.30$ and $\langle P_2 \rangle = 0.11$ respectively after 2 h of thermal treatment. In both cases, the decrease, approximately linear, was marked by a discontinuity in the derivative when $\langle P_2 \rangle$ reached the value of ~ 0.47.

4.4 Nuclear magnetic resonance

A combination of solid-state NMR and high-temperature (liquid-state) NMR is used to characterize the cure chemistry. Solid-state spectra of powders were carried out with a Bruker360 spectrometer using a magic-angle spinning double resonance probe employing a cross-polarization pulse sequence with ^1H decoupling. The high-temperature (liquid state) studies used a single ^{13}C pulse width of 2.15 μs (3 dB) and ^1H broadband decoupling using an inverse gated ^{13}C NMR experiment where decoupling occurs during the acquisition time. An existing probe was modified to access the high melting and cure temperatures.

The NMR method exploits the incompletely averaged 2nd rank NMR interactions in the oriented N melt; the procedure used in this work avoids the laborious procedure of curing

for a specified length of time at a given temperature and then powdering the sample for solid state NMR experiments such as CP/MAS; also the high-temperature NMR experiment can be carried out without expensive ^{13}C labelling [151]. In order to follow the chemistry during the curing process we examined the kinetics of the disappearance of the reactive $C \equiv C$ group which, because of its chemical shift anisotropy (CSA) in the oriented N phase, is readily resolved from the rest of the resonances of the PE end-capped model compound PE-naphtalenediol-PE. The ^{13}C spectra of PE-naphtalenediol-PE using solid state NMR on the uncured sample along with the high-temperature, 'high resolution' spectrum of the oriented N phase of PE-napthalenediol-PE are superposed in Fig. 4.8 with the ethynyl resonances indicated.
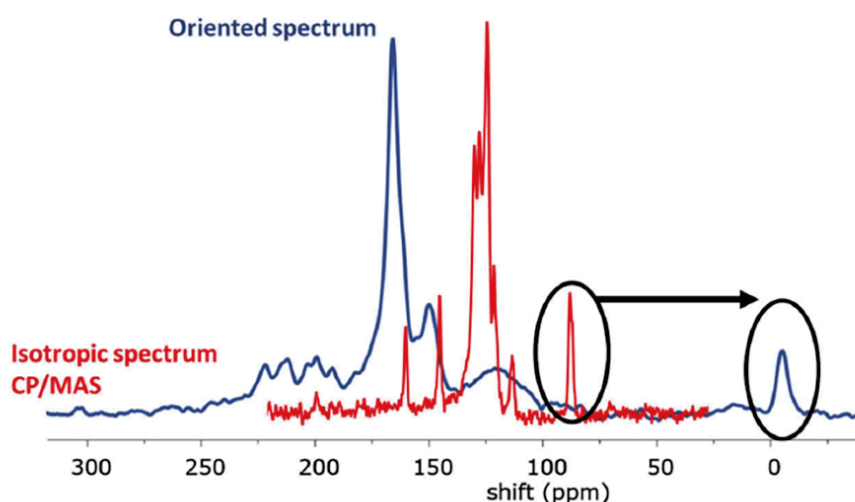
Figure 4.8 ^{13}C CP/MAS spectrum (I powder; red) and the LC spectrum (oriented melt; blue) of PE-naphtalenediol-PE. The chemical shift (arrow) of the ethynyl group due to the orientation of the $C \equiv C$ with its inherently large CSA is indicated. Reprinted from [144].

The CP/MAS spectrum shows the nicely resolved $C \equiv C$ resonance at ~ 90 ppm. That $C \equiv C$ resonance is shifted to $\sim$ - 5 ppm in the N melt, because the director spontaneously aligns along the spectrometer magnetic field exposing the large CSA of the $C \equiv C$ group. The disappearance of that $C \equiv C$ resonance indicates the formation of ill-defined cure products – cyclization reactions enabling chain extension and random cross-linking reactions. By integrating the chemically shifted $C \equiv C$ NMR peak at different time points during cure at elevated temperature in the N melt, it is possible to infer the concentration of remaining ethynyl groups to obtain kinetic plots describing the loss of the $C \equiv C$ bonds.
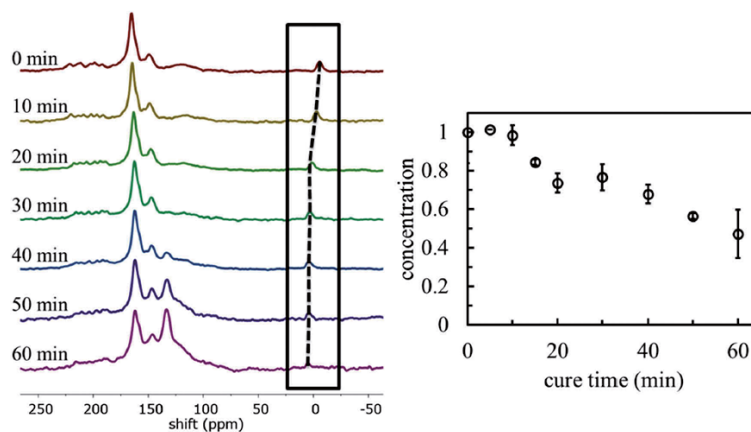
Figure 4.9 ^{13}C NMR of the PE-naphtalenediol-PE at different cure times at 300 °C (left) and plot of concentration of ethynyl peak vs cure time (right). Reprinted from [144].
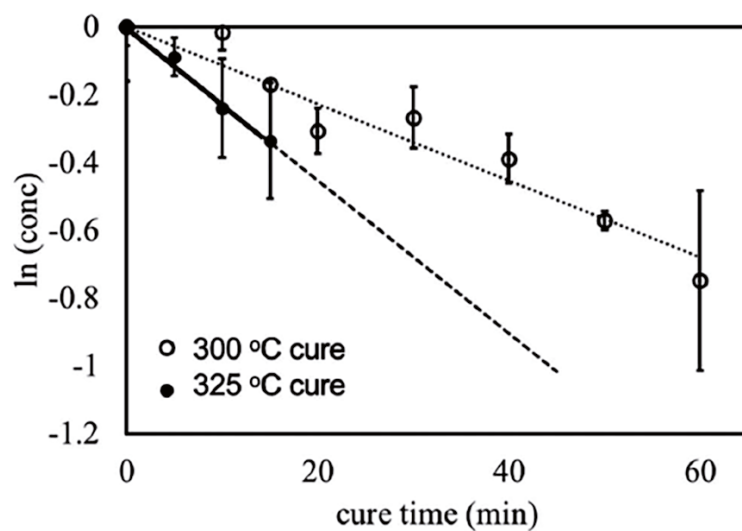
Figure 4.10 Kinetic plot of the natural log of concentration of C≡C vs. cure time for the PE-naphtalenediol-PE; linear fits to the data (dotted lines) yield first-order rate constants. Reprinted from [144].

Fig. 4.9 shows example spectra taken during cure at 300 °C along with the plot of concentration of reactive end-groups against cure time; Fig. 4.10 shows the kinetic plots with the first-order rate constants calculated from fits to the data. The observed curing chemistry of PE-naphtalenediol-PE follows first-order rate kinetics with rate constants of 0.011 min^{-1} and 0.023 min^{-1} at 300 °C and 325 °C, respectively. In addition to kinetic information, NMR also gives information about the supramolecular organization in the LC melt during curing because the $C \equiv C$ CSA can be related to the orientational order of the $C \equiv C$ triple bond which, in turn, gives insights into the orientational order of the 'long molecular axis' of the model LC thermoset mesogen PE-napthalenediol-PE . The chemical shift of the $C \equiv C$ resonance shifts towards its I value (dashed line in Fig. 4.9) during the curing process which indicates a decrease in orientational order as the crosslinked network is formed. Using eqn 4.1,

$$S_{zz} = \frac{\delta^{aniso}}{\sigma_{zz}^{C \equiv C} - \sigma_{yy}^{C \equiv C}} \, , \tag{4.1}$$

the order parameter of PE-napthalenediol-PE $C \equiv C$ bond S_{zz} can be calculated from the observed chemical shifts (δ^{obs} = - 5 ppm before cure and δ^{obs} = +6 ppm after curing for 60 min at 300 °C) using the observed I chemical shift (δ^{iso} = 88 ppm). The $C \equiv C$ CSA values used to calculate the triple bond order parameter are the principal chemical shielding tensor elements for dimethylacetylene, σ_{zz} = - 44 and $\sigma_{xx} = \sigma_{yy}$ = 157, reported by Pines *et al*. [152]:

$$\delta^{obs} = \delta^{iso} + \delta^{aniso} \, ,$$
$$\delta_{C \equiv C}^{iso} = \frac{1}{3}(\sigma_{xx} + \sigma_{yy} + \sigma_{zz}) =$$
$$= \frac{1}{3}(157 + 157 - 44) = 90 ppm \, , \tag{4.2}$$
$$\delta_{C \equiv C}^{aniso} = S_{zz}\left(\sigma_{zz} - \frac{\sigma_{xx} + \sigma_{yy}}{2}\right) =$$
$$\cong 0.5(-44 - 157) = -110 ppm \, ,$$

It was found that the $C \equiv C$ order parameter derived from NMR is fairly constant during the curing process only dropping from S_{zz} = 0.46 to S_{zz} = 0.41 after 60 min at 300 °C. The $C \equiv C$ peak also broadens which indicates a gradient of order parameters – *i.e.* domains with different degrees of order.

4.5   Discussion

XRD measurements indicate for both mesogens high initial order parameters, $\langle P_2 \rangle = 0.71$ for PE-biphenol-PE at 335 °C and $\langle P_2 \rangle = 0.65$ for PE-naphtalenediol-PE at 308 °C, and comparable reaction kinetics, with an evident deterioration of $\langle P_2 \rangle$ upon curing (Fig. 4.7). On the other hand, the initial order parameter of PE-naphtalenediol-PE estimated by NMR data is significantly lower and decreases slightly while reaction proceeds from $S_{zz} = 0.46$ to 0.41 upon curing for 60 min at 300 °C. The difference in the initial values of $\langle P_2 \rangle$ and S_{zz} obtained by the two techniques is due to the phenomena being probed: NMR measures the average orientation of the C≡C triple bond relative to the director $\mathbf{n} \parallel \mathbf{B}$; in contrast, XRD provides the average orientation of the molecular long axis $\mathbf{m}$ relative to $\mathbf{n} \parallel \mathbf{B}$. Unlike PE-biphenol-PE, PE-naphtalenediol-PE - the subject of the NMR study – has conformational isomers wherein the C≡C bond axis is not colinear with $\mathbf{m}$ (Fig. 4.11); isomerization will thus average the CSA relative to the long axis $\mathbf{m}$, lowering the observed NMR value of S_{zz} relative to the XRD value $\langle P_2 \rangle$ which measures the average orientation of $\mathbf{n}$. Besides averaging the orientation of the C≡C triple bond axis relative to $\mathbf{m}$, the isomerization also lowers the effective aspect ratio of PE-naphtalenediol-PE and that also may account for the lower XRD order parameter of PE-naphtalenediol-PE ($\langle P_2 \rangle = 0.65$) relative to PE-biphenol-PE ($\langle P_2 \rangle = 0.71$) at 335 °C. The fact that the NMR order parameter is calculated from the CSA of the remaining C≡C triple bonds may also explain the small decrease of S_{zz} observed in NMR data upon curing. That is, the molecules responsible for the C≡C resonance, whose shift determines S_{zz}, are those unreacted C≡C triple bonds and, moreover, those remaining C≡C units probably reside in N droplets dispersed in the I crosslinked network.

Polarizing optical microscopy (Fig. 4.12) of PE-naphtalenediol-PE shows that the N birefringence is lost on curing. This is not surprising as transition temperatures, in particular, the N-I transition, can be easily suppressed with minor chemical structural modifications in low molar mass LC. The chain extension and cross-linking reactions would lead to major perturbations of the shapes of the model LC thermosets and the onset of an I phase would be anticipated as observed in the microscopy. There may be a distribution of NMR order parameter values corresponding to the observed broadening of the C≡C resonance with time at elevated temperature. However, unless the droplets are very small the value of the S_{zz} will appear to be unchanged. On the other hand, the XRD data are inherently averaged over a macroscopic sample volume and are therefore unable to discriminate a true I phase ($\langle P_2 \rangle = 0$) from variably oriented N phase droplets ($\langle P_2 \rangle \neq 0$ locally but vanishing macroscopically). The possibility of chain extension/cross-linking reactions partitioning the local $\mathbf{n}$ director from a uniform alignment along $\mathbf{B}$ to uncorrelated and unaligned N domains seems unlikely in a magnetic field exceeding 3 T. In conjunction with polarizing optical microscopy
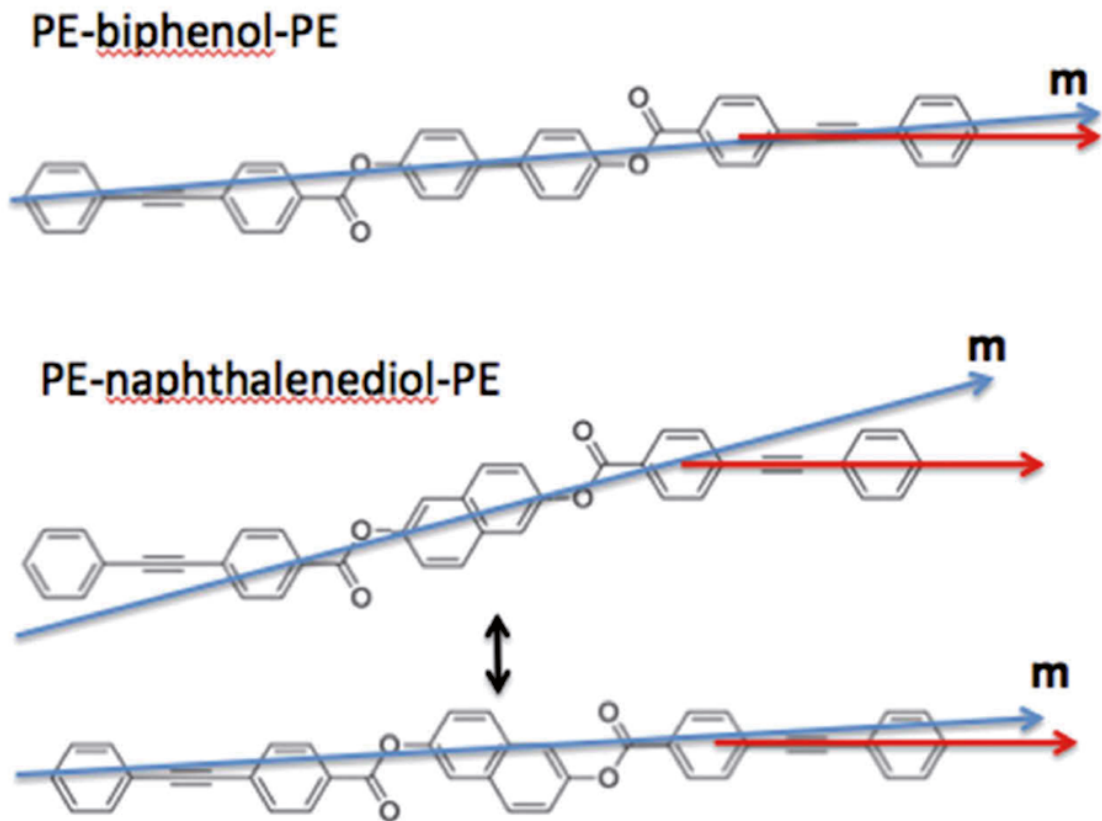
Figure 4.11 Schematic illustrations of the reactive LC model compounds with molecular long axes **m** (blue) and C≡C CSA principal axes (red). Reprinted from [144].
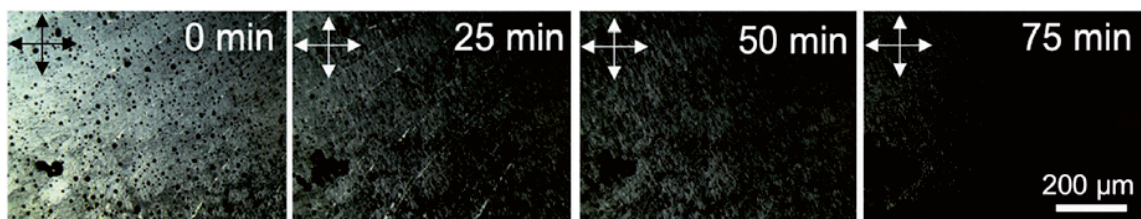
Figure 4.12 Time evolution of birefringent, N texture of PE-naphtalenediol-PE between crossed polarizers of an optical microscopy at constant temperature (310 °C). To enable comparison of birefringence, the exposure time was maintained constant at 30 s. The N birefringence decreases with increasing cure time and becomes nearly isotropic after ∼ 75 min. Model compound PE-biphenol-PE behaves similarly. Reprinted from [144].

showing that both model compounds PE-biphenol-PE and PE-naphtalenediol-PE do in fact become isotropic on holding them at temperatures in excess of 300 °C, we conclude that unlike the XRD that probes the entire sample – fully N to N droplets in an I cross-linked network to completely isotropic – the NMR data is disproportionately weighted by unreacted oriented $C\equiv C$ bonds in persistence N droplets until the chemically shifted NMR signal is no longer visible because the remaining $C\equiv C$ bonds are either in the I state or they have reacted. These two sets of complementary observations imply that the final morphology of the cured LC thermoset model compounds is an isotropic one. But unlike PE-biphenol-PE and PE-naphtalenediol-PE, higher molecular weight oligomers (macromonomers) appear to become trapped in a N glassy morphology as those solids remain birefringent throughout the chain extension/cross-linking solidification process [153]. In such high molecular weight macromonomers the cross-linking 'defects' are more dilute and the LC thermoset vitrifies before the N morphology is destroyed.

4.6   Conclusions

Because of their well-defined structure and low molecular weight, rod-like reactive mesogens PE-biphenol-PE and PE-naphtalenediol-PE represent convenient model compounds to study cross-linking and chain extension reactions in the N phase of PE-terminated LC thermoset macromonomers. In particular, ^{13}C NMR measurements provided a quantitative estimation of the first-order reaction rates of PE endgroups and of their orientational order parameter. While the latter was found to be relatively unaffected by the proceeding reaction, XRD data showed the formation of a cybotactic N phase in the unreacted compounds and a gradual loss of the molecular long axis orientational order upon curing. These results can be rationalized by considering the formation of N droplets of unreacted monomers within an I crosslinked matrix. The difference in the molecular order parameters of model compounds PE-biphenol-PE and PE-naphtalenediol-PE can be ascribed to their specific molecular structures, resulting in a different degree of conformational isomerization. These findings differ substantially from those obtained for higher molecular weight oligomeric macromonomers, which retain N morphology in a glassy state upon curing. These differences emphasize the complex relationship between the molecular structure of well-defined model compounds investigated here and the robustness of the N order and its compatibility with cross-linking and chain extension reactions in mixtures of high molecular oligomers.

Appendix A

Orientational order parameter from X-ray diffraction pattern

The orientational order parameter $\langle P_2 \rangle$ can be evaluated by fitting the azimuthal profile of the wide-angle feature, following the method described by Davidson *et al.* [154]. According to this approach, the wide-angle equatorial scattering is caused by interference in the radiation transversely scattered within small clusters composed of tens of nearly parallel molecules and its azimuthal broadening originates from the orientational disorder among different clusters. The azimuthal intensity profile $I(\gamma)$ can thus be numerically related to the cluster orientational distribution function (ODF) $f_d(\theta)$ [155]. Here θ is the angle formed by (a cluster of) molecules with the molecular director **n**, while γ is the azimuthal angle on the detector measured with respect to the equatorial axis.

Retrieval of $f_d(\theta)$ is simplified if one assumes a Maier-Saupe ODF:

$$f_d(\theta) \approx f(\cos\theta) = Z^{-1} e^{m\cos^2\theta} \tag{A.1}$$

where Z is the normalization constant and m the unknown temperature-dependent parameter describing the strength of orientational order within Maier-Saupe theory. With this assumption, the azimuthal intensity can be fitted by the expression

$$I(\gamma) = k\frac{e^{m\cos^2\gamma}}{Z\sqrt{m}\cos\gamma}\frac{\sqrt{\pi}}{2}erf(\sqrt{m}\cos\gamma) \tag{A.2}$$

with k and m fitting parameters, the former being an intensity scale factor. This allows the evaluation of m, and hence the corresponding ODF, as a function of temperature. Finally the orientational order parameter $\langle P_2 \rangle$ can be calculated as :

$$\langle P_2 \rangle = \int_0^1 P_2(\cos\theta) f(\cos\theta) d(\cos\theta) \tag{A.3}$$

where P_2 is the second-order Legendre polynomial of $\cos\theta$.

Chapter 5

Non-lamellar lyotropic liquid crystalline nanocarriers for the next generation of nanomedicine

5.1 Introduction

The lyotropic LC nanomaterials described in Section 1.2 represent an emerging class of materials of particular interest for pharmaceutical and biomedical applications. They are biocompatible, low toxic materials, chemically stable and having hydrophilic and hydrophobic domains allowing the incorporation guest molecules of hydrophilic, lipophilic and/or amphiphilic nature. The lyotropic LC systems with 2D inverse hexagonal and 3D cubic symmetry can be dispersed in water by adding steric stabilizers to obtain stable colloidal dispersions which are much less viscous, these dispersions are known as hexosomes and cubosomes, respectively. Furthermore, these nanoparticles can be functionalized increasing the therapeutic effect and reducing side effects by avoiding exposure of healthy tissues. Cubosomes and hexosomes have also been conjugated with antibodies making them more attractive for targeted delivery of chemotherapeutic drugs. There are several reviews that show the diverse applications for lyotropic LC nanoparticles such as delivery of drugs, bioactive molecules, contrast agents for desease treatment and medical imaging. Moreover, the majority of lyotropic LC nanoparticles consist of lipid and surfactants which make them more biocompatible and biodegradable than other types of nanoparticles for biomedical application such as carbon nanotubes, metallic nanoparticles, quantum dots and certain polymers. Since the structural control is of primary importance for the mechanism of nanocarriers' assembly and loading, recent publications highlight the key role of the SAXS investigations

for these novel nanomedicine carriers [24, 156–158]. The inverse non-lamellar lyotropic LC mesophases, hexosomes and cubosomes, are particularly advantageous owing to their ability to tune membrane curvature by varying the amphiphilic composition. Therefore, the addition of ionic surfactants, cationic or anionic to lipid composition, may influence their phase behaviour and their structural properties, such as bilayer thickness, water channel diameter and interfacial curvature, resulting in specific amphiphile self-assembly materials. The amphiphilic lipids most commonly used in lyotropic LC research are glyceryl monooleate (GMO) and glyceryl monolinoleate (MLO), both forming a bicontinuous cubic phase in excess water. However, the ester-based structure of these lipids may limit their practical application because of undesirable hydrolysis of the ester linkage within the monoglyceride headgroups upon long term storage or as a result of enzymatic breakdown. PHYT (3,7,11,15-tetramethylhexadecane-1,2,3-triol) has the same physicochemical characteristics of GMO or MLO but with a relatively higher resistance to hydrolysis due to the lack of ester linkages and the presence of saturated phytanyl backbone [156, 159]. Moreover, being a cosmetic ingredient, PHYT is easily available and relatively cheap, so that it can be considered a better candidate than GMO or MLO in drug delivery research. Phase behaviour of PHYT has been extensively studied [156, 159]: just like GMO, it forms an inverse bicontinuous cubic $Pn3m$ phase in excess water at room temperature and a reverse hexagonal phase H_{II} at higher temperatures. The cubic to hexagonal phase transition for PHYT/water system occurs at lower temperature (40 °C) [159] as compared to GMO/water system (80 °C) and this represents an attractive feature for PHYT in biochemical applications where chemical stability of lyotropic LC phases and their formation at temperatures close to human body ones are of major concern.

The possibility of tuning the water channel networks in bicontinuous LC cubic lipid phases can be obtained by incorporation of lipids or other surfactants with charged headgroups [160–164]. For example, swollen bicontinuous cubic phases of space group $Im3m$ were generated by inducing electrostatic repulsion across the water channel upon addition of anionic lipids, DOPG (1,2-dioleoyl-sn-glycero-3-phosphoglycerol) and DOPS (1,2-dioleoyl-sn-glycero-3-phospho-L-serine) [161] or cationic DOMA (dioctadecyldimethylammonium bromide) [165] to monoolein. Incorporation of both anionic and cationic surfactants to PHYT determined its phase transition from a cubic to a lamellar phase [166, 167]; whereas addition of up to 30% oleic acid favoured the formation of an inverse hexagonal phase at acidic and neutral pH and of a cubic phase at higher pH [168]. These tunable properties of the lipid nanocarriers make them as adaptive supramolecular nanomaterials. Within this frame, it was carried out a study on the ability of a cationic surfactant, DDABr, to modulate the phase behaviour of PHYT bulk or dispersed cubic phases and to control the pore size

of the aqueous channels and the membrane interface charge. Therefore, such study is of considerable interest for the potential use of these self-assembling materials for the encapsulation and the delivery of hydrophilic drugs, especially in ionic form, which accommodate in the aqueous water channels, shielded from the surrounding environment. The possibility of altering the interfacial charge on the surface of the particles, contributing to more desirable interactions with the loaded cargo or to differences in the cellular uptake [169, 170], makes these systems good candidates for the entrapment and delivery of ionic drugs. Recently, these nanostructures have received considerable attention as anticancer drugs delivery systems and various antineoplastic molecules have been encapsulated in GMO and PHYT-based lipid formulations in order to improve their stability, biodistribution and therapeutic efficacy. For example, GMO or PHYT cubosomes were demonstrated to improve the therapeutic potential of doxorubicin [171, 172], docetaxel [173] or paclitaxel [174] for the treatment of various kind of cancers.

In this study bulk PHYT/DDABr cubic phases and cubosomes dispersions of PHYT/DDABr were prepared, in the presence of the steric stabilizer Pluronic F127, and loaded with the antineoplastic agent 5-fluorouracil, in neutral (5-FU) and anionic form (5-FUs). The 5-fluorouracil is one of the major agents clinically used, alone or in combinations with other chemotherapy agents, for the treatment of stomach, colorectal, gastric, head and neck, and breast cancers. In particular, 5-fluorouracil is often used for the treatment of Triple Negative Breast Cancer (TNBC), one of the most aggressive subtypes of breast cancer, associated with the worst prognosis [175]. 5-fluorouracil is an antimetabolite of the pyrimidine analogue type which, due to its structure, interferes with nucleoside metabolism and can be incorporated into DNA and RNA, leading to cytotoxicity and cell death. The current mode of treatment with intravenous administration is often inconvenient. In fact, due to its high rate of metabolism in the body and to its short half-life (10-20 min) [176], costly and repeated doses are required to maintain a therapeutic serum concentration. In addition, 5-fluorouracil is rapidly absorbed through blood capillaries into systemic circulation resulting in low levels of drug near the tumor sites and consequent loss of efficacy along with higher toxicity [177]. Therefore, 5-fluorouracil requires an effective delivery vector for appropriate therapy. All the formulations prepared were characterized by synchrotron SAXS, ATR-FTIR spectroscopy, UV-Vis spectroscopy and DLS.

5.2   Characterization of liquid crystalline gels

The first step was to characterize the different formulations of PHYT/DDABr in gel phases unloaded or loaded with the drug by means of SAXS technique and ATR-FTIR spectroscopy.

SAXS experiments were carried out to investigate the internal nanostructure of PHYT/DDABr LC phases in water and the possible geometrical and topological modifications induced by encapsulation of 5-fluorouracil both in neutral and anionic form . ATR-FTIR spectroscopy was used to verify the encapsulation of 5-fluorouracil, both neutral and in anionic form, in PHYT/DDABr matrices and possibly to investigate the nature of the interactions between the drug and the carrying nanosystems.

5.2.1 Preparation of blank and drug loaded gels

Samples of blank bulk lyotropic LC phases were prepared by co-dissolving PHYT (50 mg), DDABr (3-10 mol%) and Pluronic F127 (10% w/w of total lipid) in chloroform. The PHYT has been reported to exhibit lyotropic phase behaviour as described in Section 1.2 and forms a bicontinuous cubic phase in excess of water at room temperature and reverse hexagonal phase at higher temperatures [178]. It is a biocompatible compound with high chemical stability due to the absence of ester linkages and of unsaturated bonds in the chain. DDABr is one of the most common cationic lipids added in the preparation of positively charged lyotropic LC matrices. The steric stabilizer Pluronic F127, a block *co*-polymer typically used in the preparation of the dispersions to avoid aggregation of the nanoparticles, was included in all the formulations (bulk and dispersed phases) to have the same compositions for all the systems. The chloroform was evaporated under a stream of nitrogen and the mixture dried under vacuum. Water (200 μl) was added and the mixture was vortexed to achieve a homogeneous state and equilibrated at room temperature for 24 h to hydrate the system and obtain the cubic phase gel.
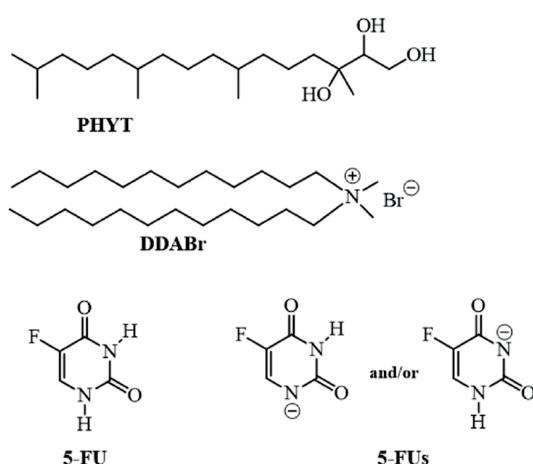
Figure 5.1 Chemical structures of phytantriol (PHYT), didodecyldimethylammonium bromide (DDABr), 5-fluorouracil in neutral (5-FU) and anionic (5-FUs) forms

5-Fluorouracil loaded cubic gels were prepared by adding 200 μl of 10 mg/ml 5-FU neutral solution (5-FU) or of 50 mg/ml 5-FU alkaline one (5-FUs), instead of water, to the dried PHYT/F127/DDABr mixtures prepared as described for the blank gel. After vortexing, mixtures were maintained at room temperature for 24 h for promoting the gel formation.

5.2.2 SAXS measurements

SAXS experiments were performed at the high brilliance beamline ID02 at the ESRF (Grenoble, France). 2D diffraction patterns were recorded by a Rayonix MX-170HS detector using an incident beam wavelength λ=0.995 Å) and a sample to detector distance of 1.0 m. The investigated q-range was comprised between 0.3 nm^{-1} and 6 nm^{-1}. The samples were held in 1 mm diameter glass capillaries. Measurements were performed from 22 °C to 40 °C and a maximum exposure time of 1 s/frame was used to avoid radiation damage. Satisfactory statistics were attained by repeating several measurements on fresh samples. The collected 2D diffraction spectra were angularly integrated to get 1D intensity vs q patterns. The cubic lattice parameter a and the water channel radius r_w was calculated through the linear fit of the plot q_{hkl} vs $\sqrt{h^2 + k^2 + l^2}$ whereas the water channel radius was estimated using the relation:

$$r_w = [(-\sigma/2\pi\chi)^{1/2}a] - l \qquad (5.1)$$

where l is the lipid length ($\sim$ 1.4 nm) and σ and χ are topological constants, characteristic of a given cubic phase (for *Pn3m* structure σ=1.919 and $\chi = -2$, for *Im3m* structure σ=2.345 and $\chi = -4$).

The incorporation of steric stabilizer Pluronic F127 had no effect on the observed mesophases of both unloaded and loaded PHYT/DDABr. PHYT alone, in excess of water, formed a cubic phase with the double-diamond (*Pn3m*) symmetry and a lattice parameter of 6.51 nm [157]. Addition of a cationic surfactant induced structural changes as shown in Fig. 5.2 and in Tab. 5.1, where the SAXS patterns of PHYT/DDABr systems with increasing DDABr content and the corresponding structural parameters are reported, respectively. In detail, for PHYT/DDABr system containing 3 mol% DDABr, a *Pn3m* cubic phase was still observed with an increased cell unit (a = 7.21 nm) with respect to PHYT alone. The presence of a positive charge on DDABr molecule induces an increase of the effective head group size and hence a reduction in negative curvature and the formation of a swollen *Pn3m* mesophase [166]. In the range 5–8 mol% DDABr, a phase transition from *Pn3m* to *Im3m* was evident, whereas the scattering peaks associated with the cubic phases disappeared for cationic lipid concentration of 10 mol%. In this case, a multilayer L$_\alpha$ phase with large d-spacing (a = 48.5 nm) was observed in the low scattering vector region. A similar trend was reported
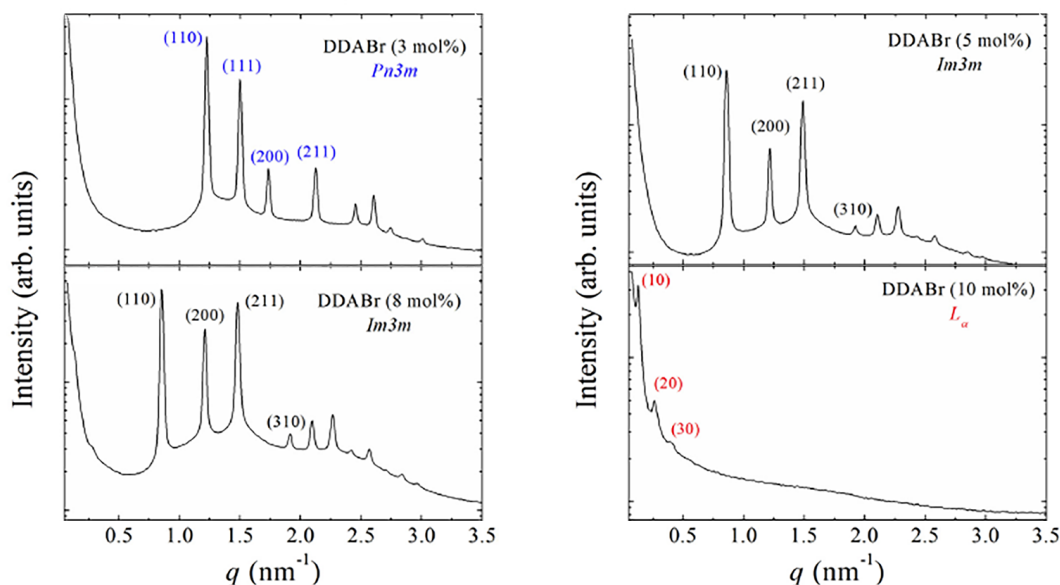
Figure 5.2 Synchrotron SAXS profiles of PHYT/DDABr bulk phase with increasing DDABr content (3–10 mol%) in water at 20°C. Adapted from [158].

by Liu *etal*. [166] and this behaviour can be justified using the critical packing parameter (CPP). With a packing parameter larger than 1, PHYT tends to form a *Pn*3*m* cubic phase in the presence of an excess of water. In contrast, the CPP value for DDABr is close to 1 [166], favouring the formation of vesicles in water. Hence, the addition of DDABr to PHYT may decrease the effective CPP of the system, inducing a transition from the cubic to the L$_\alpha$ phase. The addition of the anticancer agent 5-FU, in the neutral and anionic form, further influenced the phase behaviour of these ordered nanostructures and the effect of drug encapsulation on the cubic phase (3–8 mol% of DDABr) was analyzed. Representative SAXS scattering profiles of PHYT/DDABr systems containing neutral 5-FU with increasing amounts of DDABr are shown in Fig. 5.3(a). At low percentages of DDABr (3 mol%), the double diamond cubic phase, *Pn*3*m*, was still present but a decrease in the lattice parameter was observed, from *a* = 7.21 to 6.92 nm (Tab. 5.1). Also at 5 mol% of DDABr, the *Im*3*m* cubic space group observed for the unloaded system did not change upon addition of 5-FU, and only the lattice parameter decreased, from *a* = 10.34 to 9.78 nm. Assuming that the length of the lipid does not change, this suggests that the presence of 5-FU, a hydrophilic drug, may reduce the solvation of the lipid headgroup and lead to the shrinkage of the water channels as reported in Tab. 5.1 [179]. At 8 mol% of DDABr, the coexistence of *Im*3*m* and L$_\alpha$ phases was observed for PHYT/DDABr(8)/5-FU, whereas with PHYT/DDABr(8) the L$_\alpha$ phase appeared only at 10 mol% DDABr. Hence, in 5-FU loaded PHYT/DDABr

the sequence of phase transitions of the unloaded system (from *Pn3m* to L_α through an *Im3m* intermediate) remains the same, but with the L_α phase appearing already at 8 mol% of DDABr.
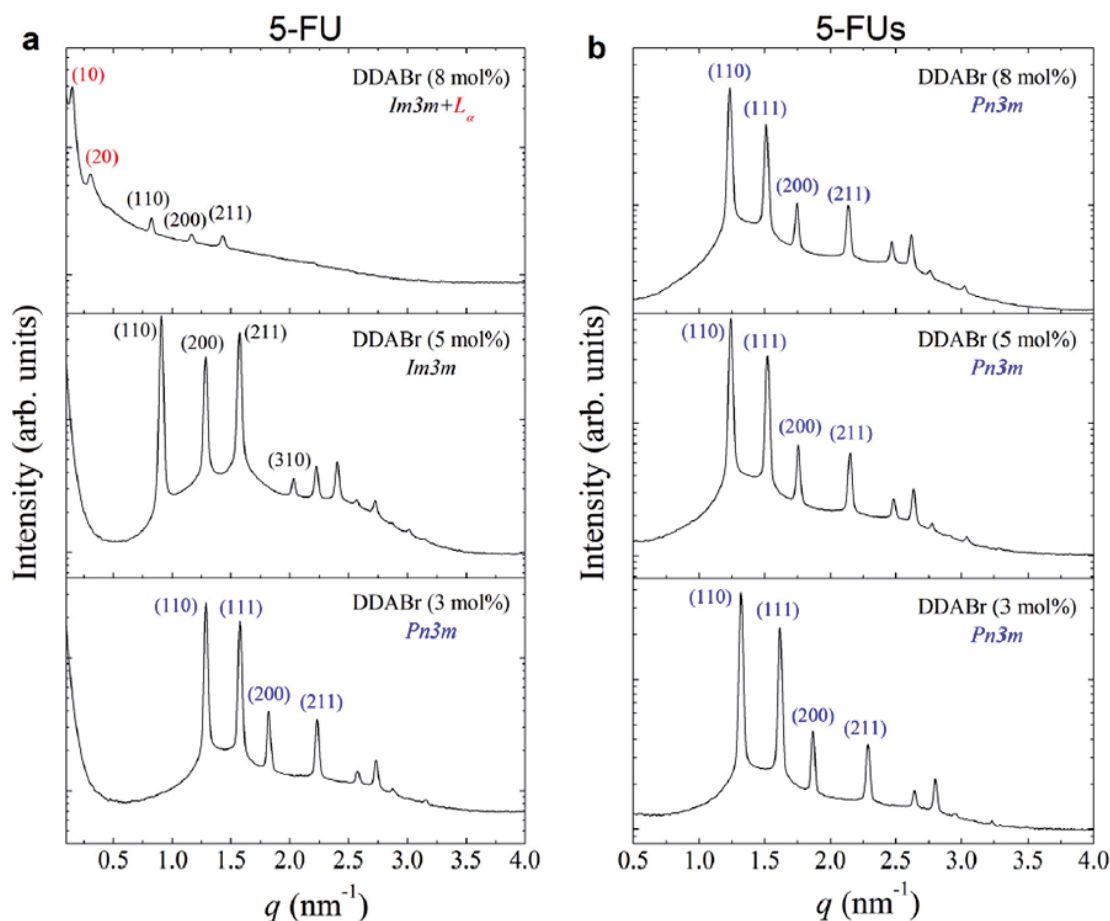
Figure 5.3 Synchrotron SAXS profiles of PHYT/DDABr (3, 5 and 8 mol%) bulk phase loaded with (a) neutral 5FU, and (b) anionic 5-FUs, at 20 °C. Reprinted from [158].

Fig. 5.3 (b) shows the phase behaviour of PHYT/DDABr matrices loaded with anionic 5-FUs. A *Pn3m* space group was observed for all the systems, included those containing 8 and 10 mol% DDABr. The positive charges of the DDABr headgroup, responsible for the reduced negative curvature in PHYT/DDABr matrices, are shielded by the anionic 5-FUs through the electrostatic interactions between them and the *Pn3m* cubic phase is stabilized. The system switches to a mesophase characterized by a higher negative curvature resulting by an increasing in charge screening and by a reduced effective headgroup area at the lipid-water interface.

Table 5.1 Phase structure, lattice parameter and water channel radius of PHYT/DDABr bulk phase, empty and loaded with 5-FU and 5-FUs, at increasing amounts of DDABr. Adapted from [158].

DDABr mol%	Blank	5-FU	5-FUs
0% [157]	$Pn3m$ a=6.51 nm r_w=1.14 nm	$Pn3m$ a=6.53 nm r_w=1.51 nm	$Pn3m$ a=6.71 nm r_w =1.22 nm
3%	$Pn3m$ a=7.21 nm r_w=1.42 nm	$Pn3m$ a=6.92 nm r_w=1.30 nm	$Pn3m$ a=6.73 nm r_w=1.23 nm
5%	$Im3m$ a=10.34 nm r_w=1.76 nm	$Im3m$ a=9.78 nm r_w=1.59 nm	$Pn3m$ a=6.82 nm r_w=1.26 nm
8%	$Im3m$ a=10.38 nm r_w=1.77 nm	$Im3m/L_\alpha$ a=10.83/41.94 nm r_w=1.59 nm	$Pn3m$ a=7.15 nm r_w=1.39 nm

The influence of the temperature on the phase behaviour of PHYT/DDABr and PHYT/DDABr loaded with 5FU, in the neutral or anionic form, was also analyzed from 20 °C to 40 °C as shown in Fig. 5.4. In all cases, independently of the DDABr content, a slight decrease in the lattice parameters was observed at higher temperatures, in agreement with previous literature reports [180–182]. In fact, the increase in the lipid chain conformational disorder upon heating induces a reduction of the lattice parameter of bicontinuous cubic phases and an increase in the magnitude of the bilayer spontaneous inverse curvature. With PHYT/DDABr(5), empty and loaded with neutral 5-FU, the $Pn3m$ phase, with a higher negative curvature, appeared starting from 34 °C and partially coexisted with the $Im3m$ phase.
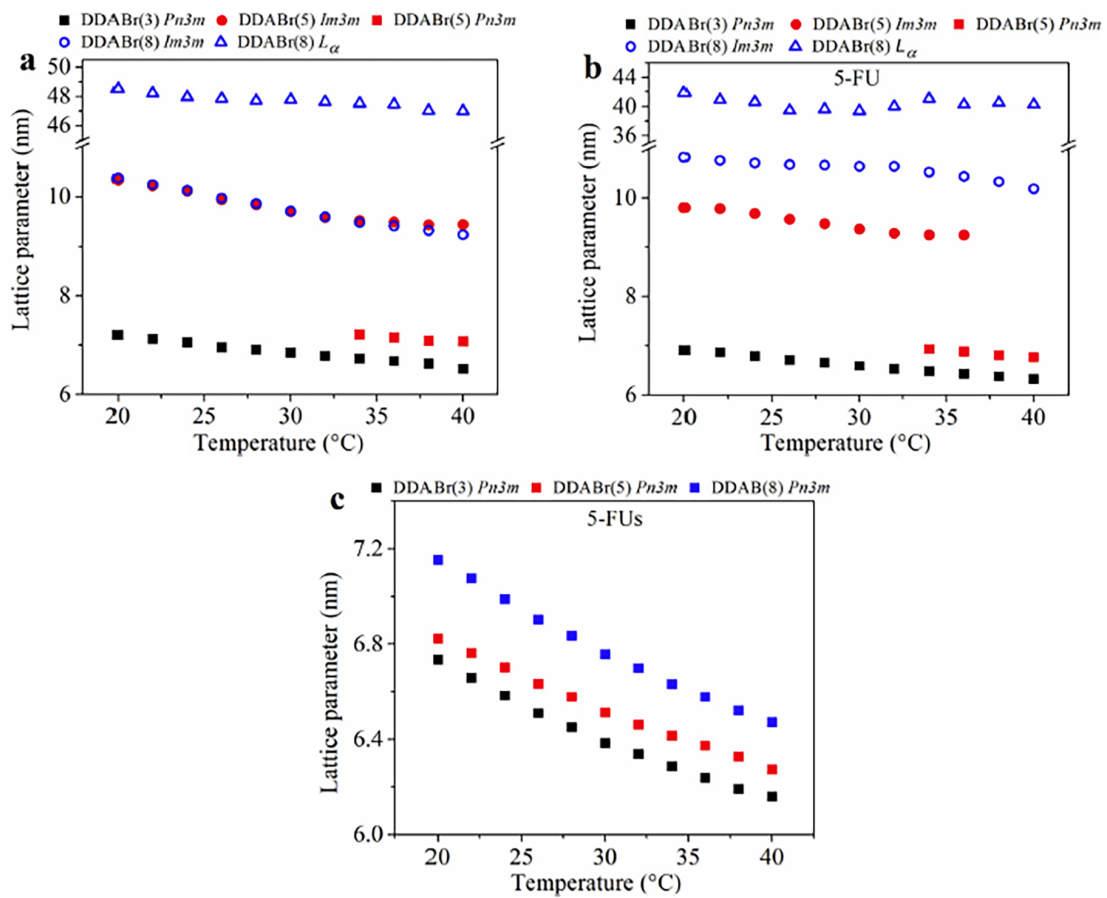
Figure 5.4 Changes in lattice parameter *a* as a function of the temperature (20–40 °C) and at increasing DDABr content for the three systems (a) PHYT/DDABr, (b) PHYT/DDABr/5-FU and (c) PHYT/DDABr/5-FUs. Adapted from [158].

5.2.3 ATR-FTIR experiments

ATR-FTIR measurements were carried out at the infrared SISSI beamline, Elettra Sincrotrone Trieste (Trieste, Italy), by using the MIRacle Single Reflection ATR box (PIKE technologies) with diamond crystal, equipped with a Vertex 70 interferometer (Bruker Optics GmbH) and a Deuterated TriGlycine Sulfate (DTGS) detector. Samples were deposited onto the diamond crystal and ATR-FTIR spectra were collected at room temperature, every 5 s, under a continuous stream of nitrogen until sample dehydration, followed by vanishing of the combination band of bending and liberation water modes, centred at about 2100 cm^{-1}, below the detection limit. Each spectrum was acquired in the spectral range 5000–550 cm^{-1} and averaged over 128 scans with a spectral resolution of 4 cm^{-1}. Before each sample acquisition, the background spectrum was collected on the clean diamond crystal, under the same conditions. Raw spectra were corrected for carbon dioxide and water vapour using OPUS 7.5 routine (Bruker Optics GmbH), and then vector normalized in the entire spectral range of acquisition. The steric stabilizer Pluronic F127 was included in all the formulations and its presence has no effects on the vibrational profile of PHYT/DDABr. IR absorption bands for PHYT,DDABr, 5-FUand 5-FUs are reported in Tab. 5.2. All the IR spectra shown are reported in absorbance mode in the 1800–600 cm^{-1} spectral region (Fig. 5.5).
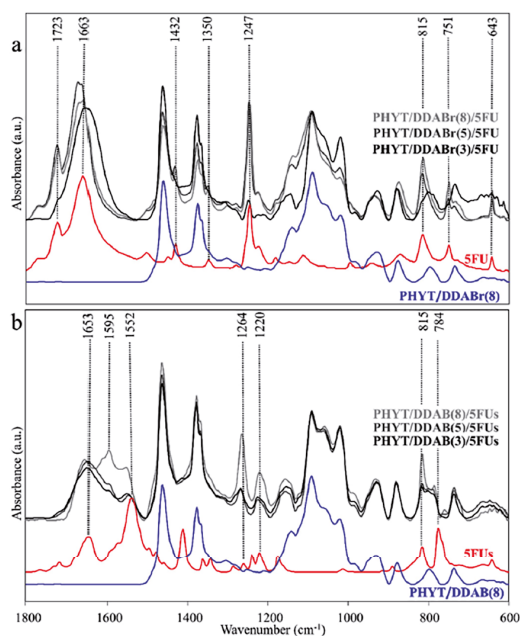
Figure 5.5 Absorbance average spectra of: (a) PHYT/DDABr(8), 5-FU and PHYT/DDABr/5-FU at increasing concentrations (3-8 mol%) of DDABr; (b) PHYT/DDABr(8), 5-FUs and PHYT/ DDABr/5-FUs at increasing concentrations (3-8 mol%) of DDABr (1800-600 cm^{-1} spectral range). Reprinted from [158].

Table 5.2 IR absorption bands detected in PHYT, DDABr, 5-FU, and 5-FUs. Adapted from [158].

Compound	IR vibrational modes
PHYT [157]	1463 and 1375 cm^{-1} ($\delta CH_{2/3}$); 1091, 1061 and 1022 cm^{-1} (νC−O, νC−C and δOCH); 735 cm^{-1} (δCH)
DDABr	1467 cm^{-1} (δCH_2); 750 and 721 cm^{-1} (δCH)
5-FU	1723 cm^{-1} (νC=O); 1663 cm^{-1} (νC=C), 1432 cm^{-1} and 1350 cm^{-1} (δN−H and δC−H); 1247 cm^{-1} (νC−F); 815 cm^{-1} (νring); 751 cm^{-1} (γC=O); 643 cm^{-1} (γN-H)
5-FUs	1653 cm^{-1} (νC=C), 1595 cm^{-1} and 1552 cm^{-1} (νC=N), 1264 cm^{-1} and 1220 cm^{-1} (νC−F), 815 cm^{-1} (νring), and 784 cm^{-1} (γC=O)

The ATR-FTIR spectra of 5-FU, PHYT/DDABr(8) (representative of an unloaded matrix) and PHYT/DDABr mixtures loaded with 5-FU are reported in Fig. 5.5(a). Encapsulation of 5-FU in the three matrices was confirmed by the presence of some bands typical of the neutral form of 5-fluorouracil: 1723 cm^{-1} (νC=O), 1663 cm^{-1} (νC=C), 1432 cm^{-1} and 1350 cm^{-1} (δN−H and δC−H), 1247 cm^{-1} (νC−F), 815 cm^{-1} (νring), 751 cm^{-1} (γC=O), and 643 cm^{-1} (γN−H). These bands are particularly evident in the samples with the higher concentrations of DDABr and this could be correlated to their nanostructures, *i.e.* *Im3m* and swollen L$_\alpha$ phase, having larger aqueous compartments compared to *Pn3m* cubic phase of PHYT/DDABr(3). Notably, an absorption band was detected at 1671 cm^{-1}, more evident in PHYT/DDABr(5)/5FU and PHYT/DDABr(8)/5FU, suggesting an interaction between the drug and the lipid matrix, mainly localized at the C=C bond.

The ATR-FTIR spectra of 5FUs, PHYT/DDABr(8) and 5-FUs loaded PHYT/DDABr mixtures are reported in Fig. 5.5(b). The following bands characteristic of 5-FUs are clearly visible in the spectra of the three samples: 1653 cm^{-1} (νC=C, 1595 cm^{-1} and 1552 cm^{-1} (νC=N), 1264 cm^{-1} and 1220 cm^{-1} (νC−F), 815 cm^{-1} (νring), and 784 cm^{-1} (γC=O). In particular in PHYT/DDABr(8)/5FUs spectrum, some of these bands, 1595 cm^{-1}, 1552 cm^{-1}, 1264 cm^{-1}, 1220 cm^{-1}, and 815 cm^{-1}, show higher absorbance values suggesting that C=N and C−F bonds are more involved in the interactions between the drug and the cationic matrix.

5.3 Characterization of liquid crystalline nanodispersions

The lipid dispersions were prepared and analysed at two different concentrations of DDABr (3 and 5 mol%). To the naked eye, while pure PHYT dispersions were milky in appearance, on the addition of the ionic surfactant they became more transparent, as already observed for similar systems [166, 183]. This is possibly due to the reduction of the average particle size observed for increasing DDABr concentrations (see below), resulting in a lower Rayleigh scattering cross section. These formulations were analysed by means of DLS and UV-Vis spectroscopy.

5.3.1 Preparation of nanostructured lipid dispersion

To prepare the lipid dispersions, 2000 μl of water were added to the gels and the samples were sonicated by a probe sonicator for 10 min in pulse mode (1 s pulses interrupted by 1 s breaks) at 50% of the maximum power.

5.3.2 Particle size and Zeta potential measurements

The particle size (Z-average), polydispersity index (PDI) and zeta potential (Zp) value of the dispersions were determined using the Malvern Zetasizer Nano ZS (Malvern Instruments GmbH). Samples were properly diluted and measured in PMMA cuvettes or DTS1070 capillary cells for the determination of size and Zp, respectively. All measurements were performed in triplicate at 25 °C on three independent samples. Data were analysed using Dispersion Technology Software V 5.03 provided by Malvern Instruments.

Table 5.3 Size, Polydispersity Index (PDI), Zeta Potential (Zp) of PHYT/DDABr (3 and 5mol%) nanoparticles, empty and loaded with 5-FUand 5-FUs, together with the corresponding Entrapment Efficiency (EE%). Adapted from [158].

Formulations	Size (nm)	PDI	Zp (mV)	EE (%)
PHYT	215.1 ± 1.7	0.224 ± 0.009	-33.8 ± 1.8	
PHYT/DDABr(3)	158.5 ± 1.8	0.166 ± 0.012	+43.0 ± 0.7	
PHYT/DDABr(5)	106.1 ± 1.8	0.283 ± 0.009	+45.7 ± 2.7	
PHYT/DDABr(3)/5-FU	177.5 ± 1.4	0.125 ± 0.024	+40.4 ± 0.64	25.7 ± 4.6
PHYT/DDABr(5)/5-FU	86.4 ± 1.1	0.254 ± 0.011	+44.3 ± 3.2	45.3 ± 2.9
PHYT/DDABr(3)/5-FUs	203.0 ± 2.3	0.182 ± 0.026	+31.5 ± 1.4	27.6 ± 6.3
PHYT/DDABr(5)/5-FUs	192.8 ± 2.4	0.140 ± 0.050	+32.1 ± 0.4	36.4 ± 5.1

The particle size of PHYT/DDABr dispersions decreased with increasing DDABr content, as reported in Tab. 5.3, and was smaller than the size of cubosomes made of PHYT alone

(215 nm). This trend agrees with other literature reports [157, 166, 167] and, as already observed, it could be due to higher surfaces repulsive forces which protect nanoparticle from aggregation.

The surface electrostatic potential of the dispersed particles was evaluated by Zp measurements (Tab. 5.3). As expected, incorporation of the positively charged DDABr resulted in a considerable increase of the potential,which changed from a slightly negative value for pure PHYT dispersions (-33.8 eV) to more +40 eV for the cationic ones.

When 5-FU was encapsulated in PHYT/DDABr, no visual changes were observed on the dispersions, being rather milky in the case of DDABr(3) and almost transparent with DDABr(5), in agreement with a progressive reduction of the average particle size. In particular, at 5 mol% DDABr and in the presence of 5-FU the dispersion was rather viscous and comprised a significant contribution from particles smaller than 100 nm.

Instead, upon encapsulation of 5-FUs in PHYT/DDABr, the dispersions turned milky again both at 3 and 5 mol% DDABr. Correspondingly, the particle size increased to $\sim$ 200 nm, closer to the size of cubosomes with PHYT alone, again with PHYT/DDABr(5)/5-FUs nanoparticles being slightly smaller than those with 3 mol% DDABr.

PDIs were in the approximate range 0.12–0.28, indicating moderately homogeneous systems especially at low DDABr concentration and/or in the presence of 5-FUs.

Positive Zp values for PHYT/DDABr/5-FU dispersions were determined with almost no differences with the empty cubosomes, whereas encapsulation of 5-FUs still resulted in a positive Zp but lower ($\sim$ +30 eV) than those measured for PHYT/DDABr and PHYT/DDABr/5-FU systems. Neutralization of DDABr positive charges by anionic 5-FUs may occur at the interface lipid bilayer/aqueous channels, but some positive charges may still be present on the nanoparticles surface thus imparting a positive potential.

5.3.3   Determination of 5-fluorouracil content in cubosomes

Free 5-FU or 5-FUs (non-encapsulated in the cubosomes) was separated by ultrafiltration method: aliquots of the drug loaded dispersions were centrifuged in an Amicon Ultra (Amicon Ultra-4, 10,000 MW, Millipore) at 10,000 rpm for 15 min. The obtained filtrates were diluted (1:100) with methanol and spectrophotometrically read at λ_{max} = 266 nm for free 5-FU/5-FUs. The total amount of 5-FU/5-FUs (free and encapsulated) was determined after addition of methanol (1:100) to an aliquot of the drug loaded dispersions to dissolve the lipid. The resultant solution was spectrophotometrically assayed at λ_{max} = 266 nm for total 5-FU/5-FUs content using methanol as the blank. The EE(%) was calculated by the following equation:

$$EE(\%) = \frac{W(T) - W(F)}{W(T)} \times 100 \ , \tag{5.2}$$

where $W(T)$ is the total drug in cubosomes, and $W(F)$ is the free drug in the filtrate. All the experiments were repeated at least three times and measurements were run in triplicate. Functionalization of cubic phase LCs with DDABr was performed to modulate the mesophase structure and to improve the capacity of these nanoparticles to encapsulate 5-fluorouracil drug. As reported in Tab. 5.3, modest EE values for 5- FU or 5-FUs in PHYT/DDABr cubosomes were obtained, especially at 3 mol% DDABr. In this latter case, there were no differences between the neutral and anionic drug with EE values. As evidenced by SAXS measurements, the amount of added DDABr was likely not high enough to affect the phase behaviour or the entrapment capacity of the system. This low EE is consistent with the hydrophilic character and the small size of the drug molecule which is preferably located in the aqueous phase, both in the channels within the lipid bilayer architecture and in the solvent in which cubosomes are dispersed, rather than in the lipid phase (log $P_{octanol/water} = -0.85$) [184]. Moreover, it is not excluded that the small 5-FU or 5-FUs molecules leak out from the cubosomes aqueous channels during the ultrafiltration procedure [185]. When the DDABr content increased, an improvement of the entrapment capacity of the system was observed in both cases. Electrostatic interactions between the negatively charged 5-FUs molecules and the cationic DDABr headgroups favoured drug entrapment in the cubosomes and in fact a $\sim 10\%$ increase in EE was obtained when the DDABr content changed from 3 to 5 mol %. Surprisingly a higher value EE (45%) was determined with PHYT/ DDABr(5)/5-FU, but it is difficult to ascertain whether this result was actually due to an improved encapsulation in the *Im3m* phase with larger aqueous compartments or to the particular aspect of PHYT/ DDABr(5)/5-FU system. Actually, the dispersion was rather viscous, and it is not excluded that this fact influenced the ultrafiltration procedure, the volumes collected after the centrifugation and hence the measured EE value.

Dispersions with a higher content of DDABr were not considered for EE determinations because they were not uniform and large aggregates were present.

5.4   Conclusions

In this work, it has been examined the effect of a cationic surfactant, DDABr, on the cubic phase behaviour of PHYT system and observed that its addition destabilized the *Pn3m* cubic phase, promoting the formation of an *Im3m* and, at higher concentration, of a L$_\alpha$ phase. In fact, the presence of DDABr in the cubic structure causes an increase in the surface charge

density, an enhancement of the electrostatic repulsions between charged lipid headgroups and hence a decrease of the negative interfacial curvature. In addition, the examination of the phase behaviour of PHYT/ DDABr systems loaded with the chemotherapy agent 5-fluorouracil reveals that anionic 5-FUs stabilizes the *Pn3m* cubic phase at all DDABr concentrations, whereas the neutral 5-FU has no effect on the PHYT/DDABr phases sequence. PHYT/DDABr cubosome dispersions were prepared and loaded with 5-fluororacil, with EE values consistent with the hydrophilic character and the small size of the drug molecule located in the aqueous phase. Further investigations, such as in vitro cytotoxicity experiments, are necessary but the results here reported are quite promising. In fact, incorporation of the cationic surfactant into the PHYT bicontinuous cubic phase creates a positively charged matrix that increases the attraction and the loading of the drug, as observed in the case of anionic 5-FUs, making these systems interesting anticancer drug delivery vectors. The possibility of increasing the drug loading of the water-soluble agents through functionalization, as done in this work, allows to broaden the utility of bicountinuous cubic phase LCs. Moreover, by controlling the composition of PHYT/ionic surfactant mixtures, it is possible to obtain tunable cubic phases which could be used in a wide range of applications including protein and large biomolecules encapsulation.

Concluding remarks

The peculiar properties of the soft materials investigated in this Ph.D. thesis result from the inherent orientational and/or positional order of the LC mesophases specifically involved. In the thermotropic BCMs of Chapter 2, the key role is played by the cybotactic nanoscale structure of their N phase that is responsible for the potential biaxial structural organization of these materials and of their unique macroscopic response to external stimuli. The investigation performed on laterally methylated bent-core nematics has provided new insights into the effect of lateral substituents on the mesophase properties as well as on the local molecular order. These findings represent a significant step in the ongoing research of the structure-function relationships of this class of soft materials. In addition, they provide a useful guide to address next research efforts towards the synthesis of novel BCMs exhibiting a low temperature N phase endowed with spontaneous macroscopic biaxial order and/or ferroelectric switching behaviour.

In Chapter 3, it was demonstrated that the unconventional use of Langmuir films to deposit thin films of BCMs on solid substrates allows a fine control the molecular ordering. In particular, the in-plane anisotropy which is inherent to the technique (because of the compression direction) results in an anisotropic morphology and in a biaxial molecular organization, both extending homogenously over the whole film surface. This original result suggests the possibility of using these films as unconventional (possibly biaxial) aligning substrates for bulk LC samples. The observed biaxial order could also result in films featuring in-plane polar order, an issue of future investigation both for its fundamental implications and possible technological applications. From a different perspective, the reported results also represent the first demonstration of the usefulness of grazing-incidence XRD to study LC films at the molecular level.

The long-range orientational order of the nematogenic macromonomers typically used to produce thermosets from a N liquid crystalline melt, via polymerization-induced three-dimensional cross-linking at high-temperature, is responsible of the high-mechanical performances of the resulting polymeric material. Following the kinetics of the cross-linking process is key to monitor the development of the final material structure and to understand

the effects on it of the orientation properties of the underlying N LC phase. The combined XRD and NMR study performed in the model macromonomer compounds presented in Chapter 4, have demonstrated for the first time the possibility of monitoring the kinetics of the cross-linking process from the N melt and evaluating the degree of transfer of the orientational order from the starting fluid anisotropic mixture to the final solid polymer. These results pave the way to an extensive application of this technique in the study of the polymerization process of more general LC thermoset systems, with the final objective of optimizing the process parameters to maximize the mechanical performances of the final materials.

Lyotropic LC nanomaterials comprising mainly of amphiphilic lipids and functional additives self-assembling into one-, two- and three-dimensional nanostructures, like those reported in Chapter 5, have recently emerged as promising candidates for a next generation of materials for nano-biomedicine. The lyotropic LC nanoparticles are attractive platforms for drug delivery because of the versatility, compatibility, digestibility and bioadhesive properties of their lipid constituents. The integrated experimental approach used in this thesis work made it possible to establish the mesomorphic behaviour of the investigated materials and elucidate the effects of drug encapsulation on their nanostructures. It has been examined the effect of a cationic surfactant, DDABr, on the cubic phase behaviour of the PHYT system. In addition, the phase behaviour of PHYT/ DDABr systems loaded with the chemotherapy agent 5-fluorouracil has also been investigated. An improvement of the entrapment capacity of 5-FUs has been observed increasing the DDABr content in the system, with the cationic surfactant into the PHYT bicontinuous cubic phase creating a positively charged matrix that increases the attraction and the loading of the drug. This property makes these systems interesting anticancer drug delivery vectors. In this regard, the development of new engineered lyotropic LC vectors possibly targeted for the delivery of 5- fluorouracil to cancer cells may represent a major step towards a more effective and safer breast cancer therapy.

Bibliography

[1] R. A. L. Jones. *Soft Condensed Matter*. Oxford University Press, 2002.

[2] M. Doi. *Soft Matter Physics*. Oxford University Press, 2013.

[3] M. Mitov. *Sensitive Matter*. Harvard University Press, 2012.

[4] P. G. de Gennes and J. Prost. *The Physics of Liquid Crystals (2nd edn)*. Oxford University Press, 1993.

[5] S. Chandrasekhar. *Liquid Crystals (2nd edn)*. Cambridge University Press, 1992.

[6] M. L. Blinov. *Structure and Properties of Liquid Crystals*. Springer Netherlands, 2011.

[7] W. H. de Jeu. *Physical Properties of Liquid Crystalline Materials,*. Gordon and Breach, 1980.

[8] L. Onsager. The effects of shape on the interaction of colloidal particles. *Ann. N. Y. Acad. Sci.*, 51(4):627–659, 1949.

[9] D. Frenkel. Order through entropy. *Nature Materials*, 14:9–12, 2015.

[10] C. Tschierske and D. J. Photinos. Biaxial nematic phases. *J. Mater. Chem.*, 20:4263–4294, 2010.

[11] M. J. Freiser. Ordered states of a nematic liquid. *Phys. Rev. Lett.*, 24:1041–1043, 1970.

[12] W. L. McMillan. Simple molecular model for the smectic *a* phase of liquid crystals. *Phys. Rev. A*, 4:1238–1246, 1971.

[13] W. Helfrich. Electric alignment of liquid crystal. *Mol. Cryst. Liq. Cryst.*, 21(3-4):187–209, 1973.

[14] R. B. Meyer. Piezoelectric effects in liquid crystals. *Phys. Rev. Lett.*, 22:918–921, 1969.

[15] N. A. Clark and S. T. Lagerwall. Submicrosecond bistable electro-optic switching in liquid crystals. *Appl. Phys. Lett.*, 36(11):899–901, 1980.

[16] S. T. Lagerwall. *Ferroelectric and Antiferroelectric Liquid Crystals*. WILEY, 1999.

[17] B Jerome. Surface effects and anchoring in liquid crystals. *Rep. Prog. Phys.*, 54(3):391–451, 1991.

[18] L. M. Blinov, E. I. Kats, and A. A. Sonin. Surface physics of thermotropic liquid crystals. *Soviet Physics Uspekhi*, 30(7):604–619, 1987.

[19] P. G. de Gennes. Wetting: statics and dynamics. *Rev. Mod. Phys.*, 57:827–863, 1985.

[20] P. Guyot-Sionnest, H. Hsiung, and Y. R. Shen. Surface polar ordering in a liquid crystal observed by optical second-harmonic generation. *Phys. Rev. Lett.*, 57:2963–2966, 1986.

[21] P. Chatelain. Sur l'orientation des cristaux liquides par les surfaces frottées. *CR. Acad. Sci.*, 213:875–876, 1941.

[22] D. Meyerhofer. New technique of aligning liquid crystals on surfaces. *Appl. Phys. Lett.*, 29(11):691–692, 1976.

[23] M. Monkade, M. Boix, and G. Durand. Order electricity and oblique nematic orientation on rough solid surfaces. *EPL*, 5(8):697–702, 1988.

[24] J. Zhai, C. Fong, N. Tran, and C. J. Drummond. Non-lamellar lyotropic liquid crystalline lipid nanoparticles for the next generation of nanomedicine. *ACS Nano*, 13(6):6178–6206, 2019.

[25] J. Y. T. Chong, X. Mulet, B. J. Boyd, and C. J. Drummond. Chapter five - steric stabilizers for cubic phase lyotropic liquid crystal nanodispersions (cubosomes). volume 21 of *Advances in Planar Lipid Bilayers and Liposomes*, pages 131 – 187. Academic Press, 2015.

[26] Z. Karami and M. Hamidi. Cubosomes: remarkable drug delivery potential. *Drug Discovery Today*, 21(5):789 – 801, 2016.

[27] Koynova R. and Tenchov B. Transitions between lamellar and non-lamellar phases in membrane lipids and their physiological roles. *OA Biochemistry*, 01(1):1–9, 2013.

[28] A. Jákli, O. D. Lavrentovich, and J. V. Selinger. Physics of liquid crystals of bent-shaped molecules. *Rev. Mod. Phys.*, 90:045004, 2018.

[29] T. Niori, T. Sekine, J. Watanabe, T. Furukawa, and H. Takezoe. Distinct ferroelectric smectic liquid crystals consisting of banana shaped achiral molecules. *J. Mater. Chem.*, 6:1231–1233, 1996.

[30] O. Francescangeli, F. Vita, F. Fauth, and E. T. Samulski. Extraordinary magnetic field effect in bent-core liquid crystals. *Phys. Rev. Lett.*, 107:207801, 2011.

[31] T. Ostapenko, D. B. Wiant, S. N. Sprunt, A. Jákli, and J. T. Gleeson. Magnetic-field induced isotropic to nematic liquid crystal phase transition. *Phys. Rev. Lett.*, 101:247801, 2008.

[32] F. Vita, I. F. Placentino, C. Ferrero, G. Singh, E. T. Samulski, and O. Francescangeli. Electric field effect on the phase diagram of a bent-core liquid crystal. *Soft Matter*, 9:6475–6481, 2013.

[33] J. Harden, B. Mbanga, N. Éber, K. Fodor-Csorba, S. Sprunt, J. T. Gleeson, and A. Jákli. Giant flexoelectricity of bent-core nematic liquid crystals. *Phys. Rev. Lett.*, 97:157802, 2006.

[34] C. Bailey, K. Fodor-Csorba, J. T. Gleeson, S. N. Sprunt, and A. Jákli. Rheological properties of bent-core liquid crystals. *Soft Matter*, 5:3618–3622, 2009.

[35] C. Bailey, K. Fodor-Csorba, R. Verduzco, J. T. Gleeson, S. Sprunt, and A. Jákli. Large flow birefringence of nematogenic bent-core liquid crystals. *Phys. Rev. Lett.*, 103:237803, 2009.

[36] O. Francescangeli, V. Stanic, S. I. Torgova, A. Strigazzi, N. Scaramuzza, C. Ferrero, I. P. Dolbnya, T. M. Weiss, R. Berardi, L. Muccioli, S. Orlandi, and C. Zannoni. Ferroelectric response and induced biaxiality in the nematic phase of bent-core mesogens. *Adv. Funct. Mater.*, 19(16):2592–2600, 2009.

[37] G. Shanker, M. Nagaraj, A. Kocot, J. K. Vij, M. Prehm, and C. Tschierske. Nematic phases in 1,2,4-oxadiazole-based bent-core liquid crystals: Is there a ferroelectric switching? *Adv. Funct. Mater.*, 22(8):1671–1683, 2012.

[38] F. Vita, K. Sparnacci, G. Panzarasa, I. F. Placentino, S. Marino, N. Scaramuzza, G. Portale, E. Di Cola, C. Ferrero, S. I. Torgova, G. Galli, M. Laus, and O. Francescangeli. Evidence of cybotactic order in the nematic phase of a main-chain liquid crystal polymer with bent-core repeat unit. *ACS Macro Lett.*, 3(1):91–95, 2014.

[39] M. Alaasar, S. Poppe, C. Kerzig, C. Klopp, A. Eremin, and C. Tschierske. Cluster phases of 4-cyanoresorcinol derived hockey-stick liquid crystals. *J. Mater. Chem. C*, 5:8454–8468, 2017.

[40] F. Vita, F. C. Adamo, and O. Francescangeli. Polar order in bent-core nematics: An overview. *J. Mol. Liq.*, 267:564 – 573, 2018. Special Issue Dedicated to the Memory of Professor Y. Reznikov.

[41] L. A. Madsen, T. J. Dingemans, M. Nakata, and E. T. Samulski. Thermotropic biaxial nematic liquid crystals. *Phys. Rev. Lett.*, 92:145505, 2004.

[42] B. R. Acharya, A. Primak, and S. Kumar. Biaxial nematic phase in bent-core thermotropic mesogens. *Phys. Rev. Lett.*, 92:145506, 2004.

[43] A. G. Vanakaras and D. J. Photinos. Thermotropic biaxial nematic liquid crystals: Spontaneous or field stabilized? *J. Chem. Phys.*, 128(15):154512, 2008.

[44] S. D. Peroukidis, P. K. Karahaliou, A. G. Vanakaras, and D. J. Photinos. Biaxial nematics: symmetries, order domains and field-induced phase transitions. *Liq. Cryst.*, 36(6-7):727–737, 2009.

[45] E. T. Samulski. meta-cybotaxis and nematic biaxiality. *Liq. Cryst.*, 37(6-7):669–678, 2010.

[46] F. Vita. Search for nematic biaxiality in bent-core mesogens: an x-ray diffraction perspective. *Liq. Cryst.*, 43(13-15):2254–2276, 2016.

[47] O. Francescangeli and E. T. Samulski. Insights into the cybotactic nematic phase of bent-core molecules. *Soft Matter*, 6:2413–2420, 2010.

[48] O. Francescangeli, F. Vita, C. Ferrero, T. Dingemans, and E. T. Samulski. Cybotaxis dominates the nematic phase of bent-core mesogens: a small-angle diffuse x-ray diffraction study. *Soft Matter*, 7:895–901, 2011.

[49] O. Francescangeli, F. Vita, and E. T. Samulski. The cybotactic nematic phase of bent-core mesogens: state of the art and future developments. *Soft Matter*, 10:7685–7691, 2014.

[50] F. Vita, T. Tauscher, F. Speetjens, E. T. Samulski, and O. Scharrer, E.and Francescangeli. Evidence of biaxial order in the cybotactic nematic phase of bent-core mesogens. *Chem. Mater.*, 26:4671–4674, 2014.

[51] F. Vita, T. Tauscher, F. Speetjens, C. Ferrero, E. T. Samulski, E. Scharrer, and O. Francescangeli. Insights into biaxial ordering of bent-core nematics: X-ray diffraction evidence. *Mol. Cryst. Liq. Cryst.*, 611(1):171–179, 2015.

[52] A. Jákli. Liquid crystals of the twenty-first century – nematic phase of bent-core molecules. *Liq. Cryst. Rev.*, 1(1):65–82, 2013.

[53] S. Droulias, A.G. Vanakaras, and D.J. Photinos. Extending the maier–saupe theory to cybotactic nematics. *Liq. Cryst.*, 37(6-7):969–976, 2010.

[54] F. Speetjens, J. Lindborg, T. Tauscher, N. LaFemina, J. Nguyen, E. T. Samulski, F. Vita, O. Francescangeli, and E. Scharrer. Low nematic onset temperatures and room temperature cybotactic behavior in 1,3,4-oxadiazole-based bent-core mesogens possessing lateral methyl groups. *J. Mater. Chem.*, 22:22558–22564, 2012.

[55] J. Nguyen, W. Wonderly, T. Tauscher, R. Harkins, F. Vita, G. Portale, O. Francescangeli, E. T. Samulski, and E. Scharrer. The effects of lateral halogen substituents on the low-temperature cybotactic nematic phase in oxadiazole based bent-core liquid crystals. *Liq. Cryst.*, 42(12):1754–1764, 2015.

[56] A. Glebowska, F. Vita, O. Francescangeli, T. Dingemans, and E. Samulski. Molecular engineering room-temperature bent-core nematics. *Liq. Cryst.*, 42(5-6):829–839, 2015.

[57] W. Weissflog, H. Nádasi, U. Dunemann, G. Pelzl, S. Diele, A. Eremin, and H. Kresse. Influence of lateral substituents on the mesophase behaviour of banana-shaped mesogens. *J. Mater. Chem.*, 11:2748–2758, 2001.

[58] U. Dunemann, M. W. Schröder, R. A. Reddy, G. Pelzl, S. Diele, and W. Weissflog. The influence of lateral substituents on the mesophase behaviour of banana-shaped mesogens. part ii. *J. Mater. Chem.*, 15:4051–4061, 2005.

[59] M. Mathews, S. Kang, S. Kumar, and Q. Li. Designing bent-core nematogens towards biaxial nematic liquid crystals. *Liq. Cryst.*, 38(1):31–40, 2011.

[60] L. L. Cooper, E. T. Samulski, and E. Scharrer. Towards room temperature biaxial nematics. *Mol. Cryst. Liq. Cryst.*, 511(1):203/[1673]–217/[1687], 2009.

[61] R. Harkins, T. Tauscher, J. Nguyen, S. Lewis, F. C. Adamo, M. Pisani, D. Hermida-Merino, E. T. Samulski, F. Vita, O. Francescangeli, and E. Scharrer. Biaxial ordering in the supercooled nematic phase of bent-core mesogens: effects of molecular symmetry and outer wing lateral groups. *Liq. Cryst.*, 0(0):1–13, 2019.

[62] Y.-K. Kim, G. Cukrov, F. Vita, E. Scharrer, E. T. Samulski, O. Francescangeli, and O. D. Lavrentovich. Search for microscopic and macroscopic biaxiality in the cybotactic nematic phase of new oxadiazole bent-core mesogens. *Phys. Rev. E*, 93:062701, 2016.

[63] W. Wedler, P. Hartmann, U. Bakowsky, S. Diele, and D. Demus. X-ray investigations in low-molecular-weight glassy mesophases. *J. Mater. Chem.*, 2:1195–1204, 1992.

[64] T. Hegmann, J. Kain, S. Diele, G. Pelzl, and C. Tschierske. Evidence for the existence of the mcmillan phase in a binary system of a metallomesogen and 2,4,7-trinitrofluorenone. *Angew. Chem. Int. Edit.*, 40(5):887–890, 2001.

[65] M. Lehmann, C. Köhn, J. L. Figueirinhas, G. Feio, C. Cruz, and R. Y. Dong. Biaxial nematic mesophases from shape-persistent mesogens with a fluorenone bending unit. *Chem.-Eur. J.*, 16(28):8275–8279, 2010.

[66] M. Lehmann, S.-W. Kang, C. Köhn, S. Haseloh, U. Kolb, D. Schollmeyer, Q. Wang, and S. Kumar. Shape-persistent v-shaped mesogens—formation of nematic phases with biaxial order. *J. Mater. Chem.*, 16:4326–4334, 2006.

[67] A. J. Leadbetter, R. M. Richardson, and C. N. Colling. The structure of a number of nematogens. *J. Phys. Colloques*, 36(C1-37-C1-43), 1975.

[68] O. Francescangeli, S.I. Torgova, L.A. Karamysheva, T.A. Geivandova, A. Strigazzi, V. Stanic, C. Ferrero, and I. Dolbnya. 19th international liquid crystal conference. *Book of Abstracts*, page 137, 2002.

[69] G. Shanker, M. Prehm, M. Nagaraj, J. K. Vij, M. Weyland, A. Eremin, and C. Tschierske. 1,2,4-oxadiazole-based bent-core liquid crystals with cybotactic nematic phases. *ChemPhysChem*, 15(7):1323–1335, 2014.

[70] S. Ghosh, N. Begum, S. Turlapati, S. K. Roy, A. K. Das, and N. V. S. Rao. Ferroelectric-like switching in the nematic phase of four-ring bent-core liquid crystals. *J. Mater. Chem. C*, 2:425–431, 2014.

[71] S. Turlapati, R. K. Khan, S. Ghosh, P. Tadapatri, R. Pratibha, and N. V. S. Rao. Existence of polar switching in the nematic and orthogonal smectic phases in novel four-ring bent-core compounds. *J. Appl. Phys.*, 120(17):174101, 2016.

[72] S. Havriliak and S. Negami. A complex plane representation of dielectric and mechanical relaxation processes in some polymers. *Polymer*, 8:161 – 210, 1967.

[73] H. G. Yoon, Sh.-W. Kang, M. Lehmann, J. O. Park, M. Srinivasarao, and S. Kumar. Homogeneous and homeotropic alignment of bent-core uniaxial and biaxial nematic liquid crystals. *Soft Matter*, 7:8770–8775, 2011.

[74] L. J. Yu and A. Saupe. Observation of a biaxial nematic phase in potassium laurate-1-decanol-water mixtures. *Phys. Rev. Lett.*, 45:1000–1003, 1980.

[75] E. Akpinar, D. Reis, and A. Figueiredo Neto. Effect of alkyl chain length of alcohols on nematic uniaxial-to-biaxial phase transitions in a potassium laurate/alcohol/k2so4/water lyotropic mixture. *Liq. Cryst.*, 39, 2012.

[76] E. Akpinar, D. Reis, and Antonio M. Figueiredo Neto. Anomalous behavior in the crossover between the negative and positive biaxial nematic mesophases in a lyotropic liquid crystal. *ChemPhysChem*, 15(7):1463–1469, 2014.

[77] J.-F. Li, V. Percec, C. Rosenblatt, and O. D. Lavrentovich. Biaxiality in a cyclic thermotropic nematic liquid crystal. *Europhys. Lett.*, 25(3):199–204, 1994.

[78] I. M. Syed, V. Percec, R. G. Petschek, and C. Rosenblatt. Apparent tricritical behavior at a nearly second-order nematic-isotropic phase transition of a cyclic liquid crystalline trimer. *Phys. Rev. E*, 67:011704, 2003.

[79] B. R. Acharya, A. Primak, T. J. Dingemans, E. T. Samulski, and S. Kumar. The elusive thermotropic biaxial nematic phase in rigid bent-core molecules. *Pramana*, 61(2):231–237, 2003.

[80] J.-H. Lee, T.-K. Lim, W.-T. Kim, and J.-I. Jin. Dynamics of electro-optical switching processes in surface stabilized biaxial nematic phase found in bent-core liquid crystal. *J. Appl. Phys.*, 101(3):034105, 2007.

[81] J. You, J. Jung, K. Rhie, V. Pergamenshchik, and S. Shin. Macroscopic properties of the nematic phase of boomerang-shaped c7: Evidence of biaxiality. *J. Korean Phys. Soc.*, 52, 2008.

[82] G. S. Lee, J. S. Cho, J. C. Kim, T.-H. Yoon, and S.-T. Shin. Direct confirmation of biaxiality in a bent-core mesogen through the measurement of electro-optic characteristics. *J. Appl. Phys.*, 105(9):094509, 2009.

[83] M. Nagaraj, K. Merkel, J. K. Vij, and A. Kocot. Macroscopic biaxiality and electric-field–induced rotation of the minor director in the nematic phase of a bent-core liquid crystal. *EPL*, 91(6):66002, 2010.

[84] M. S. Park, B.-J. Yoon, J. O. Park, V. Prasad, S. Kumar, and M. Srinivasarao. Raman scattering study of phase biaxiality in a thermotropic bent-core nematic liquid crystal. *Phys. Rev. Lett.*, 105:027801, 2010.

[85] V. Prasad, S.-W. Kang, K. A. Suresh, L. Joshi, Q. Wang, and S. Kumar. Thermotropic uniaxial and biaxial nematic and smectic phases in bent-core mesogens. *Journal of the American Chemical Society*, 127(49):17224–17227, 2005.

[86] R. Y. Dong, S. Kumar, V. Prasad, and J. Zhang. High nematic ordering in a bent-core smectogen showing a biaxial nematic phase: A 13c nmr study. *Chem. Phys. Lett.*, 448(1):54 – 60, 2007.

[87] H. G. Yoon, S.-W. Kang, R. Y. Dong, A. Marini, K. A. Suresh, M. Srinivasarao, and S. Kumar. Nematic biaxiality in a bent-core material. *Phys. Rev. E*, 81:051706, 2010.

[88] J. Seltmann, A. Marini, B. Mennucci, S. Dey, S. Kumar, and M. Lehmann. Non-symmetric bent-core liquid crystals based on a 1,3,4-thiadiazole core unit and their nematic mesomorphism. *Chem. Mater.*, 23(10):2630–2636, 2011.

[89] K. Merkel, A. Kocot, J. K. Vij, G. H. Mehl, and T. Meyer. The orientational order parameters of a dendritic liquid crystal organo-siloxane tetrapode oligomer, determined using polarized infrared spectroscopy. *J. Chem. Phys.*, 121(10):5012–5021, 2004.

[90] K. Merkel, A. Kocot, J. K. Vij, R. Korlacki, G. H. Mehl, and T. Meyer. Thermotropic biaxial nematic phase in liquid crystalline organo-siloxane tetrapodes. *Phys. Rev. Lett.*, 93:237801, 2004.

[91] K. Neupane, S. W. Kang, S. Sharma, D. Carney, T. Meyer, G. H. Mehl, D. W. Allender, Satyendra Kumar, and S. Sprunt. Dynamic light scattering study of biaxial ordering in a thermotropic liquid crystal. *Phys. Rev. Lett.*, 97:207802, 2006.

[92] A. Kocot and J. Vij. Study of the biaxiality in the nematic phase of liquid crystals in terms of orientational order parameters by infrared spectroscopy. *Liq. Cryst.*, 37:653–667, 2010.

[93] K. Merkel, M. Nagaraj, A. Kocot, A. Kohlmeier, G. H. Mehl, and J. K. Vij. Biaxial order and a rotation of the minor director in the nematic phase of an organo-siloxane tetrapode by the electric field. *J. Chem. Phys.*, 136(9):094513, 2012.

[94] D. Filip, C. Cruz, P. J. Sebastião, M. Cardoso, A. C. Ribeiro, M. Vilfan, T. Meyer, P. H. J. Kouwer, and G. H. Mehl. Phase structure and molecular dynamics of liquid-crystalline side-on organosiloxane tetrapodes. *Phys. Rev. E*, 81:011702, 2010.

[95] B. Senyuk, Y.-K. Kim, L. Tortora, S.-T. Shin, S. V. Shiyanovskii, and O. D. Lavrentovich. Surface alignment, anchoring transitions, optical properties and topological defects in nematic bent-core materials c7 and c12. *Mol. Cryst. Liq. Cryst.*, 540(1):20–41, 2011.

[96] B. Senyuk, H. Wonderly, M. Mathews, Q. Li, S. V. Shiyanovskii, and O. D. Lavrentovich. Surface alignment, anchoring transitions, optical properties, and topological defects in the nematic phase of thermotropic bent-core liquid crystal a131. *Phys. Rev. E*, 82:041711, 2010.

[97] V. Berejnov, V. Cabuil, R. Perzynski, and Yu. Raikher. Lyotropic system potassium laurate/1-decanol/water as a carrier medium for a ferronematic liquid crystal: Phase diagram study. *J. Phys. Chem. B*, 102(37):7132–7138, 1998.

[98] V. Berejnov, V. Cabuil, Régine Perzynski, Yuriy Raikher, S. Lysenko, and V. Sdobnov. Lyotropic nematogenic system potassium laurate-1-decanol-water: Method of synthesis and study of phase diagrams. *Crystallogr. Rep.*, 45:493–500, 2000.

[99] Y. Galerne. Comment on "thermotropic biaxial nematic liquid crystals". *Phys. Rev. Lett.*, 96:219803, 2006.

[100] T. Ostapenko, C. Zhang, S. N. Sprunt, A. Jákli, and J. T. Gleeson. Magneto-optical technique for detecting the biaxial nematic phase. *Phys. Rev. E*, 84:021705, 2011.

[101] Y.-K. Kim, M. Majumdar, B. I. Senyuk, L. Tortora, J. Seltmann, M. Lehmann, A. Jákli, J. T. Gleeson, O D. Lavrentovich, and S. Sprunt. Search for biaxiality in a shape-persistent bent-core nematic liquid crystal. *Soft Matter*, 8:8880–8890, 2012.

[102] Y.-K. Kim, B. Senyuk, S.-T. Shin, A. Kohlmeier, G. H. Mehl, and O. D. Lavrentovich. Surface alignment, anchoring transitions, optical properties, and topological defects in the thermotropic nematic phase of organo-siloxane tetrapodes. *Soft Matter*, 10:500–509, 2014.

[103] E. van den Pol, A. V. Petukhov, D. M. E. Thies-Weesie, D. V. Byelov, and G. J. Vroege. Experimental realization of biaxial liquid crystal phases in colloidal dispersions of boardlike particles. *Phys. Rev. Lett.*, 103:258301, 2009.

[104] C. Chiccoli, I. Feruli, O. D. Lavrentovich, P. Pasini, S. V. Shiyanovskii, and C. Zannoni. Topological defects in schlieren textures of biaxial and uniaxial nematics. *Phys. Rev. E*, 66:030701, 2002.

[105] M. Kleman and O. D. Lavrentovich. Topological point defects in nematic liquid crystals. *Philosophical Magazine*, 86(25-26):4117–4137, 2006.

[106] M. Kleman and O. D. Lavrentovich. *Soft Matter Physics: An Introduction*. Springer-Verlag, 2003.

[107] G. R. Luckhurst. A missing phase found at last? *Nature*, 430(6998):413–414, 2004.

[108] F. J. Kahn. Orientation of liquid crystals by surface coupling agents. *Appl. Phys. Lett.*, 22(8):386–388, 1973.

[109] Y. Kinoshita, B. Park, H. Takezoe, T. Niori, and J. Watanabe. Visualization of the molecular shape and the orientational distribution in the langmuir-blodgett film of a bent-shaped achiral molecule as studied by surface second-harmonic generation. *Langmuir*, 14(21):6256–6260, 1998.

[110] L. Zou, J. Wang, V. J. Beleva, E. E. Kooijman, S. V. Primak, J. Risse, W. Weissflog, A. Jákli, and E. K. Mann. Langmuir monolayers of bent-core molecules. *Langmuir*, 20(7):2772–2780, 2004.

[111] J. Wang, L. Zou, A. Jákli, W. Weissflog, and E. K. Mann. Anisotropy in langmuir layers of a bent-core liquid crystal. *Langmuir*, 22(7):3198–3206, 2006.

[112] L. M. Blinov, S. P. Palto, V. V. Lazarev, A. R. Geivandov, and S. G. Yudin. Antiferro-electric and ferroelectric switching of a liquid crystal in langmuir-blodgett films under strong confinement conditions. *Crystallogr. Rep.*, 51(5):843–849, 2006.

[113] A. R. Geivandov, S. P. Palto, S. G. Yudin, L. M. Blinov, G. Pelzl, and W. Weissflog. Ferro- and antiferroelectric properties of langmuir-blodgett films composed of mesogenic bent-core molecules. *Ferroelectrics*, 344(1):3–10, 2006.

[114] I. Giner, I. Gascón, J. Vergara, M. C. López, M. B. Ros, and F. M. Royo. Molecular arrangement in langmuir and langmuir-blodgett films of a mesogenic bent-core carboxylic acid. *Langmuir*, 25(20):12332–12339, 2009.

[115] P. García-Vázquez, O.G. Morales-Saavedra, G. Pelzl, J. Guadalupe Bañuelos, and M.P. Carreón-Castro. Incorporation in langmuir and langmuir-blodgett films of symmetric fluorine substituted bent-core liquid crystals: Morphological and optical properties. *Thin Solid Films*, 517(5):1770 – 1777, 2009.

[116] J. Wang, L. Qiu, A. Jákli, W. Weissflog, and E. K. Mann. Inverse langmuir–schaefer films of bent-core molecules. *Liq. Cryst.*, 37(10):1229–1236, 2010.

[117] T. Smith, W. Iglesias, S. Stefanovic, E. Mann, C. Tschierske, A. Jákli, and D. Lacks. Effects of tether length on the behavior of amphiphilic bent-core molecules at water surfaces. *J. Phys. Chem. B*, 115:12809–15, 2011.

[118] W. Iglesias, T. J. Smith, P. B. Basnet, S. Stefanovic, C. Tschierske, D. J. Lacks, A. Jákli, and E. K. Mann. Alignment by langmuir/schaefer monolayers of bent-core liquid crystals. *Ferroelectrics*, 431(1):141–149, 2012.

[119] R. Kaur, G. K. Bhullar, N. V. S. Rao, and K.K. Raina. Effect of ph on the control of molecular orientation in monolayer of bent-core liquid crystal materials by langmuir–blodgett method. *Liq. Cryst.*, 42(1):8–17, 2015.

[120] G. Roberts. *Langmuir-Blodgett films*. Plenum Press, 1990.

[121] N. Duff, J. Wang, E. K. Mann, and D. J. Lacks. Molecular dynamics investigation of bent-core molecules on a water surface. *Langmuir*, 22(22):9082–9085, 2006.

[122] M. N. G. de Mul and J. A. Mann. Determination of the thickness and optical properties of a langmuir film from the domain morphology by brewster angle microscopy. *Langmuir*, 14(9):2455–2466, 1998.

[123] F. C. Goodrich. Molecular interaction in mixed monolayers. In *Proceedings of the 2nd International Congress of Surface Activity. London: Butterworth*, 1957.

[124] R. G. Oliveira, R. O. Calderón, and B. Maggio. Surface behavior of myelin monolayers. *Biochimica et Biophysica Acta (BBA) - Biomembranes*, 1370(1):127 – 137, 1998.

[125] M. Björck and G. Andersson. Genx: An extensible x-ray reflectivity refinement program utilizing differential evolution. *J. Appl. Cryst.*, 40:1174–1178, 2007.

[126] L. G. Parratt. Surface studies of solids by total reflection of x-rays. *Phys. Rev.*, 95:359–369, 1954.

[127] P. Croce and L. Névot. Étude des couches minces et des surfaces par réflexion rasante spéculaire ou diffuse, de rayons x. *Revue de Physique appliquée*, 11:113–125, 1976.

[128] L. Névot and P. Croce. Caractérisation des surfaces par réflexion rasante de rayons x. application à l'étude du polissage de quelques verres silicates. 15:761–779, 1980.

[129] M. Morita, T. Ohmi, E. Hasegawa, M. Kawakami, and M. Ohwada. Growth of native oxide on a silicon surface. *J. Appl. Phys.*, 68(3):1272–1281, 1990.

[130] R. J. Cotter. *Engineering Plastics*. Gordon and Breach Publishers, 1995.

[131] Ed. K. L. Mittal. *Polyimides and Other High Temperature Polymers: Synthesis, Characterization and Applications.* Koninklijke Brill NV, 2009.

[132] J. K. Fink. *High Performance Polymers.* William Andrew Inc., 2008.

[133] P. M. Hergenrother, J. W. Connell, J. W. Labadie, and J. L. Hedrick. Poly(arylene ether)s containing heterocyclic units. *Adv. Polym. Sci.*, 117:67–110, 1994.

[134] P. M. Hergenrother. The use, design, synthesis, and properties of high performance/high temperature polymers: An overview. *High Perform. Polym*, 15:3–45, 2003.

[135] M. A. Meador. Recent advances in the development of processable high-temperature polymers. *Annu. Rev. Mater. Sci.*, 28(1):599–630, 1998.

[136] A. M. Donald, A. H. Windle, and S. Hanna. *Liquid Crystalline Polymers.* Cambridge University Press, 2 edition, 2006.

[137] T. Dingemans. High-temperature thermosets. In K. Matyjaszewski and M. Möller, editors, *Polymer Science: A Comprehensive Reference*, pages 753 – 769. Elsevier, Amsterdam, 2012.

[138] P. G. De Gennes. Possibilites offertes par la reticulation de polymeres en presence d'un cristal liquide. *Physics Letters A*, 28(11):725 – 726, 1969.

[139] M. Warner, K. P. Gelling, and T. A. Vilgis. Theory of nematic networks. *The Journal of Chemical Physics*, 88(6):4008–4013, 1988.

[140] G. G. Barclay, C. K. Ober, K. I. Papathomas, and D. W. Wang. Rigid-rod thermosets based on 1,3,5-triazine-linked aromatic ester segments. *Macromolecules*, 25(11):2947–2954, 1992.

[141] A. J. Gavrin, C. L. Curts, and E. P. Douglas. High-temperature stability of a novel phenylethynyl liquid-crystalline thermoset. *J. Polym. Sci., Part A: Polym. Chem*, 37(22):4184–4190, 1999.

[142] A. J. Gavrin and E. P. Douglas. Isothermal curing of acetylene functionalized liquid crystalline thermoset monomers. *Macromolecules*, 34(17):5876–5884, 2001.

[143] A. Knijnenberg, E. S. Weiser, T. L. StClair, E. Mendes, and T. J. Dingemans. Synthesis and characterization of aryl ethynyl terminated liquid crystalline oligomers and their cured polymers. *Macromolecules*, 39(20):6936–6943, 2006.

[144] F. Vita, F. C. Adamo, M. Pisani, L. M. Heist, M. Li, M. Hegde, T. J. Dingemans, E. T. Samulski, and O. Francescangeli. Liquid crystal thermosets. a new class of high-performance materials. *Liq. Cryst.*, 0(0):1–11, 2019.

[145] J. W. Connell, J. G. Smith JR., and P. M. Hergenrother. Oligomers and polymers containing phenylethynyl groups. *J. Macromol. Sci., Rev. Macromol. Chem. Phys. C*, 40(2-3):207–230, 2000.

[146] P.M Hergenrother, J.W Connell, and J.G Smith. Phenylethynyl containing imide oligomers. *Polymer*, 41(13):5073 – 5081, 2000.

[147] C. C. Roberts, T. M. Apple, and G. E. Wnek. Curing chemistry of phenylethynyl-terminated imide oligomers: Synthesis of 13c-labeled oligomers and solid-state nmr studies. *J. Polym. Sci., Part A: Polym. Chem.*, 38(19):3486–3497, 2000.

[148] P. B. J. Thompson, L. Bouchenoire, S. D. Brown, D. Mannix, D. F. Paul, C. Lucas, J. Kervin, M. J. Cooper, P. Arakawa, and G. Laughon. New developments at the xmas beamline for magnetic and high resolution diffraction. *AIP Conf. Proc.*, 705(1):428–431, 2004.

[149] T. J. Bunning, H. Korner, V. V. Tsukruk, C. M. McHugh, C. K. Ober, and W. W. Adams. Structural characterization of biphenyl ester-based lc molecules: Peculiarities of cyclic siloxane-based materials. *Macromolecules*, 29(27):8717–8725, 1996.

[150] F. Vita, M. Hegde, G. Portale, W. Bras, C. Ferrero, E. T. Samulski, O. Francescangeli, and T. Dingemans. Molecular ordering in the high-temperature nematic phase of an all-aromatic liquid crystal. *Soft Matter*, 12:2309–2314, 2016.

[151] C. Gong, Q. Luo, Y. Li, M. Giotto, N. E. Cipollini, Z. Yang, R. A. Weiss, and D. A. Scola. Free radical initiated low temperature crosslinking of phenylethynyl (pe) end-capped oligomides. *J. Poly. Sci. Part A: Poly. Chem.*, 48(18):3950–3963, 2010.

[152] A. Pines, M.G. Gibby, and J.S. Waugh. Proton-enhanced nuclear induction spectroscopy 13c chemical shielding anisotropy in some organic solids. *Chemical Physics Letters*, 15(3):373 – 376, 1972.

[153] M. Iqbal and T. J. Dingemans. High tg nematic thermosets: Synthesis, characterization and thermo-mechanical properties. *Euro. Poly. J.*, 46(11):2174 – 2180, 2010.

[154] P. Davidson, D. Petermann, and A. M. Levelut. The measurement of the nematic order parameter by x-ray scattering reconsidered. *J. Phys. II*, 5:113–131, 1995.

[155] M Deutsch. Orientational order determination in liquid crystals by x-ray diffraction. *Phys. Rev. A*, 44:8264–8270, Dec 1991.

[156] A. Angelova, V. M. Garamus, B. Angelov, Z. Tian, Y. Li, and A. Zou. Advances in structural design of lipid-based nanoparticle carriers for delivery of macromolecular drugs, phytochemicals and anti-tumor agents. *Adv. Colloid Interface Sci.*, 249:331 – 345, 2017.

[157] P. Astolfi, E. Giorgini, V. Gambini, B. Rossi, L. Vaccari, F. Vita, O. Francescangeli, C. Marchini, and M. Pisani. Lyotropic liquid-crystalline nanosystems as drug delivery agents for 5-fluorouracil: Structure and cytotoxicity. *Langmuir*, 33(43):12369–12378, 2017.

[158] P. Astolfi, E. Giorgini, F. C. Adamo, F. Vita, S. Logrippo, O. Francescangeli, and M. Pisani. Effects of a cationic surfactant incorporation in phytantriol bulk cubic phases and dispersions loaded with the anticancer drug 5-fluorouracil. *J. Mol. Liq.*, 286:110954, 2019.

[159] A. Angelova, B. Angelov, R. Mutafchieva, S. Lesieur, and P. Couvreur. Self-assembled multicompartment liquid crystalline lipid carriers for protein, peptide, and nucleic acid drug delivery. *Acc. Chem. Res.*, 44(2):147–156, 2011.

[160] V. Cherezov, J. Clogston, Y. Misquitta, W. Abdel-Gawad, and M. Caffrey. Membrane protein crystallization in meso: Lipid type-tailoring of the cubic phase. *Biophys. J.*, 83(6):3393 – 3407, 2002.

[161] A. I. I. Tyler, H. M. G. Barriga, E. S. Parsons, N. L. C. McCarthy, O Ces, R. V. Law, J. M. Seddon, and N. J. Brooks. Electrostatic swelling of bicontinuous cubic lipid phases. *Soft Matter*, 11:3279–3286, 2015.

[162] H. Kim, Z. Song, and C. Leal. Super-swelled lyotropic single crystals. *Proc. Natl. Acad. Sci.*, 114(41):10834–10839, 2017.

[163] A. Zabara, J. T. Y. Chong, I. Martiel, L. Stark, B. A. Cromer, C. Speziale, C. John Drummond, and R. Mezzenga. Design of ultra-swollen lipidic mesophases for the crystallization of membrane proteins with large extracellular domains. *Nat. Commun.*, 9:544, 2018.

[164] I. R. Ribeiro, M. F. Immich, D. Lundberg, F. Poletto, and W. Loh. Physiological neutral ph drives a gradual lamellar-to-reverse cubic-to-reverse hexagonal phase transition in phytantriol-based nanoparticles. *Colloids Surf. B: Biointerfaces*, 177:204 – 210, 2019.

[165] B. Angelov, A. Angelova, M. Drechsler, V. M. Garamus, R. Mutafchieva, and S. Lesieur. Identification of large channels in cationic pegylated cubosome nanoparticles by synchrotron radiation saxs and cryo-tem imaging. *Soft Matter*, 11:3686–3692, 2015.

[166] Q. Liu, Y.-Da Dong, T. L. Hanley, and B. J. Boyd. Sensitivity of nanostructure in charged cubosomes to phase changes triggered by ionic species in solution. *Langmuir*, 29(46):14265–14273, 2013.

[167] H.-H. Shen, J. G. Crowston, F. Huber, S. Saubern, K. M. McLean, and P. G. Hartley. The influence of dipalmitoyl phosphatidylserine on phase behaviour of and cellular response to lyotropic liquid crystalline dispersions. *Biomaterials*, 31(36):9473 – 9481, 2010.

[168] J. D. Du, Q. Liu, S. Salentinig, T.-H. Nguyen, and B. J. Boyd. A novel approach to enhance the mucoadhesion of lipid drug nanocarriers for improved drug delivery to the buccal mucosa. *Int. J. Pharm.*, 471(1):358 – 365, 2014.

[169] A. Tan, L. Hong, J. D. Du, and B. J. Boyd. Self-assembled nanostructured lipid systems: Is there a link between structure and cytotoxicity? *Adv. Sci.*, 6(3):1801223, 2019.

[170] S. Deshpande and N. Singh. Influence of cubosome surface architecture on its cellular uptake mechanism. *Langmuir*, 33(14):3509–3516, 2017.

[171] Y.-D. Dong, I. Larson, T. Hanley, and B. J. Boyd. Bulk and dispersed aqueous phase behavior of phytantriol: Effect of vitamin e acetate and f127 polymer on liquid crystal nanostructure. *Langmuir*, 22(23):9512–9518, 2006.

[172] Y.-D. Dong, A. W. Dong, I. Larson, M. Rappolt, H. Amenitsch, T. Hanley, and B. J. Boyd. Impurities in commercial phytantriol significantly alter its lyotropic liquid-crystalline phase behavior. *Langmuir*, 24(13):6998–7003, 2008.

[173] C. Guo, J. Wang, F. Cao, R. J. Lee, and G. Zhai. Lyotropic liquid crystal systems in drug delivery. *Drug Discovery Today*, 15(23):1032 – 1040, 2010.

[174] A. Salonen, S. Guillot, and O. Glatter. Determination of water content in internally self-assembled monoglyceride-based dispersions from the bulk phase. *Langmuir*, 23(18):9151–9154, 2007.

[175] N. K. Swarnakar, K. Thanki, and S. Jain. Bicontinuous cubic liquid crystalline nanoparticles for oral delivery of doxorubicin: Implications on bioavailability, therapeutic efficacy, and cardiotoxicity. *Pharm. Res.*, 31(5):1219–1238, May 2014.

[176] E. Nazaruk, A. Majkowska-Pilip, and R. Bilewicz. Lipidic cubic-phase nanoparticles—cubosomes for efficient drug delivery to cancer cells. *ChemPlusChem*, 82(4):570–575, 2017.

[177] S. Jain, N. Bhankur, N. K. Swarnakar, and K. Thanki. Phytantriol based "stealth" lyotropic liquid crystalline nanoparticles for improved antitumor efficacy and reduced toxicity of docetaxel. *Pharm. Res.*, 32(10):3282–3292, Oct 2015.

[178] H. M. G. Barriga, M. N. Holme, and M. M. Stevens. Cubosomes: The next generation of smart lipid nanoparticles? *Angew. Chem. Int. Ed.*, 58(10):2958–2978, 2019.

[179] A. Chemelli, B. Conde-Valentín, F. Uhlig, and O. Glatter. Amino acid induced modification of self-assembled monoglyceride-based nanostructures. *Langmuir*, 31(38):10377–10381, 2015.

[180] T.-Y. D. Tang, N. J. Brooks, C. Jeworrek, O. Ces, N. J. Terrill, R. Winter, R. H. Templer, and J. M. Seddon. Hydrostatic pressure effects on the lamellar to gyroid cubic phase transition of monolinolein at limited hydration. *Langmuir*, 28(36):13018–13024, 2012.

[181] C. Czeslik, R. Winter, G. Rapp, and K. Bartels. Temperature- and pressure-dependent phase behavior of monoacylglycerides monoolein and monoelaidin. *Biophys. J.*, 68(4):1423 – 1429, 1995.

[182] B. Tenchov, R. Koynova, and G. Rapp. Accelerated formation of cubic phases in phosphatidylethanolamine dispersions. *Biophys. J.*, 75(2):853 – 866, 1998.

[183] B. W. Muir, G. Zhen, P. Gunatillake, and P. G. Hartley. Salt induced lamellar to bicontinuous cubic phase transitions in cationic nanoparticles. *J. Phys. Chem. B*, 116(11):3551–3556, 2012.

[184] S. Mutalik, P. K. Shetty, A. Kumar, R. Kalra, and H. S. Parekh. Enhancement in deposition and permeation of 5-fluorouracil through human epidermis assisted by peptide dendrimers. *Drug Deliv.*, 21(1):44–54, 2014.

[185] B. J. Boyd. Characterisation of drug release from cubosomes using the pressure ultrafiltration method. *Int. J. Pharm.*, 260(2):239 – 247, 2003.